



## REPORT ON THE SWIM CAL/VAL AT THE END OF THE VERIFICATION PHASE



AND



<p><b>Written by:</b></p> <p>D. Hauser, C. Tourain, L. Hermozo,</p> <p>With contributions from Alraddawi D., Aouf L., Chapron B., Collard F., Dalila M., Dalphiné A., Dufour C., Gouillon F., Grouazel A., Guitton G., Husson R., Lachiver J-M, Lacrouts C., Mironov A., Nougier F, Ollivier A., Perret B., Piras F., Rodriguez-Suquet R., Schippers P., Tison C.</p>	<p>On : 11 September 2019</p>	
<p><b>Validated by:</b></p>	<p>on:</p>	
<p><b>Distribution</b></p>		

## TABLE OF CONTENTS

REFERENCE DOCUMENTS.....	4
LIST OF FIGURES .....	6
ACRONYMS AND ABBREVIATIONS .....	11
1 - INTRODUCTION .....	13
2 - SWIM FUNCTIONAL VALIDATION .....	15
3 - SWIM INSTRUMENTAL PERFORMANCES.....	19
4 - DATA DELIVERY TO THE CNES MISSION CENTRE.....	23
5 - NADIR PRODUCTS (L2A).....	25
5.1 VARIABLES ANALYZED .....	25
5.2 VALIDATION METHOD AND DATA SETS USED FOR ANALYSIS .....	26
5.3 MAIN RESULTS .....	26
5.3.1 Retracking algorithm performance.....	26
5.3.2 Significant Wave Height .....	27
5.3.3 Sigma0.....	29
5.3.4 Improvement with respect to the conventional altimetry processing.....	30
5.3.5 Wind Speed .....	32
5.3.6 Nadir rain flag.....	33
5.3.7 Mean Square Slope parameter.....	34
5.4 FORESEEN ANALYSES AND EVOLUTIONS .....	35
6 - SIGMA0 PRODUCTS (L1A_CWWIC, L2_CWWIC).....	37
6.1 VARIABLES ANALYZED AND STEPS FOR THE VERIFICATION .....	37
6.2 VALIDATION METHOD AND DATA SET USED FOR ANALYSIS .....	38
6.3 MAIN RESULTS .....	38
6.3.1 Antenna gain compensation .....	38
6.3.2 Thermal noise corrections and signal to noise ratio .....	43
6.3.3 Sigma0 analysis .....	43
6.4 FORESEEN ANALYSES AND EVOLUTIONS .....	51
6.4.1 Planned processing evolutions .....	51
6.4.2 Foreseen analyses .....	51
7 - L1B PRODUCTS (L1B CWWIC AND IWWOC ANALYSIS) .....	52
7.1 VARIABLES ANALYZED .....	52
7.2 VALIDATION METHOD AND DATA SET USED FOR ANALYSIS .....	52
7.3 MAIN RESULTS .....	52
7.3.1 Along-track perturbation due to speckle noise.....	53
7.3.2 Fluctuation spectra compared to wave spectra.....	55
7.3.3 Fluctuation statistics .....	57
7.3.4 First analysis of the speckle density spectrum .....	59
7.4 FORESEEN ANALYSES AND EVOLUTIONS .....	63
7.4.1 Planned processing evolutions .....	63
7.4.2 Foreseen analyses .....	64
8 - L2 PRODUCTS (L2 CWWIC).....	65
8.1 VARIABLES ANALYZED .....	65
8.2 VALIDATION METHOD AND DATA SET USED FOR ANALYSIS .....	65
8.1 COMPARISONS OF THE DIRECTIONAL SPECTRA FROM DIFFREENT BEAMS AND WITH MFWAM SPECTRA .....	66
8.2 STATISTICS AND MAPS OF WAVE PARAMETERS .....	68
8.2.1 Significant wave height of the wave spectra .....	68
8.2.2 Wave parameters from the SWIM products partitions.....	70
8.2.3 Analysis using partitions estimated a posteriori from the MFWAM model .....	73
8.3 ADDITIONAL CONSIDERATIONS ON THE WAVE SPECTRUM PARTITIONING.....	75

8.4	SOME COMPARISONS WITH BUOY DATA .....	77
8.5	STUDIES ON THE MODULATION TRANSFER FUNCTION .....	79
8.5.1	MTF from the CWWIC products .....	79
8.5.1	indirect analysis of THE mtf through comparisons of Slope spectra between SWIM and WW3	81
8.6	VALIDATION BY USING ASSIMILATION PROCESSES IN WAVE FORECAST MODEL	82
8.6.1	Methodology.....	82
8.6.2	Results .....	83
8.7	FORESEEN ANALYSES AND EVOLUTIONS .....	84
8.7.1	Planned processing evolutions .....	84
8.7.2	Foreseen analyses .....	84
9 -	SYNTHESIS AND CONCLUSION .....	85
10 -	ANNEX A - SWIM ACQUISITION MODES SINCE THE 25 <sup>th</sup> April 2019 .....	87
11 -	ANNEX B- CWWIC PROCESSING VERSIONS CORRESPONDING TO DATA RELEASE TO USERS	88

## REFERENCE DOCUMENTS

Index	Reference	Document title
R1	CF-SYMI-PL-1726-CNES	CAL/VAL Plan
R2	CF-GSFR-MU-2530-CNES	Product User Guide (PUG)
R3	Hauser D., C. Tison, T. Amiot, L. Delaye, N. Corcoral et al, SWIM: the first spaceborne wave scatterometer, <i>IEEE Trans. On Geoscience and Remote Sensing</i> , 10.1109/TGRS.2017.2658672 , VOL 55, 5, May 2017	
R4	Brown, G . S., The average impulse response of a rough surface and its applications, <i>IEEE Trans. Antenna Propagat.</i> , 2, 5(1), 67-74, 1977.	
R5	Poisson et al., 2018 : « Development of an ENVISAT Altimetry Processor Providing Sea Level Continuity Between Open Ocean and Arctic Leads, <i>IEEE Transactions on Geoscience and Remote Sensing</i> PP(99):1-21, DOI:10.1109/TGRS.2018.2813061	
R6	J. A. Nelder R. Mead , “A simplex method for function optimization” , <i>The Computer Journal</i> , Volume 7, Issue 4, January 1965, Pages 308–313, doi 10.1093.7.4.308	
R7	J. Tournadre, J. C. Poisson, N. Steunou & B. Picard, Validation of AltiKa Matching Pursuit Rain Flag, <i>Marine Geodesy</i> , 38-1, p 107-123, 2015, doi 10.1080/01490419.2014.1001048	
R8	Collard, F.: Algorithmes de vent et période moyenne des vagues JASON à base de réseaux de neurons. <i>BO-021-CLS-0407-RF, Boost Technologies</i> , 33 pp., 2005	
R9	Gourrion, J., D. Vandemark, S. Bailey, B. Chapron, G. P. Gommenginger, P. G. Challenor, and M. A. Srokosz: A two-parameter wind speed algorithm for Ku-band altimeters. <i>J. Atmos. Oceanic Technol.</i> , <b>19</b> , 2030–2048, 2002, doi:10.1175/1520-0426	
R10	Abdalla, S., Ku-band radar altimeter surface wind speed algorithm. <i>Mar. Geod.</i> , <b>35</b> (Suppl.), 2012, 276–298, doi:10.1080/01490419.2012.718676	
R11	John Lillibridge J., One- and Two-Dimensional Wind Speed Models for Ka-Band Altimetry, <i>J. Atmos. Oceanic Technol.</i> , 2014, doi:10.1175/JTECH-D-13-00167.1	
R12	Ulaby F. D. Long, W. Blackwell, C. Elachi, A.K. Fung, C. Rif K. Sarabandi, H. Zebker and J. Van Zyl, <i>Microwave Radar and Radiometric Remote Sensing</i> , Univ. of Michigan Press, ISBN: 978-0-472-11935-6, 2014	
R13	Hasselmann S., C. Brüning, K. Hasselmann, and P. Heimbach, An improved algorithm for the retrieval of ocean wave spectra from synthetic aperture radar image spectra, <i>J. Geophys. Res.</i> , Vol101, C7, pp16,615-16,629, 1996	

R14	Jackson, F. C. (1981). An analysis of short pulse and dual frequency radar techniques for measuring ocean wave spectra from satellites. <i>Radio science</i> , 16(06), 1385-1400.	
R15	Jackson F. C., W. T. Walton, and P. L. Baker, Aircraft and satellite measurement of ocean wave directional spectra using scanning-beam microwave radars, <i>J. Geophys. Res.</i> , Vol. 90, 987-1004, 1985	
R16	Jackson, F. C. (1987). The radar ocean-wave spectrometer. <i>Johns Hopkins APL Technical Digest</i> , 8, 116-127.	

## LIST OF FIGURES

- Figure 1-1 : Position of the CFOSAT nadir track ( in km, relative to the nominal position) as a function of time (from November 2018 to mid-July 2019). The track is maintained at  $\pm 20$  km with respect to its nominal position thanks to maneuvers of the satellite every 40 to 45 days.
- Figure 2-1 : Localization of EDAC errors (red points). In blue: the Atlantic anomaly region
- Figure 2-2 : Echo power of beam  $4^\circ$  for 5 successive macrocycles on April 17<sup>th</sup> 2019. In this selected example, the perturbation of signal transmission induces by a micro-cut induces a loss of power, illustrated on the blue echo (due to lost pulses for the macrocycle configuration). However, the occurrence of this perturbation is scarce (see Fig 2.3)
- Figure 2-3 : Statistics of inconsistencies between switch matrix status (status of the actual beam performing the measurements) and command (instruction of the beam performing the measurements)
- Figure 2-4 : Rate of  $\sigma_0$  profiles impacted by the signal anomaly in the signal transmission between rotating plate and fixed part of the instrument (decrease of  $\sigma_0$  energy over the whole swath)
- Figure 3-1 Theoretical (red curve) and measured (blue curve) Point Target Response (PTR) function during an internal calibration sequence, and its derived parameters.
- Figure 3-2 : (a-top) Example of a typical nadir wave form over the ocean (raw data). (b-bottom) 1-day averaged wave forms of the nadir signal shown per class of significant wave height (from 1 to 6 m)
- Figure 3-3 : SWIM nadir tracking coverage (percentage of successful tracking with the on-board algorithm) over one cycle.
- Figure 3-4 : Typical echo (amplitude in dB as a function of range gate number) over the ocean from the nadir beam (blue) and  $2^\circ$  beam (orange). The noise floor is determined from the first range gates. Starting with version 4.3.1. of the processing the  $2^\circ$  beam is used instead of  $0^\circ$ .
- Figure 5-1 : Map of additional retracked data (red points) obtained with the adaptive retracking with respect to the conventional altimetry retracking (MLE4) over a 13 day cycle.
- Figure 5-2 : top: SWIM nadir SWH (NSEC data) compared to ECMWF SWH for a 13 day period. Top left: time-series of the differences (SWIM\_nadir-ECMWF). Top Right: scatter plot (SWIM nadir versus ECMWF). The mean bias is 12 cm. Bottom: mean difference between nadir and ECMWF SWH as a function of nadir SWH (left) or wind speed (right).
- Figure 5-3: SWIM Nadir SWH (product at the scale of each wave box) compared to the MFWAM model SWH. The considered data set covers the period from 20th December 2018 to 17th March 2019 and includes 266 809 samples. Samples corresponding to  $\sigma^0$  values less than 5 dB or greater than 25 dB have been filtered out, as well as SWIM SWH which have a standard deviation larger than 0.6 m.
- Figure 5-4: Top: Map of differences in  $H_s$  between CFOSAT and Jason 3 (a) and AltiKa (b) at cross over points. Corresponding scatter plots : Jason 3 versus SWIM (c), AltiKa versus SWIM (d).
- Figure 5-5: Map of  $\sigma_0$  differences points between CFOSAT and Jason 3 (a) and AltiKa (b) at crossover points. Corresponding scatter plots (c) Jason 3 versus SWIM, (d) AltiKa versus SWIM
- Figure 5-6: left: Swim nadir  $\sigma_0$  values over the Arctic from 2019/04/27 to 2019/05/27, right: ECMWF sea-ice cover over the Arctic from 2019/04/27 to 2019/05/27
- Figure 5-7 : Mean standard deviation of significant wave height as a function of the mean significant wave height for the “adaptive” algorithm applied to SWIM data (black line), MLE4 algorithm applied to SWIM data (red line) and MLE4 algorithm applied to JASON3 data. The SWIM data used for this analysis are 1 Hz-products, the period of analysis is from 24/12/2018 to 5/01/2019 (cycle 5) and data over sea-ice and coastal regions have been filtered out.
- Figure 5-8 : Left-hand side: Density spectrum of the SWIM nadir SWH along-track variability from the adaptive (blue curve) and MLE4 (red curve) retracking algorithms. The noise level is estimated at 20.2 cm for the adaptive method and 36.4 cm for the MLE4. The data set used for this analysis corresponds to the orbital cycle#5. Right-hand side: Same analysis but for one orbital cycle of Jason3.
- Figure 5-9 : Density spectrum of the SWIM nadir Sigma0 along-track variability from the adaptive (blue curve) and MLE4 (red curve) retracking algorithms. The data set used for this analysis corresponds to the orbital cycle#5

- Figure 5-10 : SWIM nadir  $\sigma_0$  values from the adaptive (blue curve) and MLE4 (red curve) retracking algorithms in the case of a rain event. Adaptive values follow the AGC variations (black curve), as physically expected in opposite to MLE4 values behavior.
- Figure 5-11 SWIM nadir wind speed compared to ECWFMF wind speed.
- Figure 5-12 SWIM nadir wind speed compared to ECMWF wind speed: Top: current SWIM product data; Bottom: results using the preliminary Look Up Table.
- Figure 5-13 Wind speed variance comparison: relative difference between SWIM wind speed variance and ECMWF wind speed variance. Left: Current SWIM wind speed retrieval algorithm; Right: results for SWIM wind speed obtained with a preliminary version of the Look Up Table. This analysis was obtained by accumulating 6 months of data (November 2018 to April 2019)
- Figure 5-14 : Rain event identification for CFOSAT cycle 5- Left: Radiometer rainfall rate for collocated point with a time lag less than 15min ; Right: rain event identified by SWIM nadir rain flag (value = 2)
- Figure 5-15 : Bloom event identification for CFOSAT cycle 5, identified by SWIM nadir rain flag (value =1)
- Figure 5-16 SWIM Mean Square Slope cartography for CFOSAT cycle 16; Left : over ocean; Right over Artic sea-ice.
- Figure 6-1 : Roll (blue curve) and pitch (orange curve) mispointing angles estimated from the L1A-processing algorithm, for more than 4000 consecutive measurements (about 880s) over ocean. Large-scale oscillations in the pitch mispointing angles highlight the reference ellipsoid impact on total pointing variations. Shorter scale oscillations are due to antenna rotation (see Fig below).
- Figure 6-2 : Roll (blue curve) and pitch (orange curve) mispointing angles estimated from the L1A-processing algorithm, for 1000 consecutive measurements over ocean(about 220s), on 2019/04/26. Thick lines represent mean oceanic roll (blue) and pitch (orange) mispointing angles averaged over 13 days of data. Oscillations in the pitch mispointing angles highlight the antenna rotation impact on mispointing variations.
- Figure 6-3 :  $\sigma_0$  profiles as a function of the elevation (in rad) for the different beams (beams  $0^\circ$  to  $10^\circ$  in different colors) and for 8 successive azimuths directions (with a shift in vertical axis to ease the presentation)
- Figure 6-4: Flag of convexity or concavity of the shape of  $\sigma_0$  with respect to the angle of incidence. Here zoom-in on an orbit for the  $8^\circ$  beam. The blue color indicates the samples for which the flag is raised (convexity stronger than that expected from the GPM data). This diagnosis is systematic on all the orbits for all the beams analyzed with this flag ( $6^\circ$ ,  $8^\circ$  and  $10^\circ$ ). Left plot: with the present antenna lobe pattern correction. Right-hand side plot: with an alternative antenna lobe pattern correction which combines laboratory measurements and simulation of the antenna pattern.
- Figure 6-5: Polar plots representing mean values for  $\sigma_0$  as a function of range in meters) in each azimuth direction (with respect to satellite track). 43 days of data have been averaged (before April 25<sup>th</sup> 2019). The color code represents the  $\sigma_0$  value (in dB). From top left to bottom right: for SWIM beams  $2^\circ$ ,  $4^\circ$ ,  $6^\circ$ ,  $8^\circ$ , and  $10^\circ$
- Figure 6-6 : Mean and standard deviation of  $\sigma_0$  for beams  $6^\circ$ ,  $8^\circ$ , and  $10^\circ$  over the ocean (blue lines), compared to the noise equivalent ratio (red lines)
- Figure 6-7 :  $\sigma_0$  values from L1a product (version 4.3.0) over the ocean (cumulated over 24 hours on 25-26 April 2018 for beams  $2^\circ$ ,  $4^\circ$  (top),  $6^\circ$ ,  $8^\circ$  and  $10^\circ$  (bottom). The color codes denote the number of points, the red solid and dashed lines refer to GPM reference look-up table (mean and standard deviation of the GPM values for the same range of wind and waves). The black line is a fit on the data
- Figure 6-8 : Pdf of  $\sigma_0$  values over the ocean (without sea ice) from L1 SWIM products (top 2 rows) compared to GPM (bottom 2 rows) for a period of 2,5 months. In these distributions, SWIM  $\sigma_0$  are taken at an incidence close to the beam center  $\pm 0.5^\circ$  (center value indicated on the top of the plots), except for near nadir, taken for SWIM at  $0.6^\circ \pm 0.25^\circ$ .
- Figure 6-9 : Mean profiles over 15 days of  $\sigma_0$  versus incidence from SWIM for ocean scenes (a) and sea ice scenes (b), estimated from L2 products in version 4.3.0. (c, d) profiles from GPM (with symmetry around nadir and shown as histograms)
- Figure 6-10 : Distribution of  $\sigma_0$  values for incidence values around  $0^\circ$  (a),  $2^\circ$ (b),  $4^\circ$ (c),  $6^\circ$ (d),  $8^\circ$ (e) and  $10^\circ$ (f) at ( $\pm 0.5^\circ$ ) as a function of wind speed (taken from the ECMWF model).

Figure 6-11: Maps of mean  $\sigma_0$  and its standard deviation for each beam center (2 to 10° beams) from L1A products of CFOSAT orbital cycle #4. Data plotted over the ocean for  $\text{abs}(\text{latitude}) < 50^\circ$  and distance to the coast  $> 100$  km.

Figure 6-12 :Left: Indicator on  $\sigma_0$  variance (for beam 10°) compared to a rain map from IMERG (right).

Figure 7-1: Mean Variance of the  $\sigma_0$  fluctuations calculated over each footprint and plotted as a function of the look direction with respect to the satellite track, for descending tracks (left) and ascending tracks (right). This plot was obtained by accumulating data over descending tracks for 1,5 days of observations.

Figure 7-2: An example of fluctuation spectra plotted in the radial geometry of the SWIM scans for the 8° incidence beam. The small colored segments around the cycloid give in each observed direction, the fluctuation spectra as a function of the wave number (wave numbers increasing from the center of the cycloids). The background arrows indicate the wave parameters from the WW3 model for the first spectral partition (direction, wavelength indicated by the vector, significant wave height given by the color code). On this example waves propagating from northwest are well identified in the SWIM fluctuation spectra (with a 180° ambiguity). In addition, the along-track perturbation appears clearly. This case is taken from observations on the April 29<sup>th</sup> 2019 in the Gulf of Lion (North Mediterranean Sea)

Figure 7-3 : Mean fluctuation spectra for a period of 6 days after April 25<sup>th</sup> (left) compared to the mean wave slope spectrum obtained from collocated points of WW3 outputs (right).

Figure 7-4 : Mean fluctuation spectra around the satellite track direction ( $\pm 20^\circ$  around the satellite track in abscissa) for a wavenumber of  $2\pi/30$  (rad/m). Ascending (resp. descending) tracks are shown in dashed (resp. solid) lines. The different colors are for different latitudes.

Figure 7-5 : Mean directional spectra (polar plots) of  $\sigma_0$  fluctuations for SWIM incidence beams 4° (a), 6° (b), 8° (c), and 10° (d). The mean was calculated over 6-day data set (2019/04/25 → 2019/04/30). The horizontal and vertical axis are  $k_x$  and  $k_y$  wavenumbers (cpm) with  $k_y$  aligned along the satellite track direction. (e) mean wave slope spectrum from WW3 for collocated points during the same period of time

Figure 7-6 : Polar plots of the correlation coefficient between SWIM fluctuation spectra and WW3 collocated wave slope spectra for the data set from April 25<sup>th</sup> to April 30<sup>th</sup> 2019. Horizontal and vertical axes refer to the wave number of the waves in two orthogonal directions, with the vertical axis aligned with the satellite along-track direction. (a) and (b): for SWIM beams 2° and 4°, respectively. (c) to (e): for SWIM beams 6°, 8°, 10° (from left to right)

Figure 7-7 : Histograms of variance (a, d), skewness (b,e) and kurtosis (c,f) of the  $\sigma_0$  fluctuations estimated for each footprint for a period of 2.5 days (27-29 April 2019). a ,b ,c: ocean scenes. d, e, f: sea-ice covered regions. The selection of “free ocean scenes” or “sea-covered scenes” has been carried out by using the ECMWF se-ice coverage parameter collocated with the SWIM data.

Figure 7-8 : Mean variance (left) and skewness (right) of the signal fluctuations within each footprint as a function of significant wave height (given by the ECMWF model here). Data are averaged over 1,5 days for the 10° beam SWIM observations. The along-track sector affected by the large speckle noise has been excluded in the statistics calculation ( $\pm 15^\circ$ )

Figure 7-9 : Mean density spectra of  $\sigma_0$  fluctuations as a function of wave number  $k$  (rad/m) averaged over data samples taken in the direction of minimum of  $\sigma_0$  variances for beams 6° (blue), 8° (orange) and 10° (green) and for observations acquired on April 26<sup>th</sup> 2019, between 00h et 12h. The triangle model adjusted on the data (for  $0.05 < k < 0.4$  rad/m) is indicated as dashed lines.

Figure 7-10 : Mean fluctuation spectra averaged by azimuthal sector with respect to the local orbital frame (w.r.t. the along-track direction) and averaged fluctuation spectra in the direction of minimum of variance over sectors of 180° (noted psp2b\_mean in the figure). The time period considered in the average quantities is 12 hours starting on 26 April 2019 OO UTC. (a,b,c): for SWIM beams at 6°, 8°, and 10°

Figure 7-11 : Top: Analytical model for speckle noise correction in the case of the 10° beam of SWIM (black dashed lines). The model combines a triangle function adjusted on fluctuation spectra in the direction of minimum of variance, and a polynomial function of order 2 in the sector close to the along-track

- direction. The fluctuation spectra have been corrected from the wave contribution. The different colors refer to different azimuth angles. Bottom: difference between fluctuation spectra and the fitted model.
- Figure 7-12 : Comparison of wave spectra obtained by applying the speckle correction from: (a) and (c): the analytical correction as currently implemented in the CWICC processing chain; (b) and (d) an empirical model which varies with azimuth to account for along-track perturbations and takes into account a modified background spectrum noise. Here the horizontal and vertical axes refer to the wave number of the waves in the Est-West and North-South directions, respectively. The white, red and yellow contours indicate the partitions found in each case.
- Figure 8-1 : 2D Wave spectrum from the CWWIC product. Left with the mask applied, right without the mask. The partitions (contours in solid white, red lines, and dashed yellow line) are estimated on the masked spectra to avoid a detection of partition in the along-track perturbed sector.
- Figure 8-2: Map correlation index (a) and quadratic difference (b) between pairs of spectra from SWIM beam 10° and SWIM beam 6° (c) and (d) : corresponding distribution
- Figure 8-3: Map of correlation index (a) and quadratic difference (b) between pairs of spectra from SWIM beam 10° and MFWAM.
- Figure 8-4 : Scatter plots (2d histograms) of significant wave height from SWIM, for (a) 10°, (b) 8° , (c) 6° beam, as a function of the MFWAM significant wave height. The red line is the linear regression line, the dashed black line indicates the 1:1 slope relation. The analyzed data set is from 26<sup>th</sup> -April to 8<sup>th</sup> May 2019.
- Figure 8-5 : Total significant wave height of SWIM (beam 10°) with respect to HS from MWAM spectra estimated by removing on both types of spectra the azimuth sector affected by the increased level of noise in the SWIM data.
- Figure 8-6 : Maps of SWIM (left) et MFWAM (right) total significant wave height for a period of about 13 days starting on April 26<sup>th</sup> 2019 02 :00. SWIM data are from the 10° beam in the left plot.
- Figure 8-7 : Maps of SWIM (a-b-c) et MFWAM (d-e-f) parameters of first spectral partition for a period of about 13 days starting on April 26<sup>th</sup> 2019 02 :00. (a, d): Significant wave height of the first partition, (b, e): direction of the first partition, (c,f): wavelength of the first partition. For SWIM, the processing version is the prototype of version 4.3.0. The SWIM results are shown for the 10° incidence beam. For MFWAM, the parameters are taken from files provided by Meteo-France based on their own partitioning method.
- Figure 8-8 : Scatter plots (2D histograms) for (a) the wavelength (b) the wave direction, (c) the wave height of the first partition. In each case the first partition from the SWIM spectra (10° beam) is associated to the first partition of the MFWAM spectra as provided by Meteo-France
- Figure 8-9: Top: wave spectra from SWIM (beam 10°) and their associated partitions (in white, dashed red the first and second partitions, respectively). Bottom: associated wave spectra from MFWAM
- Figure 8-10 : Illustration of collocated wave spectra imaged by SWIM and Sentinel-1
- Figure 8-11: Collocated SWIM and MFWAM spectra with their associated partitions (solid white contour for the first partition, dashed red contour for the second one)
- Figure 8-12: (a) Omni-direction spectra (m2s) from the Brittany buoy (47°33'0" N 8°28'12"), MFWAM and SWIM (3 beams the red, brown and yellow curve as indicated in the insert) on 19 August 2019 18:00 UTC. (b, c,d) directional spectrum from (b) the buoy, (c) SWIM beam 10°, (d) MFWAM
- Figure 8-13: Omni-direction spectra (m2s) from the Yeu Island buoy (46°49,993'N, 02°17,700'W), MFWAM and SWIM (3 beams with the red, brown and yellow curves as indicated in the insert) on 19 August 2019 18:00 UTC
- Figure 8-14: Same as Figure 8-12 but for a location close to the Brittany buoy (47°33'0" N 8°28'12" W) on July 24<sup>th</sup> 2019, 18:00UTC
- Figure 8-15 : Modulation Transfer function versus collocated significant wave height (from ECMWF here), for MTF1 (left) and MTF3 (right).
- Figure 8-16: Mean slope spectra inversed from SWIM 10° radar beam observations as explained in section 8.5.1, in comparison with time-spatial collocated Wave Watch III model for four different wind speeds.
- Figure 8-17 : Significant wave height bias map for the run of the model MFWAM with the assimilation of nadir SWH and wave spectra from beam 6° for the period starting from 26 April until 20 May 2019.

The validation is performed with altimeters Jason-3, Saral and Sentinel-3A and 3B. The maximum range of bias is roughly 60 cm.

Figure 8-18 : Significant wave height bias map for the control run of the model MFWAM without assimilation for the period starting from 26 April until 20 May 2019. The validation is performed with altimeters Jason-3, Saral and Sentinel-3A and 3B. The maximum range of bias is roughly 60 cm.

Figure 8-19 : Difference of mean wave periods from runs of the model MFWAM with and without assimilation of SWIM nadir SWH and wave spectra from beam 6° on 7 May 2019 at 06:00 UTC. Red and blue colors stand for underestimation and overestimation of the model MFWAM.

## LIST OF TABLES

Table 1 : In-flight observations of the SWIM instrument Point Target Response compared to the specifications

Table 2 : SWIM functional validation and instrument performances

Table 3: Binning characteristics for each SWIM incidence beam in L1A products

Table 4 : Proportion of measurements with the flag on concavity of the shape of  $\sigma_0$  profiles equal to 0 or to 1, either using the measured antenna gain or using the combined measured/simulated gain for the antenna gain correction. Statistics are computed over one cycle of data (13 days).

Table 5: Nind and  $\delta r$  parameters as estimated from the speckle analysis and as currently used in the CWWIC products. The number of range gates used in the on-board integration process is also indicated ( $L_{dis}$ )

Table 6: Statistical scores for the comparison between the wave parameters (significant wave height  $H_s$ , dominant direction, dominant wavelength) of the MF-WAM wave spectra partitions and of the SWIM spectra partitions. The data set covers from April 25<sup>th</sup> to June 10<sup>th</sup> 2019 processed with version 4.3.0

## ACRONYMS AND ABBREVIATIONS

Acronyme	Signification
AOCS	Attitude and Orbit Control System
CAL/VAL	Calibration/Validation
CFOSAT	China France Oceanography SATellite
CLS	Collecte Localisation Satellite
CNES	Centre National d'Etudes Spatiales
CWWIC	Cnes Waves & Wind Instrument Center
ECMWF	European Centre for Medium-Range Weather Forecasts
DPU	Digital Processing Unit
FROGS	French Oceanographic Ground Segment
IWWOC	Ifremer Wind and Waves Oceanic Centre
GPM	Global Precipitation Mission
LATMOS	Laboratoire ATmosphères et Observations Spatiales
LOPS	Laboratoire d'Océanographie Physique et Spatiale
LUT	Look Up Table
MFWAM	Meteo-France Wave Model
MSS	Mean Square Slopes
ODL	Ocean Data Lab
PRF	Pulse Repetition Frequency
PTR	Point Target Response
PUG	Product User Guide
SWIM	Surface Waves Investigation and Monitoring
SCAT	SCATterometer
SNR	Signal to Noise Ratio
SWH	Significant Wave Height
WS	Wind Speed

**Reference :** CF-SYMI-NT-3572-CNES

**Issue :** 1.0

**Date :** 2019\_09\_17

## 1 - INTRODUCTION

The aim of this document is to provide the data users of CFOSAT/SWIM products with a preliminary synthesis on performances of the SWIM instrument and products. This document is written at the end of the SWIM commissioning phase, i.e. 7 months after the first data sets were delivered by CNES to the French scientific expert groups which contribute to the post-launch verification phase (at LOPS, LATMOS, Meteo-France). These three expert groups in France, implemented complementary methods to analyze the data. In addition to the CNES team and to these three expert groups, three small companies contributed to this analysis, namely ODL, ACRI-ST and CLS in coordination with CNES and the above-mentioned groups.

The analyses carried out with this first data set followed the objectives and methods explained in the CAL/VAL plan [R1].

Data sets used to write the present synthesis were taken mainly from the period after April 25<sup>th</sup> 2019, a date which corresponds to a major modification in the real-time processing of the SWIM raw data on-board de satellite. Indeed, during the first part of the CAL-VAL activities (until 25 April), a problem was identified in the wave products and has been attributed to an error in the on-board algorithm dedicated to the range migration compensation during temporal integration of the raw signals. This error induced a degradation of the effective surface resolution (after time integration) with respect to the specification. This error has been corrected on April 25<sup>th</sup> 2019. All the conclusions given in this report regarding the L1b and L2 off-nadir products come from data recorded after April 25<sup>th</sup>. In certain cases, conclusions on L2\_nadir and L1a were drawn using data sets prior to April 25<sup>th</sup>, but are not affected by the change in the real-time processing. Note that due to this on-board processing correction, datasets acquired before April 25<sup>th</sup> 2019 will not be disseminated to users. If required for specific studies, provision for data sets prior to April 25<sup>th</sup> 2018 will be evaluated by CNES (product level, application, ...) upon request.

We remind that presently systematic products are produced by two French centers

- the CNES CWWIC center which provides L1A, L1B, and L2 products in near-real-time (less than 3 hours after acquisition). The data sets analyzed for the present study have been produced by incremental versions of the processing chain as described in Appendix B.
- the IFREMER IWWOC center which will provide alternative L2 products (called L2S) in deferred time (up to 48 h after acquisition).

This document is focused on the analysis of the data SWIM products, from Level 1a (normalized radar cross-sections) to Level 1b (fluctuation of these normalized cross-sections and associated fluctuation spectra) and Level 1 (wave spectral properties and nadir products). We do not present in detail the processing algorithms used to obtain these products, but when necessary they are briefly summarized. More details can be found in the Product User Guide (or PUG, [R2] or in [R3]). Similarly, note that only a subset of product variables is discussed below. For a complete list of variables and flags, please refer to the PUG or to the heading of the Netcdf data files.

It is not the purpose of this document to present the mission performance. In a few words we can just write that everything is nominal, and in particular the orbit follows the specification. In order to fulfill

the requirement of maintaining the track positions at  $\pm 20$  km, maneuvers of the satellite are carried by the satellite control center (China) every 40 to 45 days (see Figure 1-1)

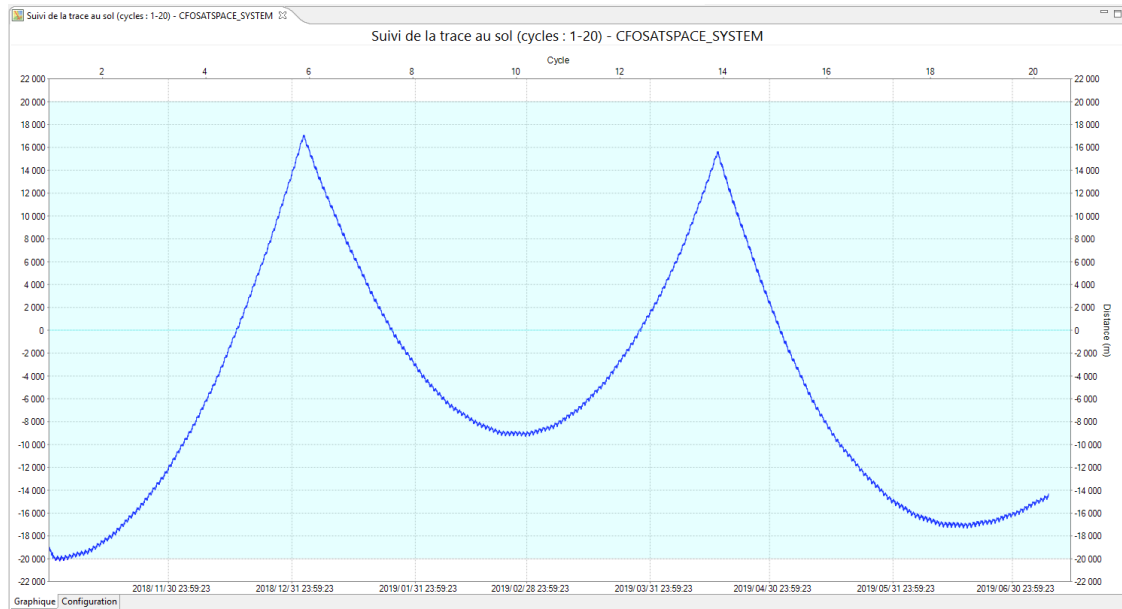


Figure 1-1 : Position of the CFOSAT nadir track ( in km, relative to the nominal position) as a function of time (from November 2018 to mid-July 2019). The track is maintained at  $\pm 20$  km with respect to its nominal position thanks to maneuvers of the satellite every 40 to 45 days.

This document provides a summary on

- SWIM instrument functional validation ([section 2](#)),
- SWIM instrumental performances ([section 3](#)),
- performance of the data delivery chain from satellite to the CNES Mission center ([section 4](#)).

Then it presents the methods and the results on

- nadir products (from the  $0^\circ$  pointing beam of SWIM)- [section 5](#),
- the normalized radar cross-sections (from all the SWIM beams from  $0$  to  $10^\circ$  incidence)- [section 6](#) ,
- the fluctuations of radar cross-sections and their spectra within the footprint (from all the beams except the nadir beam) – [section 7](#). These latter belong to the L1b product of the CWWIC products and are intermediate variables analyzed by the IWWOC center.

Finally, preliminary comments on the L2 non-nadir products are given ([section 8](#)).

## 2 - SWIM FUNCTIONAL VALIDATION

All the SWIM instrumental behavior are satisfying. We can mention in particular:

- a very stable electric consumption at a level (185 W) consistent with the predictions made before launch (192 W)
- temperature behavior of SWIM subsystems in agreement with specifications
- low rate of alarms due to radiation effect: less than 1 per day, and located over the Atlantic anomaly region, as expected (see Figure 2-1).
- the instrument operating point is validated, the PRF evolution along the track follows the specification and allows a very good signal acquisition.
- SWIM functioning modes all tested successfully
- Nominal Antenna rotation and stable antenna rotation speed

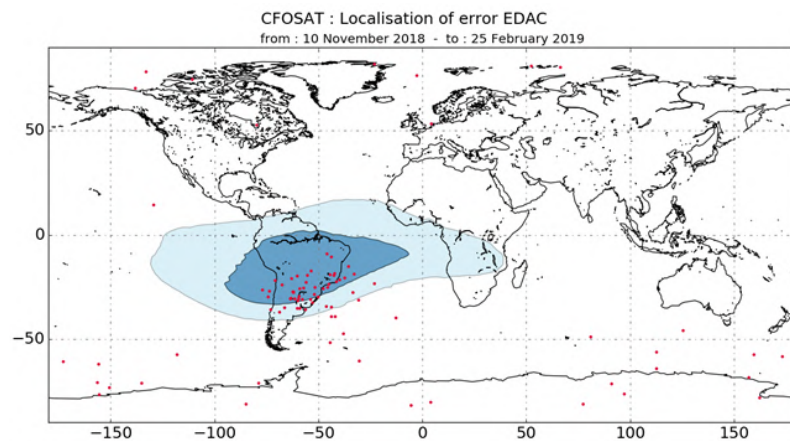


Figure 2-1 : Localization of EDAC errors (red points). In blue: the Atlantic anomaly region

The only current anomalies concern non-permanent signal transmission perturbations between the rotating plate (RFA) and the fixed part of the instrument. These anomalies identified since the end of March 2019 remain scarce and their frequency has decreased since the beginning of June 2019, after the problem was well characterized and mitigated by changing the temperature (see below). These perturbations (named micro-cuts, hereafter) impact different analog signals from the RFA (Rotary Feed Assembly) sub-system. In particular it was observed that it affects:

- The command for thermal control of the RFA: This induces short unnecessary activations of the redundant heater of the RFA
- The commands of the feed horn switch: this induces either a reset of the switch (without significant impact on tracking nor on the data) or a loss of transmitted pulses during acquisition cycles. This latter effect biases the intensity of the signal when integrated on board (echo). This effect is shown in the Fig 2.2 below for the 4° beam and an anomaly observed on the 17<sup>th</sup> April 2019.

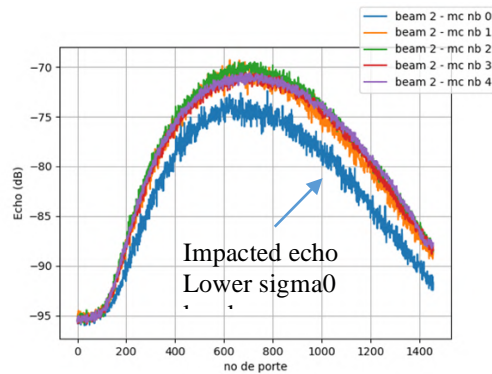


Figure 2-2 : Echo power of beam 4° for 5 successive macrocycles on April 17<sup>th</sup> 2019. In this selected example, the perturbation of signal transmission induces by a micro-cut induces a loss of power, illustrated on the blue echo (due to lost pulses for the macrocycle configuration). However, the occurrence of this perturbation is scarce (see Fig 2.3)

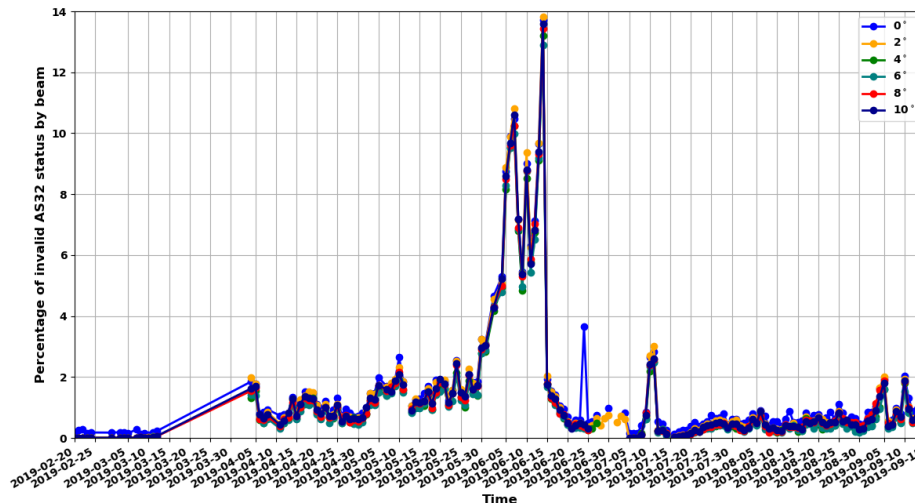


Figure 2-3 : Statistics of inconsistencies between switch matrix status (status of the actual beam performing the measurements) and command (instruction of the beam performing the measurements)

This phenomenon is now monitored using several statistics:

- Percentage of Switch Matrix status inconsistency w.r.t command. Two types of switch matrix dysfunctions are identified and monitored:
  - Incoherence between command and status: feed command applied is not the one as expected
  - Switch matrix reboot because the switch matrix status observed is in 'DFLT\_MODE\_NADIR\_2'
- Percentage of echo or normalized radar cross-section ( $\sigma_0$ ) profiles impacted by the micro-cuts (ie showing a general decrease over the whole swath).

As molecular degassing was suspected to generate these micro-cuts. Therefore, it was decided to increase the RFA sub-system temperature by 5°C to eventually reject the contaminating gas particles. This action performed June, 14<sup>th</sup>, 2019 enabled to significantly decrease the rate of micro-cuts and the impact on  $\sigma_0$  profiles.

This is illustrated in the following Figures (2.3 and 2.4). Figure 2.3 shows the switch matrix status versus command inconsistency rate from February, 20<sup>th</sup> to July, 5<sup>th</sup>, and Figure 2.4 shows the rate of impacted

$\sigma_0$  profiles over the same period. Statistics are computed for each beam for both monitored parameters. These plots show that the switch matrix status inconsistency rate decreased drastically from 14% to less than 1% since the increase of RFA temperature, and the rate of impacted  $\sigma_0$  profiles, has decreased similarly. These results confirm the molecular degassing assumption and let us hope a full extinction of the micro-cuts within a few weeks or months. At the date of editing this report (September 2019), the situation is stabilized.

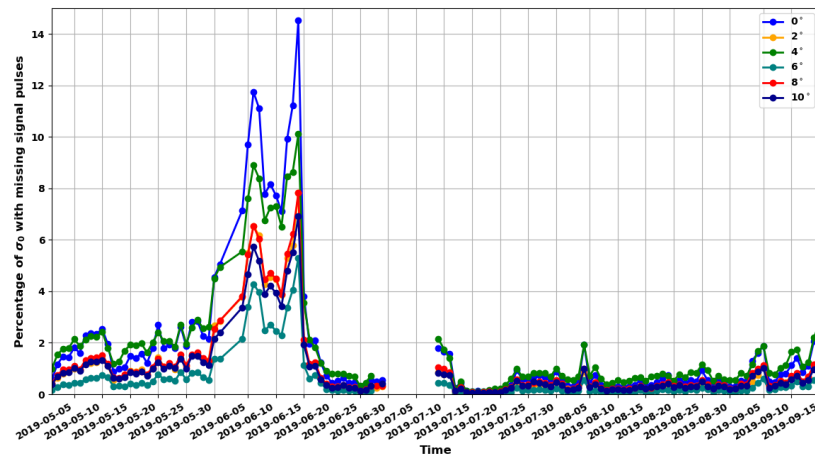


Figure 2-4 : Rate of  $\sigma_0$  profiles impacted by the signal anomaly in the signal transmission between rotating plate and fixed part of the instrument (decrease of  $\sigma_0$  energy over the whole swath)

Because the anomaly may impact the geophysical products ( $\sigma_0$ , and potentially wave products), a new flag will be added in the level 1A products to indicate whether the  $\sigma_0$  from a given beam is impacted or not by the micro-cuts issue. This product will be available in a future version of the SWIM products.

**Reference :** CF-SYMI-NT-3572-CNES

**Issue :** 1.0

**Date :** 2019\_09\_11

### 3 - SWIM INSTRUMENTAL PERFORMANCES

The instrumental performances are all nominal as detailed below.

The Point Target Response (PTR) function is stable and all the derived parameters are compliant with the specifications. Figure 3-1 illustrates an example of the PTR function measured during an internal calibration sequence (blue curve) and its comparison with respect to a theoretical PTR (red curve), as well as the various parameters checked to validate the measured PTR. Their validation is listed in Table 1 below.

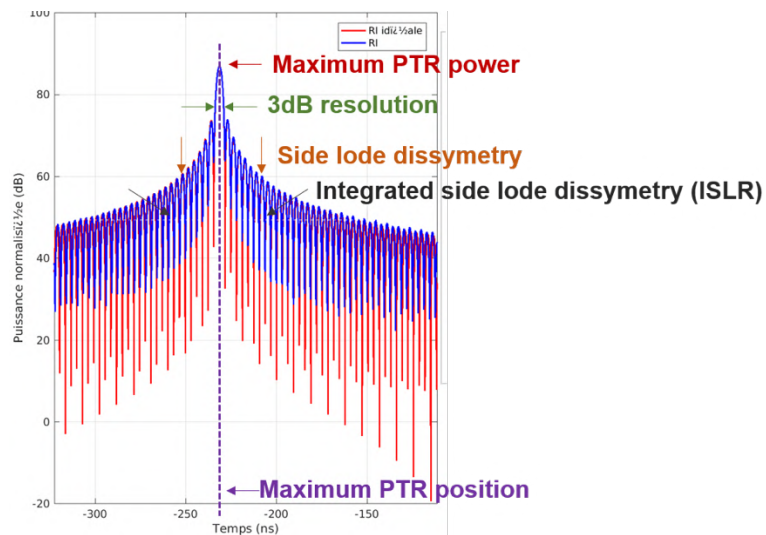


Figure 3-1 Theoretical (red curve) and measured (blue curve) Point Target Response (PTR) function during an internal calibration sequence, and its derived parameters.

Characteristic	Specifications	In-flight observations
Maximum power	Variation < 1dB	Variation < 0.2dB
3dB resolution	2,77 ns $\pm$ 5% (0.136ns)	2.7875 < 0.005ns
Secondary lobes dissymetry	$\Delta$ SL1, $\Delta$ SL2, $\Delta$ SL3 < 2dB $\Delta$ SL4, $\Delta$ SL5 < 4dB	<1dB
Side Lobe Ratio (ISLR)	10,15 dB $\pm$ 20% (2.03dB)	10.10 $\pm$ 0.05 dB

Table 1 : In-flight observations of the SWIM instrument Point Target Response compared to the specifications

- The wave forms over the ocean are fully consistent with expectations (see Figure 3-2)
- The performance of the on-board tracker is excellent (see Figure 3-3). This tracker, similar to Poseidon 3 instruments (Jason2, Jason3), is excellent over ocean and presents also good performances over land, only high relief areas are less covered, which has no impact on the mission. Thanks to CFOSAT orbit SWIM acquires data up to 82° of latitude.

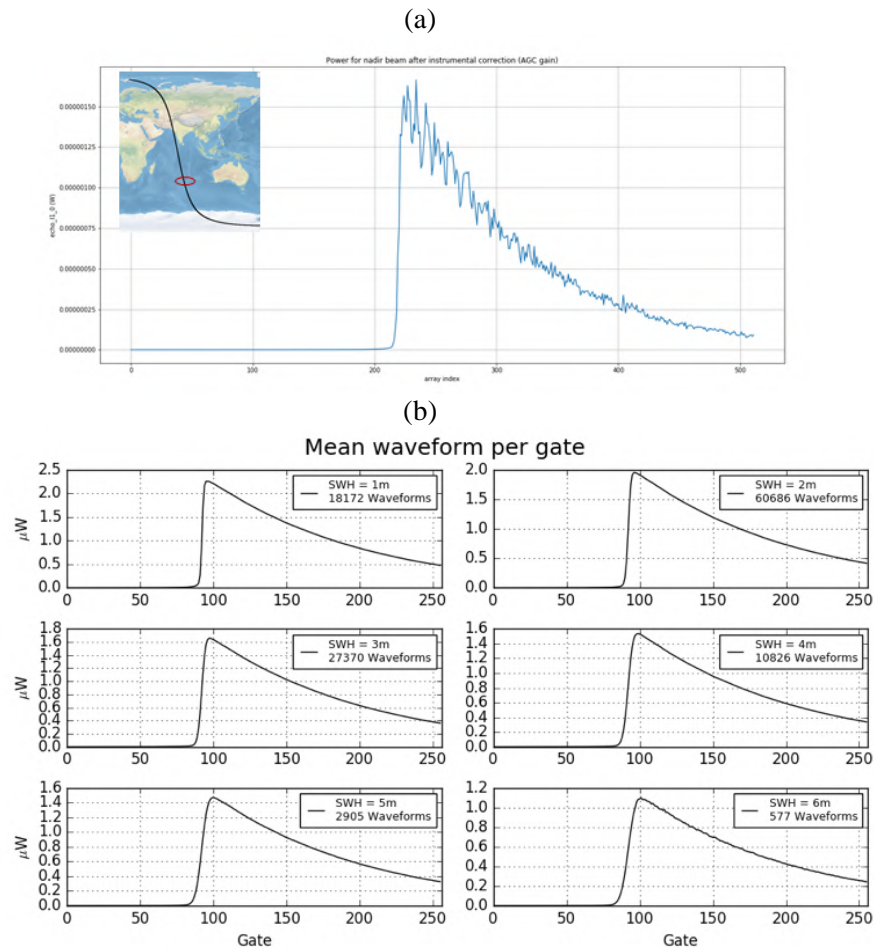


Figure 3-2 : (a-top) Example of a typical nadir wave form over the ocean (raw data). (b-bottom) 1-day averaged wave forms of the nadir signal shown per class of significant wave height (from 1 to 6 m)

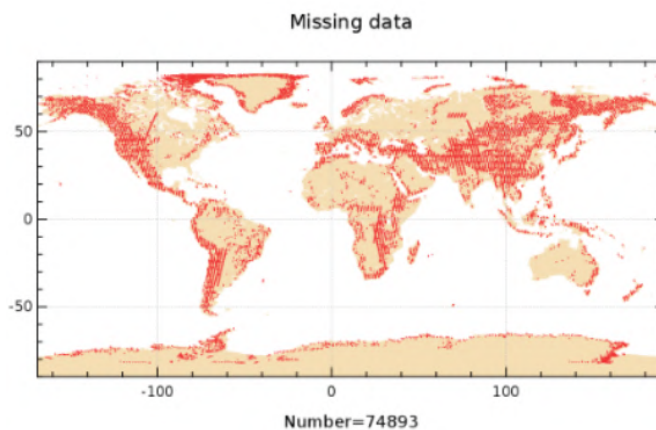


Figure 3-3 : SWIM nadir tracking coverage (percentage of successful tracking with the on-board algorithm) over one cycle.

- The rotation speed is compliant with specifications (5.6 rpm with an error less than the measured least significant bit).

- Instrumental Gain: SWIM instrumental gain estimated through specific calibration sequences shows less than  $\pm 0.5$  dB difference with respect to the pre-launched values (less than 1% difference) and remains very stable with time.
- Instrument calibration: all calibration modes (internal calibration, antenna calibration and AGC calibration) of the instrument were tested during 4 days every 4 hours. Internal and antenna calibration show very stable performances in time and with respect to thermal variations. However, AGC (Automatic Gain Control) calibration presented a small (up to 0.3dB and less than 0.05dB expected) temporal variation for some AGC steps estimation and a small temporal variation on calibration power (up to 0.11 dB and less than 0.05 dB expected) for high AGC steps. Nevertheless, in the range of AGC steps actually encountered in the tracking mode, these variations are less than 0.15 dB and have a negligible impact on sigma0 profiles. This small issue is presently under investigation.
- Thermal noise: Until July 2019 (version 4.3 of the processing), the thermal noise was estimated for each macrocycle from the nadir echo, by averaging the noise floor in the first 60 range bins. It was then extrapolated to off-nadir beams. Due to an in-flight Signal to Noise Ratio stronger than foreseen on-ground, the noise floor is blemished by the Impulse Response side lobes for most of the nadir echoes (more than 99%), see Figure 3-4. This induces an error on the estimated nadir-beam thermal noise reaching 0.6dB and corresponding to a 0.14dB error on the normalized radar cross-sections  $\sigma^0$  (in the worst case: for the 10° beam and 7dB SNR). To minimize this error, a modification was made to estimate the thermal noise based on the 2° beam echoes, for which the noise floor is free of IR side lobes (lower SNR and larger noise floor in gates). This is illustrated in Figure 3-4. This modification is available since version 4.3.1 of SWIM products. This lowers the estimation error when extrapolating the thermal noise to the nadir and the other off-nadir beams, and thus lowers the impact on sigma0 to 0.11dB error (in the worst case: for the 10° beam and 7dB SNR). The impact of scene heterogeneity was also assessed as the propagation algorithm used to estimate thermal noise at all beams and for each macrocycle (propagation from a reference beam – the 2° beam - to other beams) is based on a homogeneous scene assumption. In-flight measurements in CAL2 mode (reception-only mode) were performed over a North Atlantic area where both the Labrador current and the Gulf Stream converge. The received power, equivalent to brightness temperature at Ku-band, shows a high impact of the scene heterogeneity on thermal noise, reaching 1 dB in the worst case. However, such areas remain scarce and the impact can be much lower. Thus the impact of the heterogeneity of the scene is thus not considered in the propagation of thermal noise to the other beams.

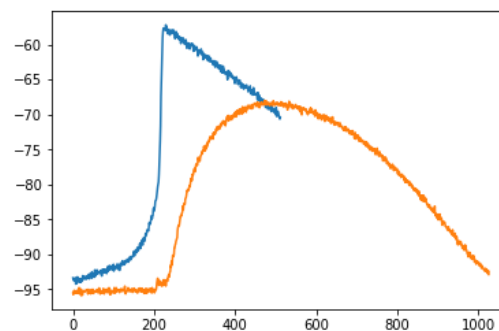


Figure 3-4 : Typical echo (amplitude in dB as a function of range gate number) over the ocean from the nadir beam (blue) and 2° beam (orange). The noise floor is determined from the first range gates. Starting with version 4.3.1. of the processing the 2° beam is used instead of 0°.

A summary of the functional validation and instrument performances is presented in Table 2.

SWIM Functioning or performance	Comparison with requirement
Consumption	OK
Temperature	OK
Alarms	OK
Instrument operating point	OK
Antenna rotation speed	OK
Mispointing	OK
Signal transmission behavior	X anomaly identified: may have temporary affected up 14% of the scientific data ( $\sigma^0$ ) but was mitigated in June 2019.
Point Target Response	OK
Internal Calibration	OK
Antenna Calibration	X to be further assessed
Instrumental Gain and Noise	OK

*Table 2 : SWIM functional validation and instrument performances*

#### **4 - DATA DELIVERY TO THE CNES MISSION CENTRE**

The CFOSAT data are recorded on-board and transmitted to the ground segment using two polar receiving stations (Kiruna and Inuvik) operated under CNES supervising and 3 mid-latitude stations in China operated under NSOAS supervising. The two French polar stations deliver in Near-Real Time the data to the French Mission Center (CWWIC). Then, the CWWIC processes the telemetry to generate SWIM and SCAT products. Starting July 16<sup>th</sup> 2019, the CWWIC chain used the 4.3.1 version of the SWIM processor; this version includes corrections of anomalies evidenced during the verification phase and/or evolutions of algorithms or of input files decided by considering the results of the verification phase. The currently running version 4.3.2 includes additional small corrections (see appendix B).

Since beginning of July 2019, SCAT products are generated at CNES, using version 1.0.2 of the Chinese processor. Work is going on to integrate the updated version of the Chinese SCAT processor (now in 2.0 version).

The SWIM product availability is 100% (maneuvers excluded), and since last December 2018, 89% of the products were delivered within the Near Real Time (NRT) delay of less than 3 hours.

**Reference :** CF-SYMI-NT-3572-CNES

**Issue :** 1.0

**Date :** 2019\_09\_11

## 5 - NADIR PRODUCTS (L2A)

### 5.1 VARIABLES ANALYZED

In a way similar to the cases of satellite altimeter missions, geophysical parameters from the nadir echo waveform over the ocean are inverted by applying a “retracking” algorithm based on the fit of a Brown model echo [R4] to the recorded waveforms. However, for SWIM no information is provided on the epoch or height because CFOSAT is not an altimeter mission (no precise orbit determination, no microwave radiometry nor dual wavelength measurement for delay correction). Over ocean surfaces, the main geophysical products are hence the significant wave height (SWH), the normalized radar-cross-section  $\sigma^0$ , and the wind speed (WS). As explained below, thanks to the implementation of a new algorithm in the French ground segment, an additional parameter will tentatively be provided as output of the retracking, namely the parameter « mean square slope » of the waves.

The following paragraph is about the analysis performed on this new algorithm called “Adaptive algorithm”. Validation of the nominal retracking (based on ICE-2) has still to be performed; especially, look up table have to be established.

The “adaptive” algorithm [R5] implemented in the French ground segment has three specificities with respect to algorithms currently used for most of other altimeter missions:

- it considers the real point target response (estimated from on-board calibration sequences) instead of a theoretical function;
- mean-square slopes (MSS) of the waves are taken as an output of the fit to the Brown model; this step implies that instead, possible mispointing is given as a priori values of the inversion;
- minimization is carried out according to the Nelder-Mead method [R6] instead of the Newton-Raphson method.

The retracking is performed at the rate of the nadir echo acquisition (every 220 ms in the nominal mode of SWIM acquisition), and the geophysical products are provided either as “native” values (at 4.5 Hz), or as averaged values. Three types of averaged values are provided:

- mean values over 1 s of data. The variables ‘xx’ in the SWI\_NRT products are called “nadir\_xx\_1Hz” in this case.
- mean values over 4,5 s of data (called NSEC data), which corresponds to the time interval over which the number of averaged parameters is equivalent to the 1s averaged product of standard altimeter missions- like Jason3). The variables in the SWI\_L2 products are called “nadir\_xx\_NSEC” in this case.
- mean values associated to wave parameter “boxes” of about 70 km along the track (the boxes are geographic cells of about 70 km along-track where all the wave products are grouped- wave spectra and SWH). The variables in the SWI\_L2 products are called “nadir\_xx\_box” in this case.

In the nadir product, a rain flag is provided (see [R2]). The processing method follows the principle proposed by Tournadre and validated for AltiKa data [R7]. This method was adapted to SWIM specificities before launch. During the first months of the mission, a first tuning was established. As shown in section 5.3.6, the nadir rain flag associated to version 4.3.1 of the data processing can already be used for rain event detection even if it may be refined in the future. Improvement on bloom event detection is under specification.

For the analysis on the first data sets (before version 4.3.1 of the processing chain), the mispointing used

as input of the adaptive retracking algorithm was taken by error as AOCS pointing orders instead of mispointing angles estimated from the L1a non-nadir products (see section 6.3.1). This implies that the mss could not be exploited until data sets were produced by version 4.3.1. Preliminary results are provided in section 5.3.7 using data sets produced with the 4.3.1 version.

In order to provide synthetic information characterizing the nadir echo over all scenes (ocean or continental scenes), two other algorithms, called ICE1 and ICE2 are implemented in the processing chain. However, the products of this processing have not yet been analyzed in details because priority has been put on ocean data.

## 5.2 VALIDATION METHOD AND DATA SETS USED FOR ANALYSIS

The quality of the adaptive retracking algorithm has been checked first by its coverage, it has been compared to the conventional altimetry algorithm (MLE4).

Until now, the validation was focused on SWH and  $\sigma^0$  variables obtained with the adaptive algorithm. Analyses were performed on NSEC data for one CFOSAT orbital cycle, except for spectral analysis which is performed on native data.

Validation of SWH has been carried out by comparing to wave model data (ECMWF short-term forecasts as provided in the auxiliary files and on MFWAM model forecasts). The estimation noise has been evaluated via spectral analyses.

## 5.3 MAIN RESULTS

### 5.3.1 RETRACKING ALGORITHM PERFORMANCE

In addition to the onboard tracking performances (see section 3 - ), the adaptive retracking provides excellent performances in terms of algorithm convergence: it converges on more data than conventional altimetry algorithm (see Figure 5-1).

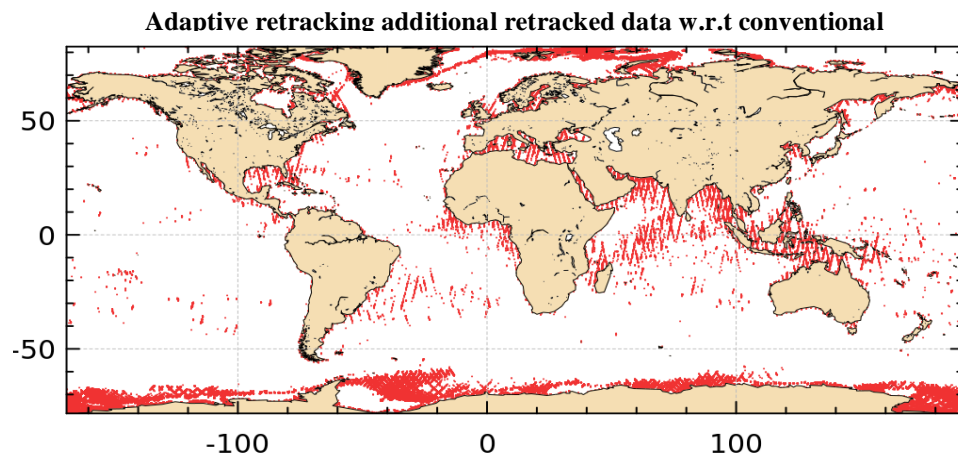


Figure 5-1 : Map of additional retracked data (red points) obtained with the adaptive retracking with respect to the conventional altimetry retracking (MLE4) over a 13 day cycle.

### 5.3.2 SIGNIFICANT WAVE HEIGHT

The adaptive algorithm provides very positive results in terms of SWH as illustrated in Figure 5-2 to Figure 5-4 . The comparisons to model show a remarkable consistency with a very weak and stable bias (less than 1 cm with respect to ECMWF SWH over 6 months (Figure 5-2); this bias is only slightly variable with wave height. As shown by Figure 5-3, compared to MFWAM, the bias is only 1cm and a standard deviation 28 cm. The comparison with altimetry missions Jason 3 and AltiKa (Figure 5-4) also shows a very good consistency with a mean difference of about 6 cm w.r.t Jason 3 (standard deviation of 34cm) and less than 1 cm w.r.t. AltiKa (standard deviation of 35cm).

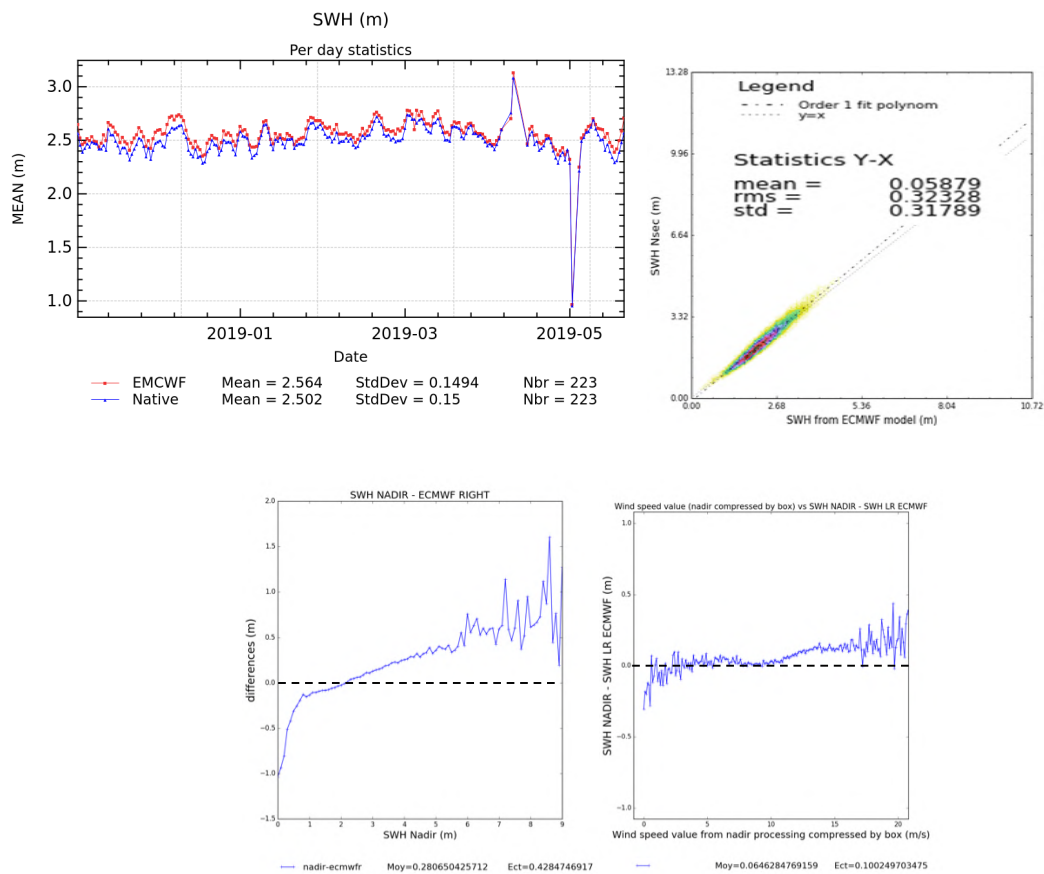


Figure 5-2 : top: SWIM nadir SWH (NSEC data) compared to ECMWF SWH for a 13 day period. Top left: time-series of the differences (SWIM\_nadir-ECMWF). Top Right: scatter plot (SWIM nadir versus ECMWF). The mean bias is 12 cm. Bottom: mean difference between nadir and ECMWF SWH as a function of nadir SWH (left) or wind speed (right).

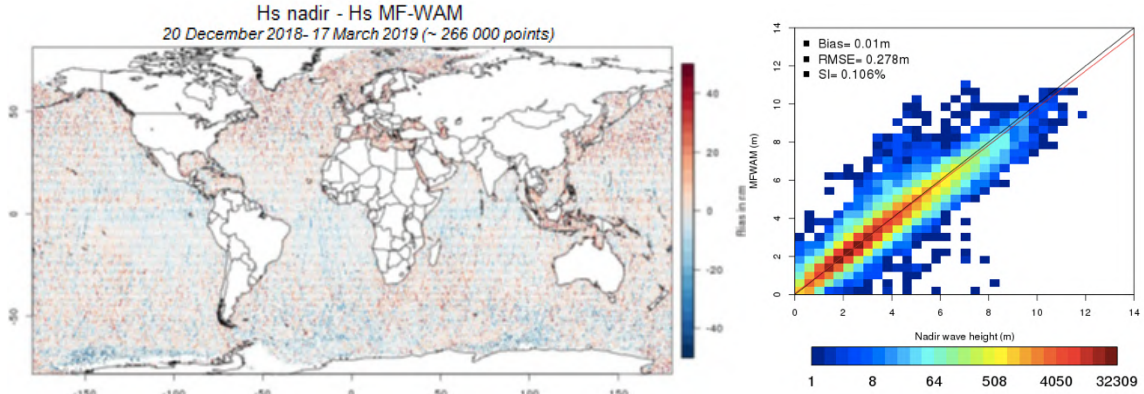


Figure 5-3: SWIM Nadir SWH (product at the scale of each wave box) compared to the MFWAM model SWH. The considered data set covers the period from 20th December 2018 to 17th March 2019 and includes 266 809 samples. Samples corresponding to  $\sigma^0$  values less than 5 dB or greater than 25 dB have been filtered out, as well as SWIM SWH which have a standard deviation larger than 0.6 m.

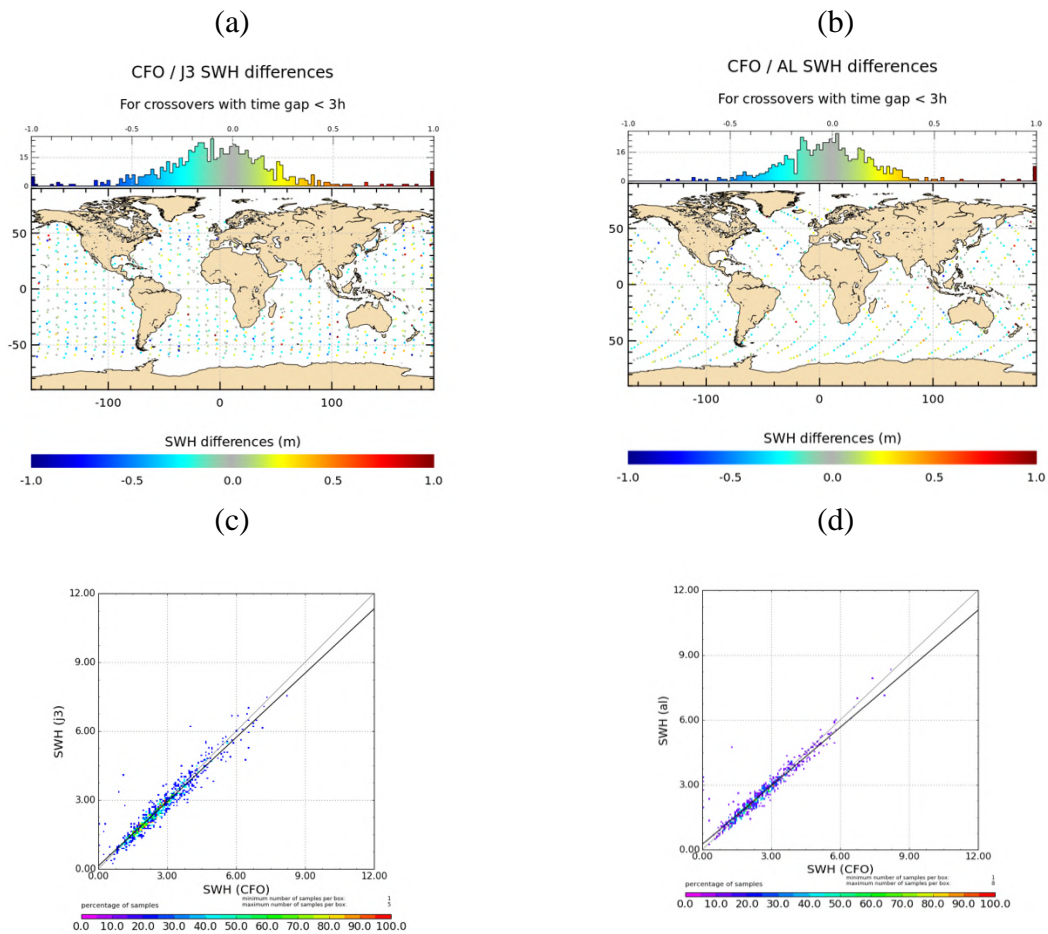


Figure 5-4: Top: Map of differences in Hs between CFOSAT and Jason 3 (a) and AltiKa (b) at cross over points. Corresponding scatter plots : Jason 3 versus SWIM (c), AltiKa versus SWIM (d).

### 5.3.3 SIGMA0

The SWIM nadir sigma0 presents very good results. The comparison with altimetry missions Jason 3 and AltiKa (Figure 5-5) shows:

- a remarkable consistency with the Jason 3 Ku-Band instrument with a mean difference of about  $0.12\text{dB} \pm 0.43\text{ dB}$  w.r.t Jason 3 (correlation coefficient of 0.93);
- a mean difference with the AltiKa Ka-Band instrument of about  $-2.77 \pm 0.7\text{ dB}$  with some latitude dependency; this is expected due to difference in the radar frequency and the different sensitivity to wind speed (Ku-Band vs Ka-Band, see eg [R11]).

The observed variations of SWIM nadir  $\sigma^0$  over the Arctic (Figure 5-6) are consistent with the sea-ice extent from ECMWF, and patterns observed are relevant for this area; for instance, we can observe an area of lower  $\sigma^0$  values corresponding to the multi-year ice region characterized by a higher roughness.

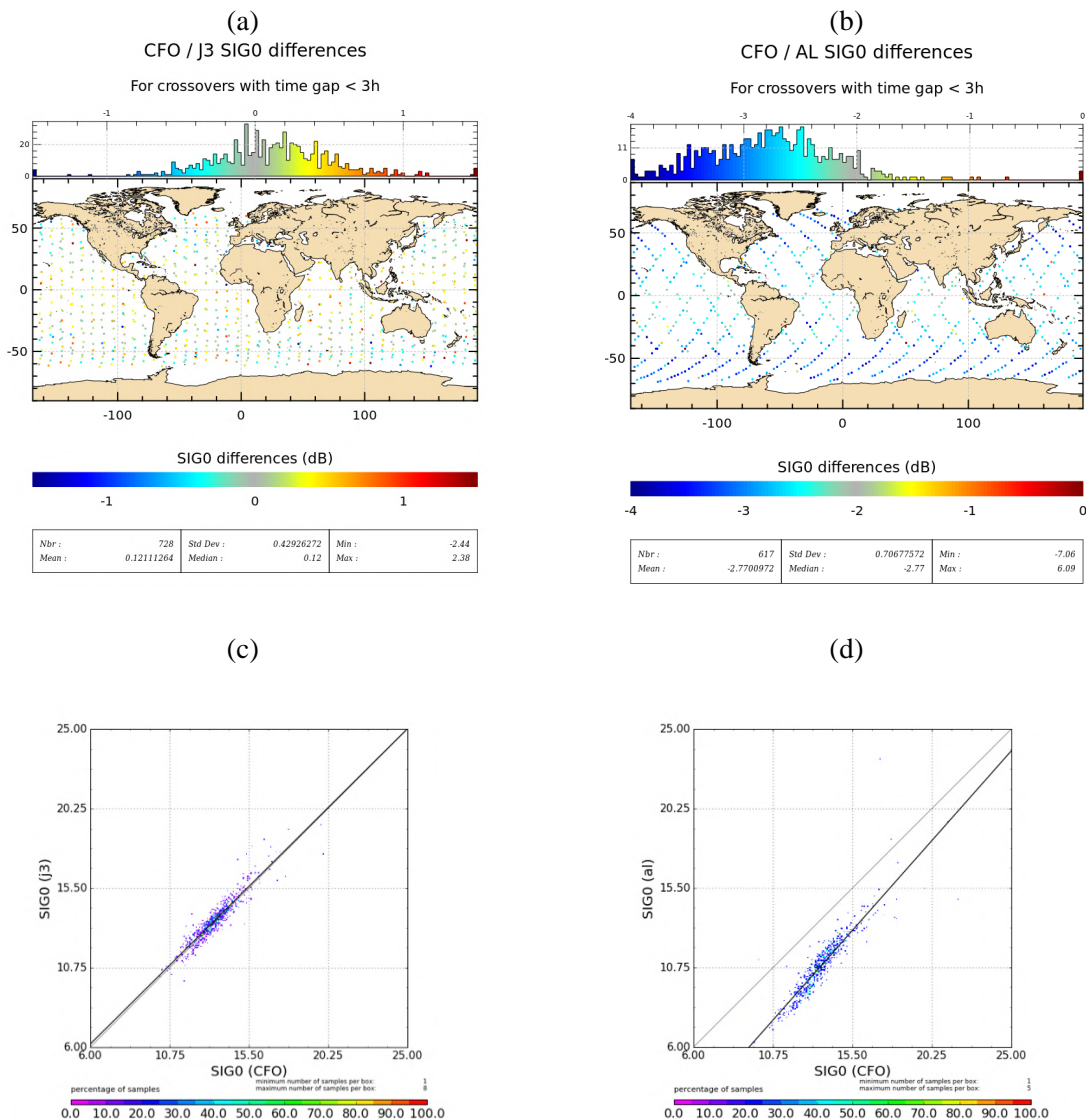


Figure 5-5: Map of  $\sigma^0$  differences points between CFOSAT and Jason 3 (a) and AltiKa (b) at crossover points. Corresponding scatter plots (c) Jason 3 versus SWIM, (d) AltiKa versus SWIM

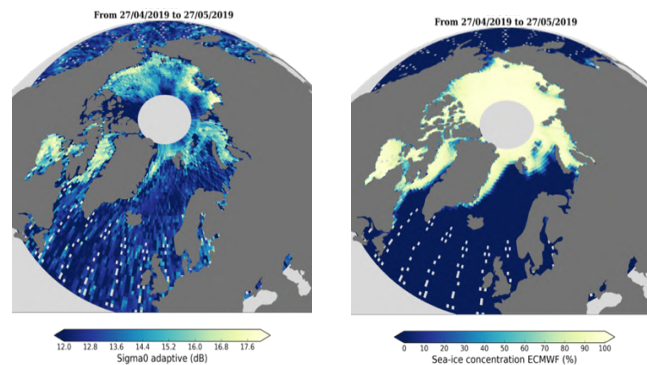


Figure 5-6: left: Swim nadir  $\sigma_0$  values over the Arctic from 2019/04/27 to 2019/05/27, right: ECMWF sea-ice cover over the Arctic from 2019/04/27 to 2019/05/27

### 5.3.4 IMPROVEMENT WITH RESPECT TO THE CONVENTIONAL ALTIMETRY PROCESSING

Adaptive retracking has been implemented in order to reduce the impact of the low nadir measurement rate on SWIM (due to the multiple beam sampling). This paragraph shows the improvement and the positive impact with respect to the conventional altimetry processing, namely MLE4.

Concerning the significant wave height, the overall standard deviation for 1Hz products remains smaller than 10% of the mean value for all wave heights, always smaller than in the case of the MLE4 (see Figure 5-7). Correlatively, this better performance of the adaptive algorithm gives the possibility to catch SWH variability at smaller scales than with the MLE4 algorithm thanks to a reduction of 45% on the noise at the smaller scales (~20 km) compared to MLE4 results (Figure 5-8). Despite the smaller repetition rate of the SWIM nadir raw sampling (5Hz) compared to Jason3 (20 Hz), the SWIM nadir performances are equivalent to the current Jason 3 official products performances (around 20cm noise).

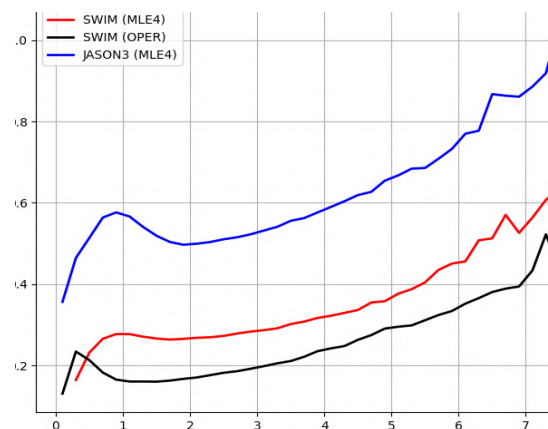


Figure 5-7 : Mean standard deviation of significant wave height as a function of the mean significant wave height for the “adaptive” algorithm applied to SWIM data (black line), MLE4 algorithm applied to SWIM data (red line) and MLE4 algorithm applied to JASON3 data. The SWIM data used for this analysis are 1 Hz-products, the period of analysis is from 24/12/2018 to 5/01/2019 (cycle 5) and data over sea-ice and coastal regions have been filtered out.

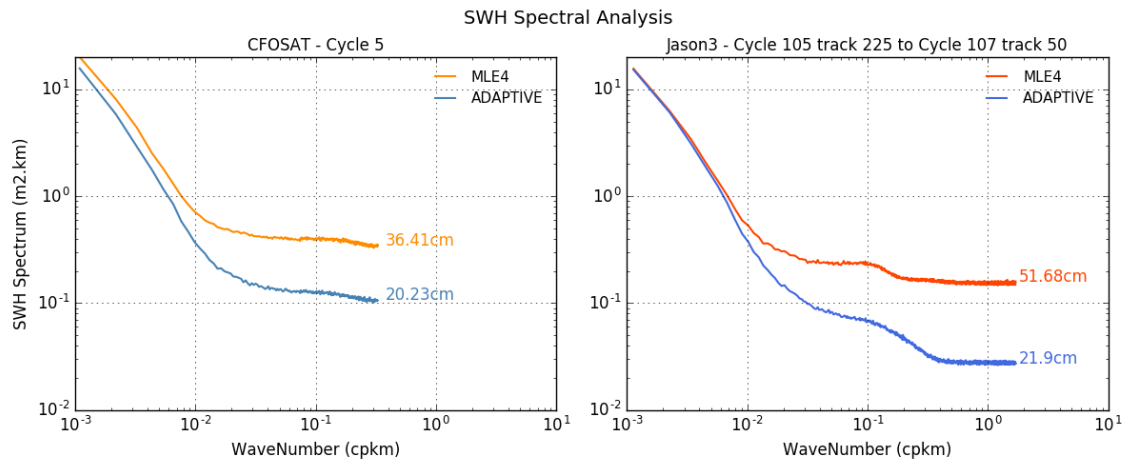


Figure 5-8 : Left-hand side: Density spectrum of the SWIM nadir SWH along-track variability from the adaptive (blue curve) and MLE4 (red curve) retracking algorithms. The noise level is estimated at 20.2 cm for the adaptive method and 36.4 cm for the MLE4. The data set used for this analysis corresponds to the orbital cycle#5. Right-hand side: Same analysis but for one orbital cycle of Jason3.

In terms of  $\sigma_0$ , an important improvement is the suppression of the artificial bump in the spectrum of  $\sigma_0$  variations between 0.06 and 0.15 cpm (Figure 5-9). This “bump” in the MLE4 results is due to the implicit correlation between the  $\sigma_0$  and the other parameters in the MLE4 algorithm. The adaptive model avoids the correlation between  $\sigma_0$  and the other trailing edge parameters, and thus gives access to a more physical  $\sigma_0$ , with no bump in the spectrum. Another improvement is observable with  $\sigma_0$  over rain cell or bloom regions. Figure 5-10 shows the case of a rain event, which is characterized by a decrease of the backscattered power. This implies variations of the Automatic Gain Control values at the instrument level. The adaptive retracking follows well these variation whereas MLE4 does not. The adaptive retracking thus provides more physical  $\sigma_0$  values and improves the detection of special events such as rain cells or blooms.

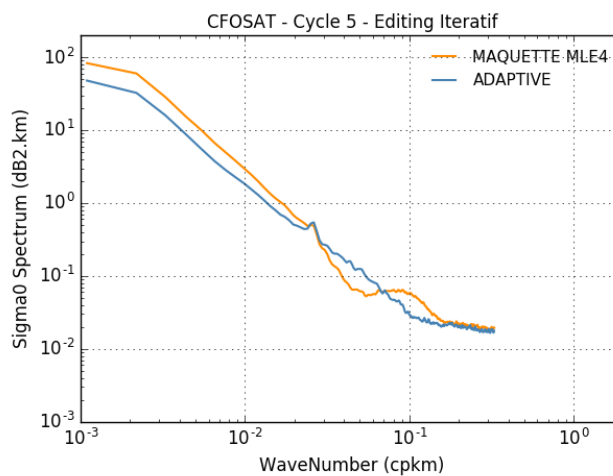


Figure 5-9 : Density spectrum of the SWIM nadir Sigma0 along-track variability from the adaptive (blue curve) and MLE4 (red curve) retracking algorithms. The data set used for this analysis corresponds to the orbital cycle#5

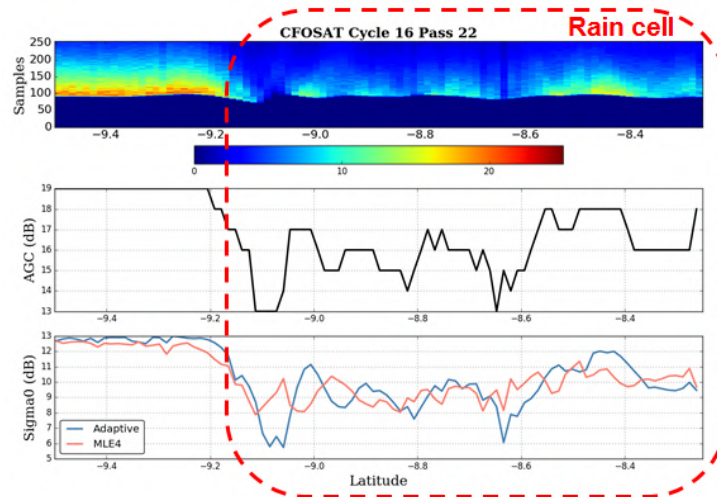


Figure 5-10 : SWIM nadir  $\sigma_0$  values from the adaptive (blue curve) and MLE4 (red curve) retracking algorithms in the case of a rain event. Adaptive values follow the AGC variations (black curve), as physically expected in opposite to MLE4 values behavior.

### 5.3.5 WIND SPEED

Nadir wind speed provided in SWIM products is determined via Collard's algorithm [R8]. This parametric algorithm relating wind speed to  $\sigma_0$  and the significant wave height (SWH) as suggested by Gourrion et al [R9] is used for Jason altimetry missions and has been implemented in SWIM data processing. As shown in Figure 5-11, results of this method are compliant with the specifications with a mean bias of about 0.10 m/s and a RMSE less than 1.2 m/s. However, in order to still improve this wind estimation, a new method has been tested based on the use of a 2D Look Up Table that depends on the pair ( $\sigma_0$ , SWH) as in the Collard's model. A preliminary version of this Look Up Table was computed from cycles 1 to 14 data. ECMWF winds are used as reference to develop this solution as performed for Envisat RA-2 [R10] or for AltiKa [R11]. Preliminary results are encouraging: as shown in Figure 5-12, this method improves the consistency with ECMWF data, especially at low to moderate winds. Another important result is the improvement in the estimation of wind variability. With this new method, this variability is larger than that from the ECMWF model (Figure 5-13) which is consistent with what we expect from altimeter observations compared to model data.

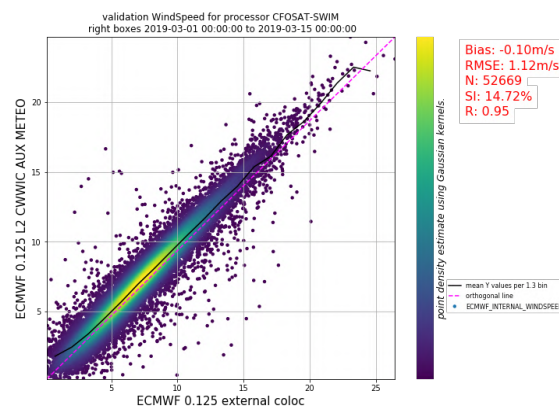


Figure 5-11 SWIM nadir wind speed compared to ECWFM wind speed.

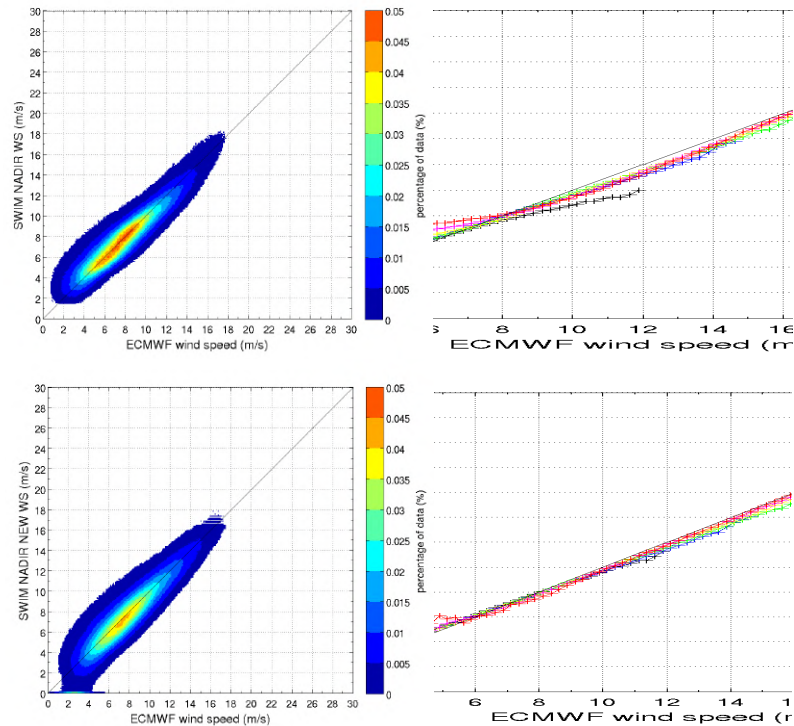


Figure 5-12 SWIM nadir wind speed compared to ECMWF wind speed: Top: current SWIM product data; Bottom: results using the preliminary Look Up Table.

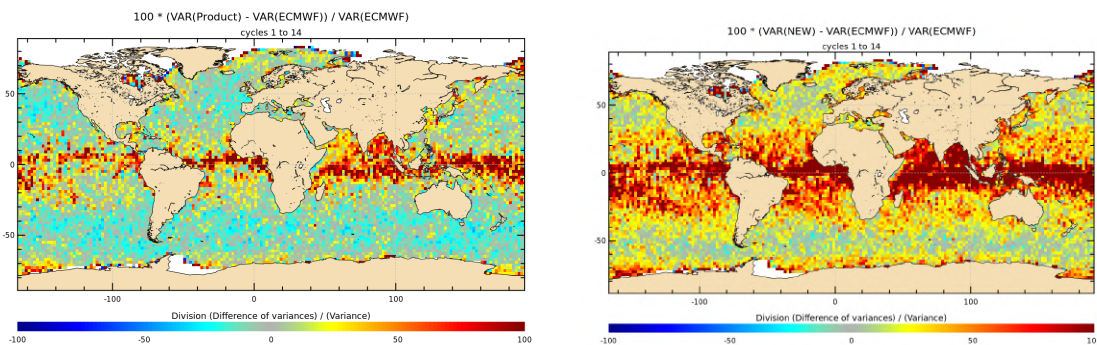


Figure 5-13 Wind speed variance comparison: relative difference between SWIM wind speed variance and ECMWF wind speed variance. Left: Current SWIM wind speed retrieval algorithm; Right: results for SWIM wind speed obtained with a preliminary version of the Look Up Table. This analysis was obtained by accumulating 6 months of data (November 2018 to April 2019)

This wind speed inversion model needs to be finely tuned with the processing of 1-year nadir data. This solution will also be validated by comparison with independent data such as in-situ, altimeters and SCAT data. In a second time, the possibility to extend the Wind Speed retrieval range (above 30m/s) will also be analyzed to add observation capabilities.

### 5.3.6 NADIR RAIN FLAG

As explained before, the rain/bloom flag processing needed to be adapted to the SWIM mission. A first tuning of this processing has been performed and is applied in the products. As shown in Figure 5-14,

the consistency between rain event given by the flag and corresponding rainfall rate from radiometers for collocated data allows to say that the rain flag is usable for rain events. Concerning bloom events (Figure 5-15), some drooling effects are observed near coasts, the cause of these effects is identified, and processing improvement is under specification to reduce them, however at this stage, bloom event given by the rain flag cannot be used.

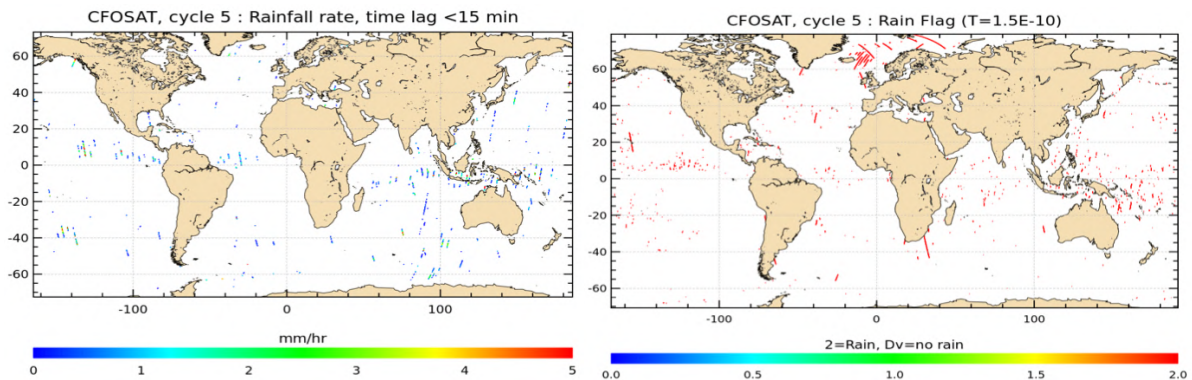


Figure 5-14 : Rain event identification for CFOSAT cycle 5- Left: Radiometer rainfall rate for collocated point with a time lag less than 15min ; Right: rain event identified by SWIM nadir rain flag (value = 2)

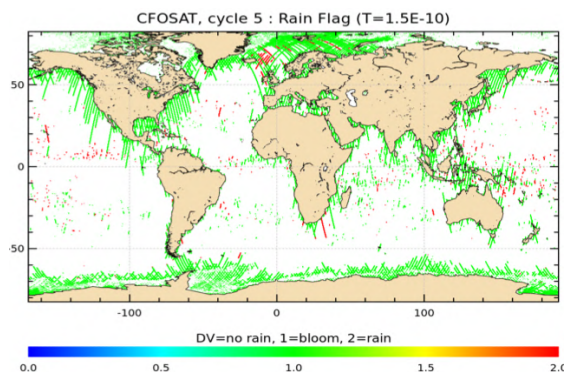


Figure 5-15 : Bloom event identification for CFOSAT cycle 5, identified by SWIM nadir rain flag (value =1)

### 5.3.7 MEAN SQUARE SLOPE PARAMETER

As already described, the adaptive retracking gives access to the mean square slope (mss) of the ocean surface, parameter that is not given in the conventional altimetry products. A first analysis has been performed on this variable, and preliminary results (Figure 5-16) show a rather noisy signal on ocean, but signatures on sea-ice are very encouraging (Figure 5-16 right). This variable will be further analyzed to be better understood and used.

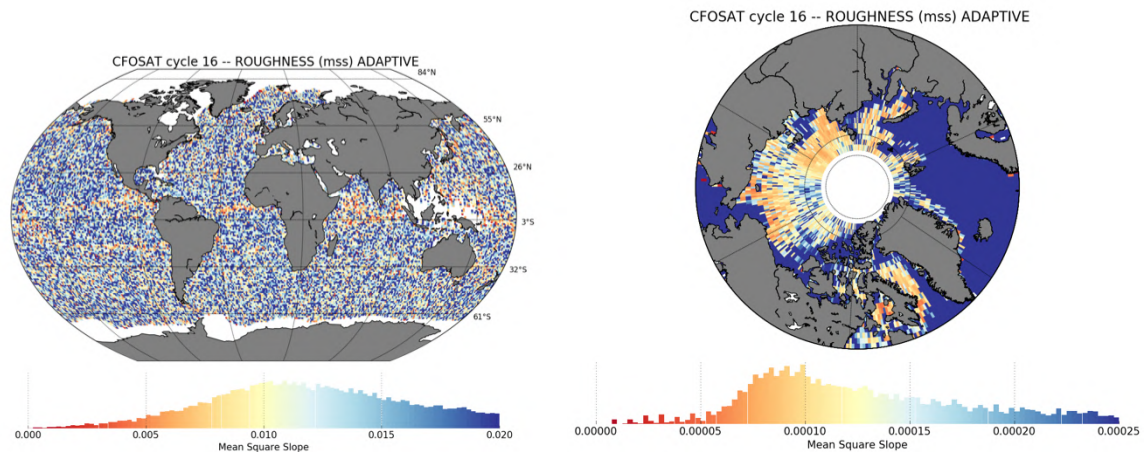


Figure 5-16 SWIM Mean Square Slope cartography for CFOSAT cycle 16; Left : over ocean; Right over Arctic sea-ice.

#### 5.4 FORESEEN ANALYSES AND EVOLUTIONS

- $\sigma^0$  values from the nadir beam over the ocean will be qualified with more details in the next months:
  - Completing cross-over points analyses
  - Using transponder data (some of them already acquired but not yet analyzed)
  - Comparison of  $\sigma_0$  values obtained from the retracking algorithm to those obtained through the L1a data processing applied to all SWIM beams will be carried out.
  
- The first tuning of rain flag will be further validated, and improvement of bloom event detection will be specified.
  
- The mean square slopes provided by the adaptive retracking algorithm will be further analyzed to be better understood and to assess its potential use.
  
- Analysis of the retracking parameters from ICE1 and ICE2 algorithm needs also to be done
  
- Possible evolutions:
  - The new method for wind speed estimation based on a Look Up Table will be further analyzed. The Look Up Table will be updated. The implementation in the nadir processing will be envisaged for a new processing issue.

**Reference :** CF-SYMI-NT-3572-CNES

**Issue :** 1.0

**Date :** 2019\_09\_11

## 6 - SIGMA0 PRODUCTS (L1A\_CWWIC, L2\_CWWIC)

### 6.1 VARIABLES ANALYZED AND STEPS FOR THE VERIFICATION

The normalized radar cross-section is provided for all the SWIM beams from 0° to 10° and for all scenes (ocean, continent) as far as the nadir tracking has been successfully achieved with the on-board processing.

At Level 1A,  $\sigma_0$  are provided at the range resolution, in the geometry of the downloaded data, and following the temporal sequence of the macrocycle of SWIM acquisition (in the nominal mode, scanning successively the 0°, 2°, 6; 8, and 10° incidence beams). Each range bin is associated to latitude and longitude coordinates.

The number of bins retained in the L1A product is recalled in Table 3 here below for each SWIM beam.

At Level 2 in the CWWIC products,  $\sigma_0$  have been averaged per bins of 0.5° in incidence and 15° in azimuth, and referenced in the geometry of the wave cells (called boxes): one box every 70 km (approximately) on each side of the nadir track.

For the conversion of radar echo to  $\sigma_0$  applied in the Level1A processing, the classical radar equation is considered; it includes geometrical and radiometric corrections (see the PUG, [R2]). In order to assess the  $\sigma^0$  values, all steps of the raw signal corrections have been checked.

For the geometrical corrections, the altitude of the satellite is provided by the epoch of the nadir beam of the same macrocycle. No specific problem was identified at this stage.

SWIM beam	0°	2°	4°	6°	8°	10°
Number of range bins in the footprint	256	755	933	2772	2640	3216
Range binning after on-board processing (m)	0.3747	1.4989	1.4989	0.7494	1.1242	1.1242
Corresponding ratio (in dB) with respect to the antenna gain at the maximum in the footprint	-0,90	-15,33	-4,90	-4,25	-4,39	-3,80
Number of range bins within the 3dB antenna gain footprint (considered as reliable in terms of antenna gain pattern)	256	393	744	2342	2190	2860

Table 3: Binning characteristics for each SWIM incidence beam in L1A products

For the radiometric corrections (instrument gain and losses), the calibration coefficients from the most recent on-board calibration sequence are taken into account. No specific problem was encountered.

The antenna gain pattern correction is taken into account both in elevation and as integrated values over the azimuth footprint. This requires an accurate evaluation of mispointing angles because any error in mispointing impacts the antenna gain pattern correction. Validation of mispointing angles is presented in section below.

In addition, specific analyses have been done during the verification phase on the antenna gain corrections because we found that the  $\sigma_0$  profiles with incidence exhibited unexpected trend with incidence in some azimuthal directions (see section 6.3.1.2).

Finally, at level 1A,  $\sigma_0$  values are corrected from the thermal noise by subtracting the mean value of the thermal noise.

Note that no atmospheric correction is applied at Level 1A. In opposite, Level 2 includes such a correction to account for attenuation by the dry and wet atmosphere (water vapor and liquid cloud water taken in auxiliary files generated from ECWMF model short term forecasts).

Finally note that in the Level 2 processing there is a possibility to include corrections to account for biases between the different SWIM incidence beams. This has not been activated until now.

## **6.2 VALIDATION METHOD AND DATA SET USED FOR ANALYSIS**

Most of the efforts until now have been concentrated on data over the ocean. The consistency of the data has been evaluated by comparing the results for the different SWIM beams (0 to 10°) and by comparing to the external reference of  $\sigma_0$  values provided by GPM (empirical model representing the GPM data sets). This was carried out by analyzing on one hand the mean values and standard deviation of  $\sigma_0$ , either at the scale of the L1A data (variation within the footprint) or by averaging these data around each beam center and analyzing the variations with wind speed, significant wave height, azimuth, ...etc. Consistency of the results between the six SWIM incidence beams has also been analyzed.

Different data sets were used: either limited data sets for case studies (in particular to investigate rain effects) or global analyses on 1 or several orbits.

Some studies using the rain forest or desert areas have been tentatively developed but they are not conclusive until now, probably because of large homogeneities of the areas chosen for these studies or to the fact that the topography has not been taken into account in this product (all the data are presently referenced to the geoid WSG84). So they are not reported here.

## **6.3 MAIN RESULTS**

### **6.3.1 ANTENNA GAIN COMPENSATION**

#### **6.3.1.1 MISPOINTING ANGLES**

In order to apply the antenna gain correction we need to account for the instrument pointing. For that purpose, an algorithm has been implemented in the L1a processing to estimate the mispointing angles in the roll and pitch directions at the rate of macrocycles sequences (for ocean scenes only). The

algorithm is based on the minimization of a cost function. For each macrocycle and each beam of the macrocycle (thus for a given azimuth angle), the cost function computes the distance between:

- a theoretical echo corrected for geometrical considerations, thermal noise and instrumental gain contributions (ie a model of  $\sigma_0$  dependence with incidence which includes antenna gain contributions);
- and the measured echo at a given beam  $k$  and antenna azimuth angle  $\phi$

The modeled  $\sigma_0$  used to define the theoretical echo is based on the optical geometrical backscattering theory and assumes homogeneous and isotropic mean square slopes at the surface. After simplifying assumptions, the modeled  $\sigma_0$  is represented by a 2<sup>nd</sup> degree polynomial in elevation angle, with three coefficients A, B and C depending on mean square slopes. A theoretical analysis has been performed before launch to validate such a model compared with a “full shape” model.

The integrated antenna gain contribution applied to the modeled  $\sigma_0$  is defined by a 2<sup>nd</sup> degree polynomial surface in roll and pitch mispointing angles ( $\alpha_r$  and  $\alpha_t$ ). Coefficients of the polynomial surface were pre-calculated using the measured antenna gain, for each beam from 0° to 10°, each bin of antenna azimuth angle and each bin of elevation angle. In the L1A-processing mispointing algorithm, values of these coefficients are interpolated at the actual antenna azimuth and elevation angle.

Thus, the state parameters of the cost function are:

- the coefficients A, B and C used to define the modeled  $\sigma_0$
- the roll and pitch mispointing angles  $\alpha_r$  and  $\alpha_t$  which define the antenna gain contribution to the modeled  $\sigma_0$ .

Estimated roll and pitch mispointing angles are obtained as the optimal values of  $\alpha_r$  and  $\alpha_t$ .

In order to validate this algorithm with real data, the output of the mispointing estimation implemented as described above was compared to two other estimations:

- the mispointing angles estimated from cross-maneuver operations (name the “cross-maneuver method”, hereafter),
- the difference between theoretical and measured platform pointing angles (this difference corresponds to the mispointing angles at the first order); this method is named the “pointing difference method” hereafter.

These comparisons have revealed that:

- all methods converge to estimated roll and pitch mispointing angles within the accuracy requirements (0.4° on absolute pointing angle estimation and 0.2° on mispointing knowledge)
- the L1A-estimated mispointing angles are consistent with the pointing difference method, in the mean values (mean total mispointing ~ 0.02°)
- the retrieved pointing variations are consistent with both the reference ellipsoid variations at the orbital scale (Figure 6-1) and with the impact of the antenna rotation (see Figure 6-2).
- the L1A-estimated mispointing angles are provided with an accuracy of about 0.01° (compliant with the expected accuracy of the algorithm).
- the L1A-processing mispointing algorithm seems to be much more reliable than the cross-maneuver method because by definition, the cross-maneuver method cannot describe any temporal variation of the mispointing (like effect of antenna rotation or ellipsoid contributions). Only a value can be retrieved in pitch and roll after one cross-maneuver sequence.

Once the mispointing angles are estimated, they are used to correct  $\sigma_0$  measurements from antenna gain contributions.

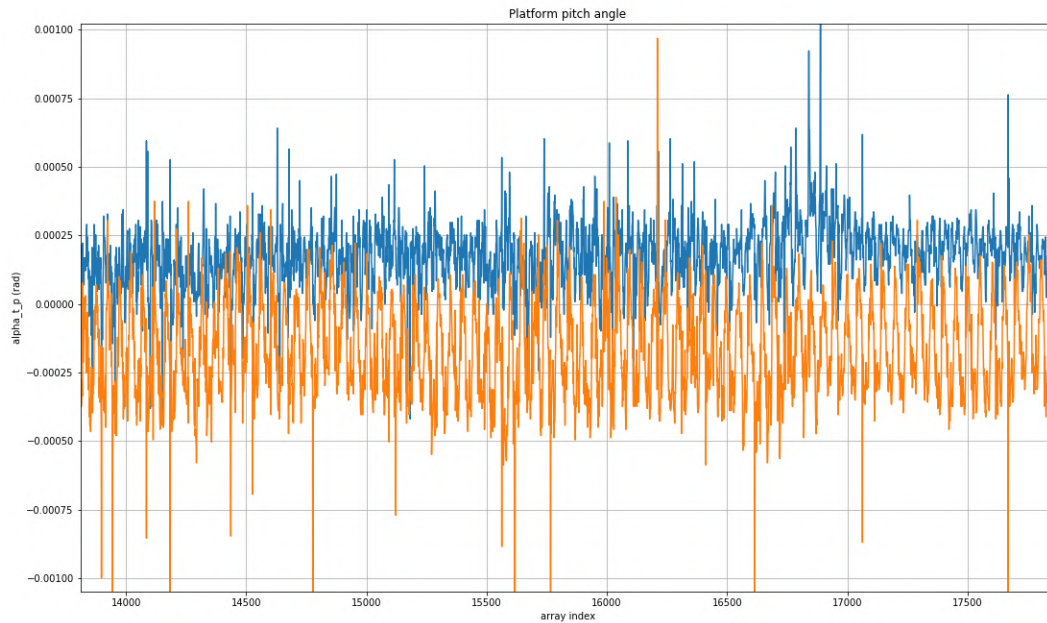


Figure 6-1 : Roll (blue curve) and pitch (orange curve) mispointing angles estimated from the LIA-processing algorithm, for more than 4000 consecutive measurements (about 880s) over ocean. Large-scale oscillations in the pitch mispointing angles highlight the reference ellipsoid impact on total pointing variations. Shorter scale oscillations are due to antenna rotation (see Fig below).

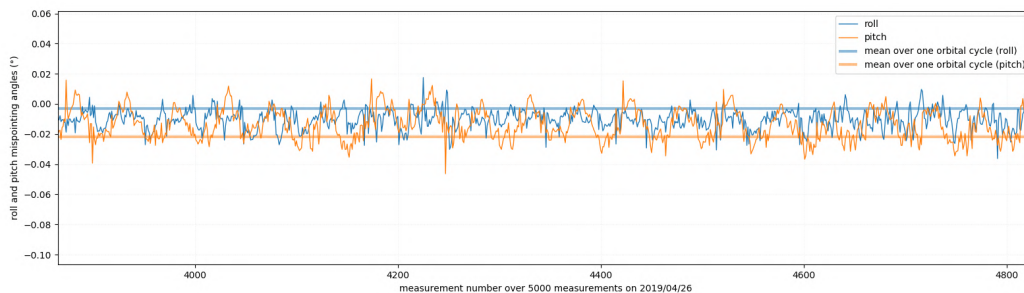


Figure 6-2 : Roll (blue curve) and pitch (orange curve) mispointing angles estimated from the LIA-processing algorithm, for 1000 consecutive measurements over ocean (about 220s), on 2019/04/26. Thick lines represent mean oceanic roll (blue) and pitch (orange) mispointing angles averaged over 13 days of data. Oscillations in the pitch mispointing angles highlight the antenna rotation impact on mispointing variations.

### 6.3.1.2 ANTENNA BEAM PATTERN CORRECTIONS

In the processing, the antenna gain correction (integrated over each gate) is applied by using a pre-calculated look-up table which includes the integrated antenna gain over the direction perpendicular to the look direction, for each beam and each corresponding elevation bin in the swaths, and every 5° of antenna azimuth angles between 0° and 360°. In the LIA processing, values from the pre-calculated integrated antenna gain are interpolated at the position of the measured azimuth and of each elevation angle of the swaths.

Until mid-July, the integrated antenna gain was computed from the 2D antenna gain measured in anechoic chambers during SWIM Assembly and Integration Tests (AIT) on the satellite. It was measured

in 8 look directions (every 45° of antenna azimuth angles) and interpolated to intermediate azimuths angles for the L1a processing.

One of the result of the CAL/VAL analysis is that we observe an azimuthal dependence of  $\sigma_0$  trend with respect to incidence, with more convexity of the trend for some looking angles in the right of the satellite track (see Figure 6-3, left-hand side of Figure 6-4 and Figure 6-5). Thus, different tests were carried out on the antenna gain pattern correction. It was verified that this unexpected behavior cannot be due to errors in the prescribed mispointing angles used to estimate the antenna gain pattern (see previous section). It was also verified that this is not due to interpolation errors. Finally, the most conclusive test is the one which combines antenna gain patterns from simulation (on one side of the rotation) with antenna gain patterns measured in anechoic chamber (on the other side of the rotation). They give better results in terms of  $\sigma_0$  trend with incidence compared to the original antenna gain pattern prescribed in the processing (see right-hand side of Figure 6-4). Indeed, they reduce the azimuthal dependency of the  $\sigma_0$  profiles with respect to the satellite track with almost identical convexity for right-hand side and left hand-side looking angles. Statistics of the improvement on  $\sigma_0$  profiles using this combined antenna gain look-up-table was evaluated by analyzing the occurrence of the flag characterizing the convexity of the  $\sigma_0$  trend with incidence compared to  $\sigma_0$  profiles provided by the radar instrument of GPM (same incidence range and same frequency). The results are shown in Table 4 for one day of data. However, the reason of this improvement is not clear enough yet, and the source of the azimuthal dependency of the antenna pattern correction is currently under investigation (see section 6.4 for more details on further improvements).

After these different tests, it was decided that starting mid-July with CWWIC product generation in version 4.3.1, the pre-calculated integrated antenna gain will combine the measured antenna pattern (mentioned above) for several consecutive look directions (on one side of the rotation) and simulated antenna pattern for another range of look directions.

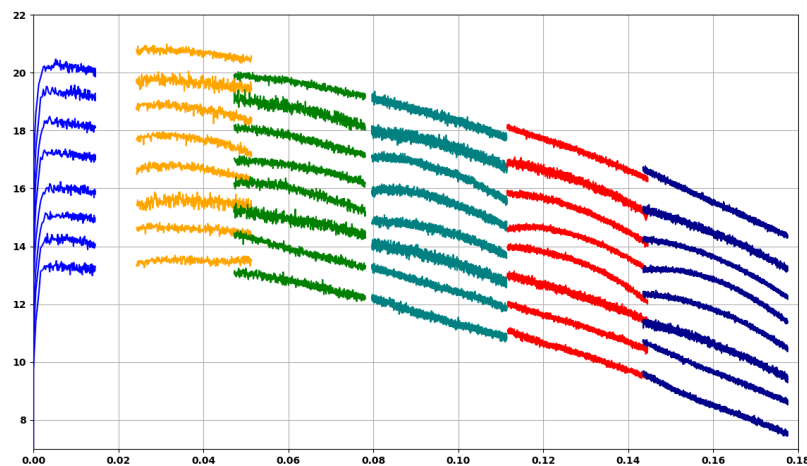


Figure 6-3 :  $\sigma_0$  profiles as a function of the elevation (in rad) for the different beams (beams 0° to 10° in different colors) and for 8 successive azimuths directions (with a shift in vertical axis to ease the presentation)

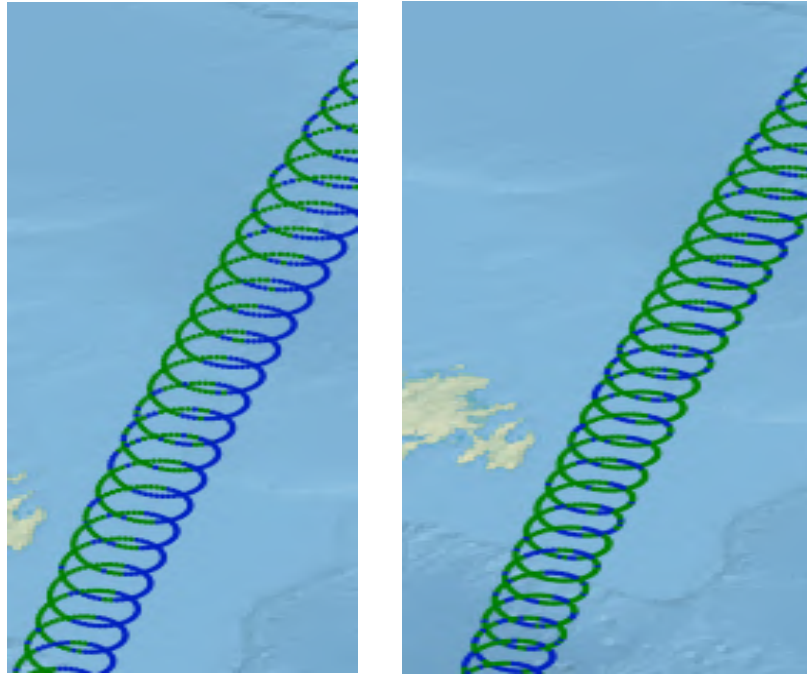


Figure 6-4: Flag of convexity or concavity of the shape of  $\sigma_0$  with respect to the angle of incidence. Here zoom-in on an orbit for the 8 ° beam. The blue color indicates the samples for which the flag is raised (convexity stronger than that expected from the GPM data). This diagnosis is systematic on all the orbits for all the beams analyzed with this flag (6, 8 and 10 °). Left plot: with the present antenna lobe pattern correction. Right-hand side plot: with an alternative antenna lobe pattern correction which combines laboratory measurements and simulation of the antenna pattern.

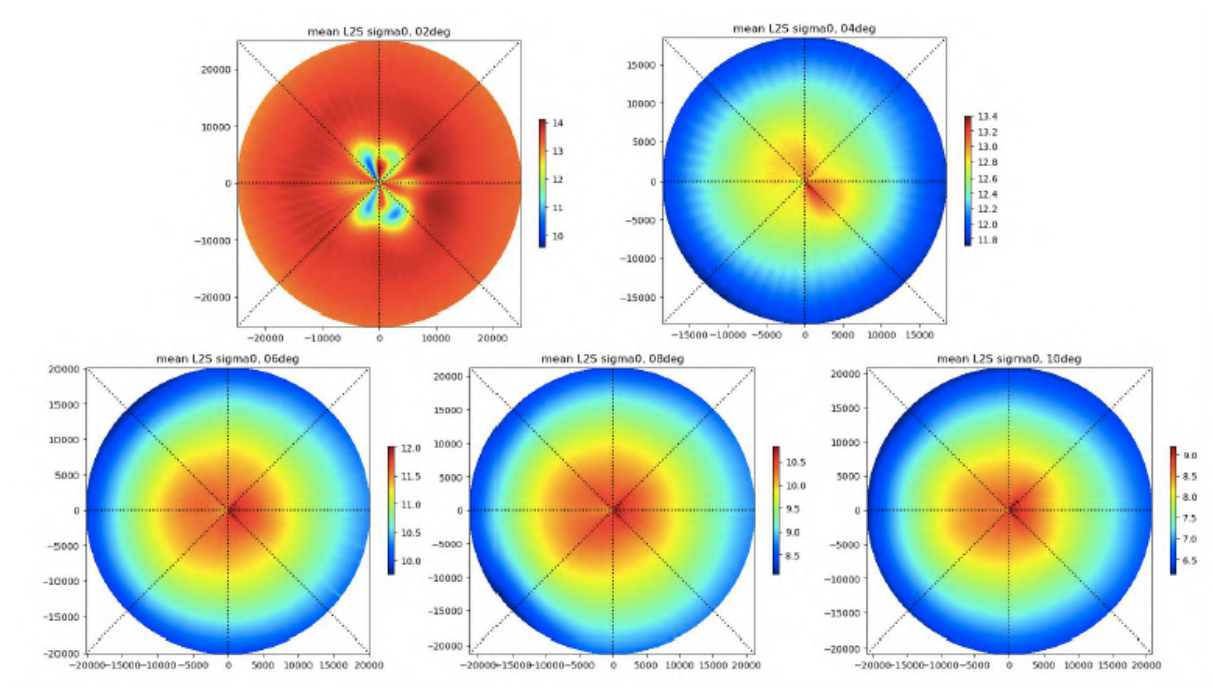


Figure 6-5: Polar plots representing mean values for  $\sigma_0$  as a function of range (in meters) in each azimuth direction (with respect to satellite track). 43 days of data have been averaged (before April 25<sup>th</sup> 2019). The color code represents the  $\sigma_0$  value (in dB). From top left to bottom right: for SWIM beams 2, 4, 6, 8, and 10°

Value of flag on shape of $\sigma_0$ profile	TYPE OF L1B PRODUCTS	Beam 6°	Beam 8°	Beam 10°
=0 (nominal profile)	OPERATIONAL PRODUCTS*	31%	39%	30%
	TEST PRODUCTS**	46%	70%	48%
=1 (concave profile)	OPERATIONAL PRODUCTS	67%	58%	66%
	TEST PRODUCTS	52%	36%	48%

\*OPERATIONAL PRODUCTS (use of measured antenna gain to perform the antenna gain correction in the L1A processing)  
 \*\*TEST PRODUCTS (use of combined measured/simulated antenna gain to perform the antenna gain correction in the L1A processing)

Table 4 : Proportion of measurements with the flag on concavity of the shape of  $\sigma_0$  profiles equal to 0 or to 1, either using the measured antenna gain or using the combined measured/simulated gain for the antenna gain correction. Statistics are computed over one cycle of data (13 days).

### 6.3.2 THERMAL NOISE CORRECTIONS AND SIGNAL TO NOISE RATIO

Thermal noise is estimated from the noise floor of echoes. Starting with version 4.3.0 of the processing, the 2° beam is used instead at the 0° beam as the reference beam to provide this noise floor. This was chosen in order to better estimate the thermal noise mean level (at 0° the noise floor is not reached because a signal to noise ratio greater than anticipated, see section 3 - ). Note also that starting with version 4.3.1,  $\sigma^0$  values are provided in linear scale, keeping eventual negative values when the signal is below the mean thermal noise.

Figure 6-6 illustrates the performance in terms of mean signal to noise ratio. It shows a very large signal to noise ratio at the central incidence for all beams (12 to 18 dB). At the near and far ranges, the mean SNR remains larger than about 5 dB for beams 6 and 8° but decreases to about 3 dB for beam 10°.

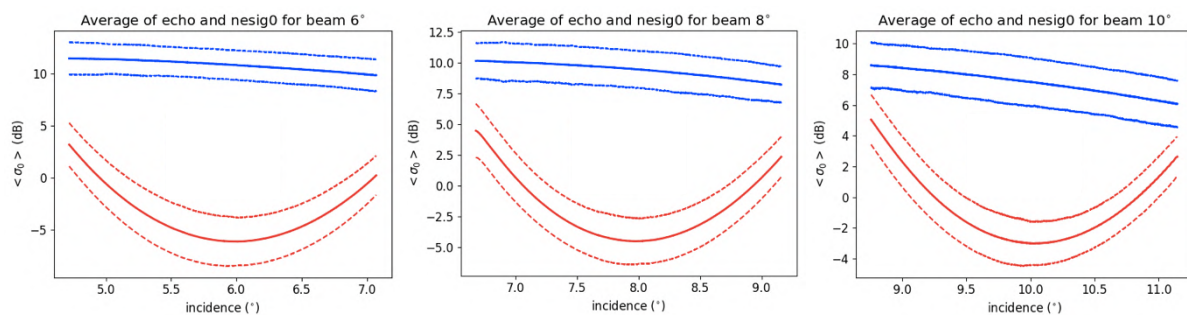


Figure 6-6 : Mean and standard deviation of  $\sigma_0$  for beams 6, 8, and 10° over the ocean (blue lines), compared to the noise equivalent ratio (red lines)

### 6.3.3 SIGMA0 ANALYSIS

Unless stated, all the results shown in this section are based on the antenna gain correction as prescribed before July 2019; this means that the antenna gain integrated over the azimuth footprint was computed from the 2D antenna gain measured in anechoic chambers during SWIM Assembly and Integration Tests (AIT), see section 6.3.

Figure 6-7 and Figure 6-8 plotted from L1a products illustrate that:

- $\sigma_0$  values exhibit a very good dynamic over the incidence range from 0 to 11° (in consistency with good signal to noise ratio).

- Except for the convexity of the  $\sigma_0$  trend with incidence already discussed above,  $\sigma_0$  of each SWIM beam exhibit overall consistent values with respect to GPM values. At some incidences there might be some bias (of the order of 1 dB) but this still needs to be confirmed.
- The standard deviation of the  $\sigma_0$  pdf (Figure 6-8) is smaller for SWIM than for GPM and this seems consistent with the fact that the noise is smaller on SWIM.

Figure 6-9 illustrate the results for mean profiles of  $\sigma_0$  with incidence estimated from L2 products and compared to GPM results. It shows that SWIM profiles are in overall agreement with results from GPM both over ocean and over sea ice, in spite of a small overestimate of SWIM with respect to GPM at the largest incidences of SWIM. Figure 6-9 also shows however that the 2° beams departs from all the other measurements both in mean level and in shape. It was already apparent on the polar plots shown in Figure 6-5. This needs to be further investigated.

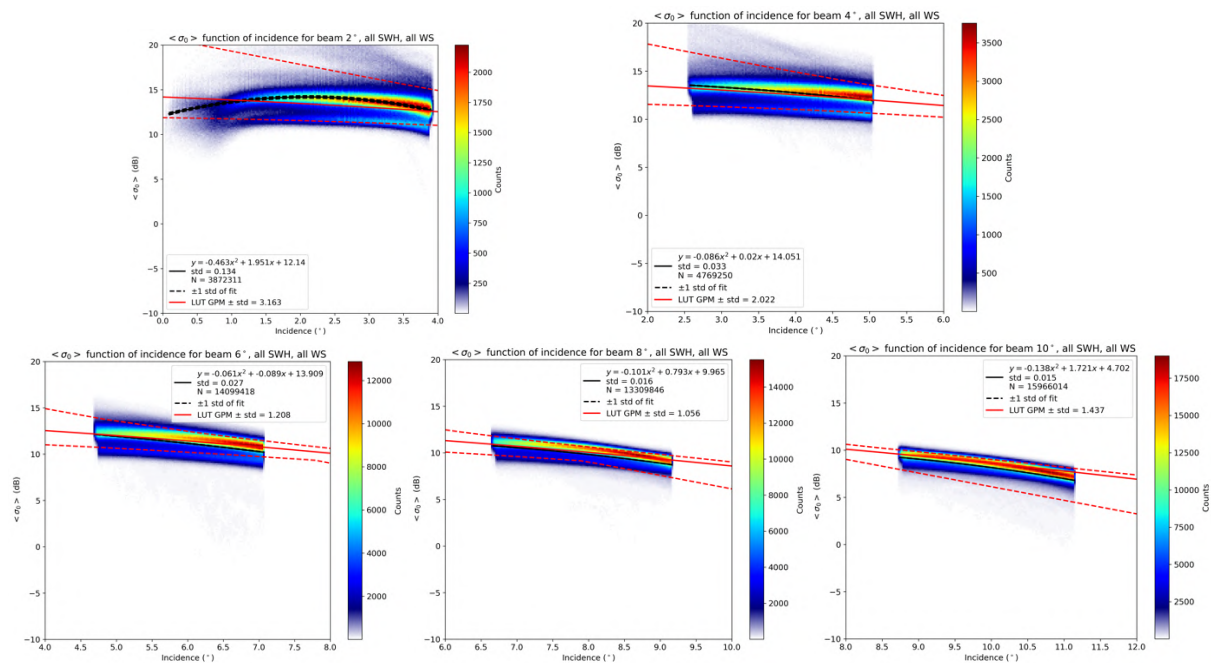


Figure 6-7 :  $\sigma_0$  values from L1a product (version 4.3.0) over the ocean (cumulated over 24 hours on 25-26 April 2018 for beams 2°, 4° (top), 6°, 8° and 10° (bottom)). The color codes denote the number of points, the red solid and dashed lines refer to GPM reference look-up table (mean and standard deviation of the GPM values for the same range of wind and waves). The black line is a fit on the data

Note that at this stage, possible inter-beam biases have not been corrected. By comparing the mean profiles of  $\sigma_0$  with incidence from the different beams over oceanic scenes, we could give a rough estimate of the inter-beam bias, found to be of the order of 0.5 to 0.8 dB. However, this analysis may be hampered by the problems of convexity evidenced in the near and far range of each footprint (due to the too large convexity). Therefore, we need new data sets with better corrections of antenna gain pattern to confirm these inter-beam biases.

In spite of the small anomalies above mentioned (some convexity in the profiles in particular on one side of the antenna rotation, abnormal behavior of the 2° beam and possible slight interbeam biases), the  $\sigma_0$  values taken at the center of each beam could be analyzed with respect to wind and wave conditions. Figure 6-10 illustrates the overall good consistency of this trend, in particular as compared

to what we know from the GPM data sets. The sensitivity to wind speed is very small for the 10° and 8° beams (1dB to 1.5 dB difference between 5 and 20 m/s) and gradually increases at smaller incidence angles. Thanks to this smallest sensitivity of  $\sigma_0$  with wind speed at 8 and 10°, the dominant effect in the  $\sigma_0$  fluctuations at the scale of the footprint will hence be the tilt of the long waves, so that the best results for the wave inversion are expected to come from these incidence ranges. Figure 6-10 also shows that at light winds (typically less than 4 to 5 m/s, there are many outliers. This is probably due to the fact that in this analysis there is no rain scene or non-homogeneous scene elimination.

Maps of mean and standard deviation of  $\sigma_0$  over the ocean are illustrated in Figure 6-11. In addition to a different sensitivity to wind speed at the different incidences, already illustrated in Figure 6-10, they show the probable effect of rain, especially in the tropical regions, both on mean and standard deviation values. This illustrates the need to work on a rain flag in addition to the one which will be provided by the nadir beam according to the method applied on AltiKa data. First analysis show that a flag based on  $\sigma_0$  variance (after filtering wave effects) may be sufficient. The very first results are illustrated in Figure 6-12. Work is under progress to better define such a flag for each SWIM beam and eventually implement it in future versions of the processing and products.

CFOSAT SWIM L1A over ocean (abs(lat<55°))  
2019-04-25 00:00:00 to 2019-07-16 00:00:00 nb orbit = 1239

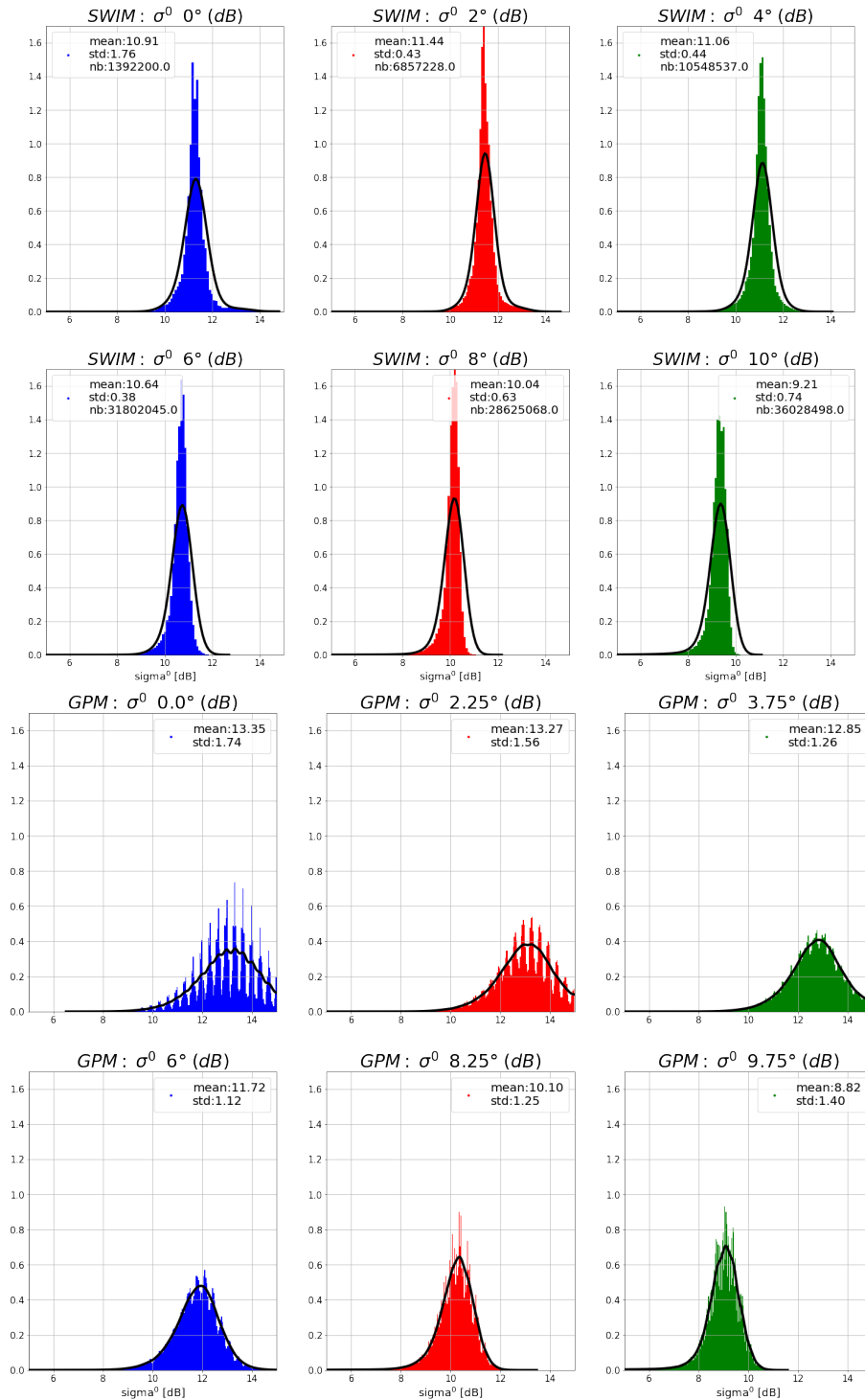


Figure 6-8 : Pdf of  $\sigma_0$  values over the ocean (without sea ice) from L1 SWIM products (top 2 rows) compared to GPM (bottom 2 rows) for a period of 2,5 months. In these distributions, SWIM  $\sigma_0$  are taken at an incidence close to the beam center  $\pm 0.5^\circ$  (center value indicated on the top of the plots), except for near nadir, taken for SWIM at  $0.6^\circ \pm 0.25^\circ$ .

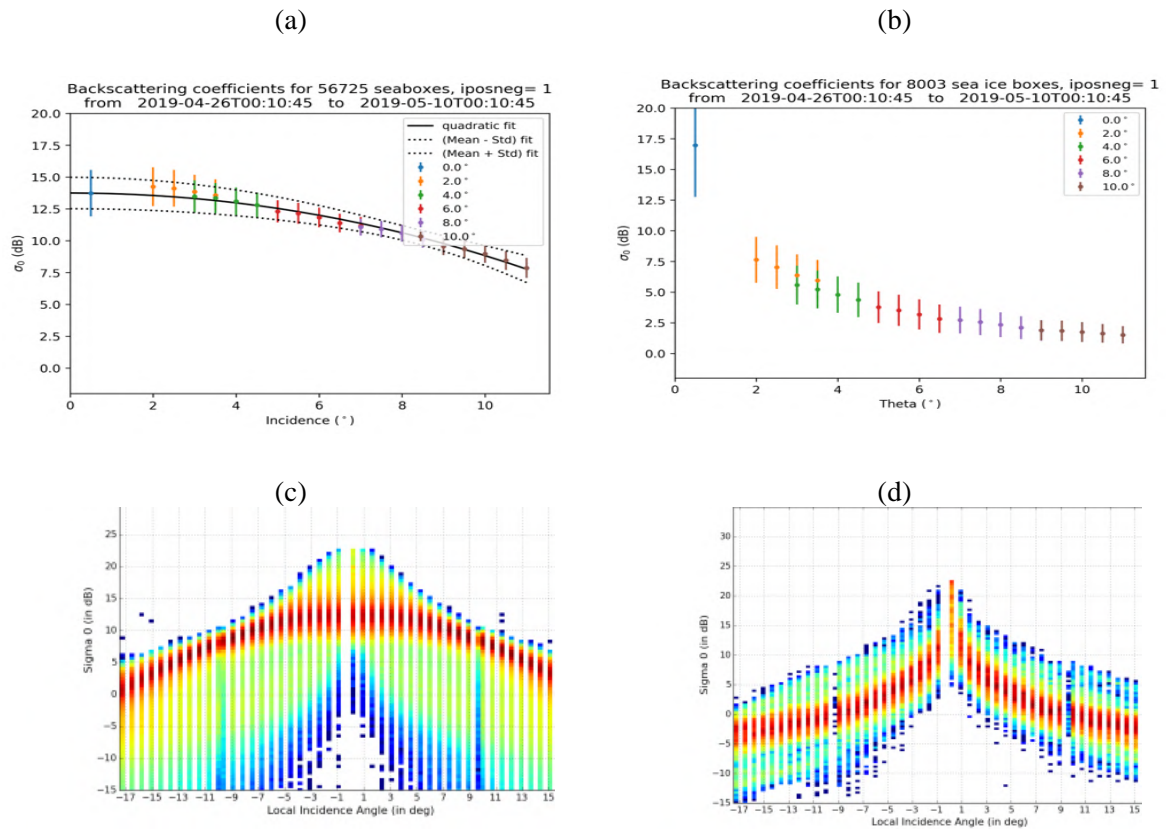


Figure 6-9 : Mean profiles over 15 days of  $\sigma_0$  versus incidence from SWIM for ocean scenes (a) and sea ice scenes (b), estimated from L2 products in version 4.3.0. (c, d) profiles from GPM (with symmetry around nadir and shown as histograms)

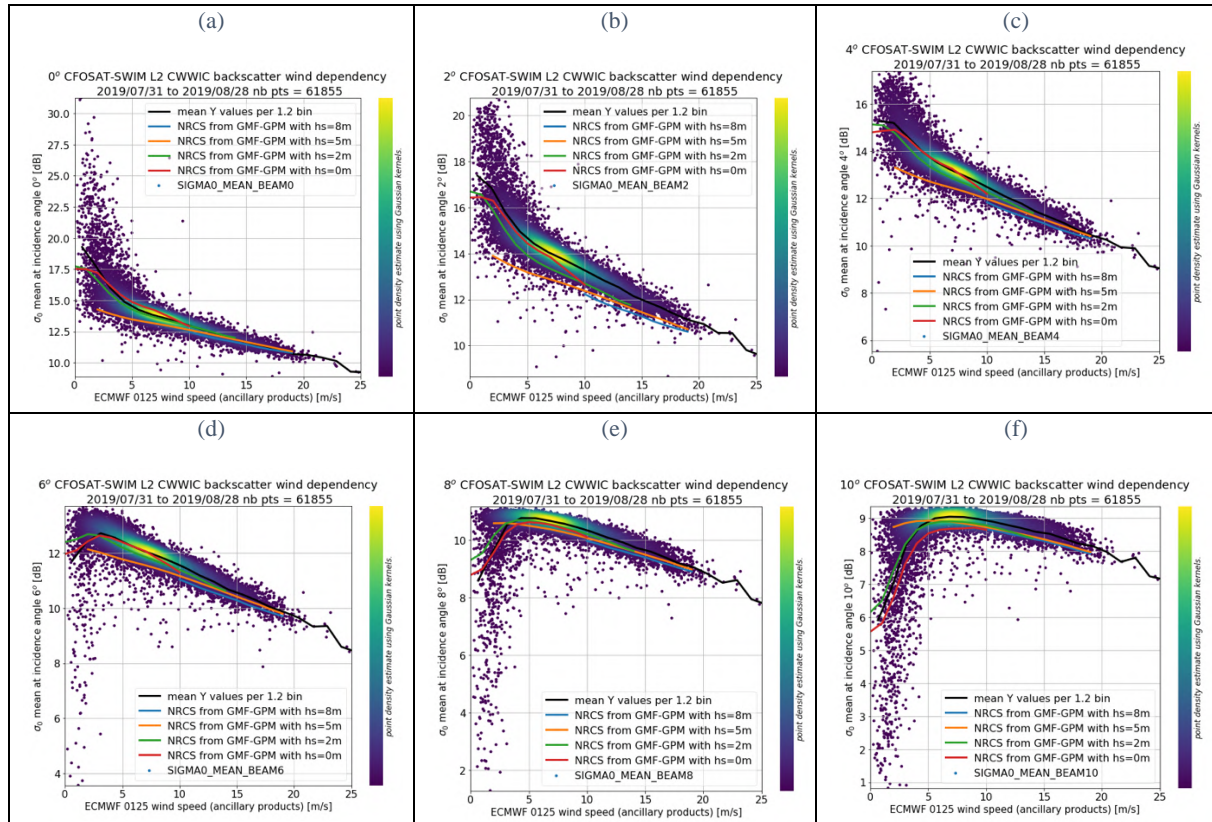
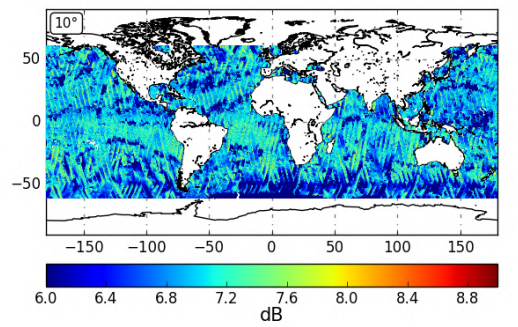
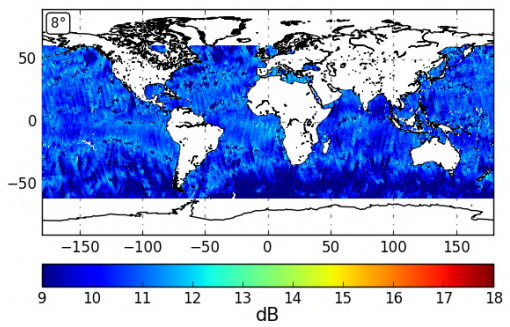
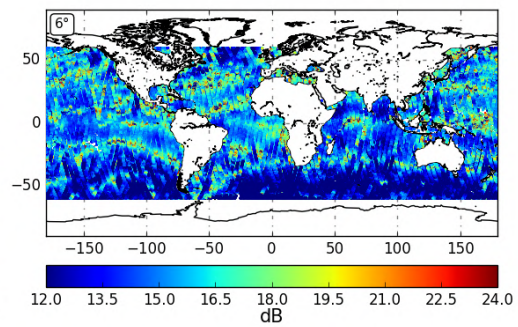
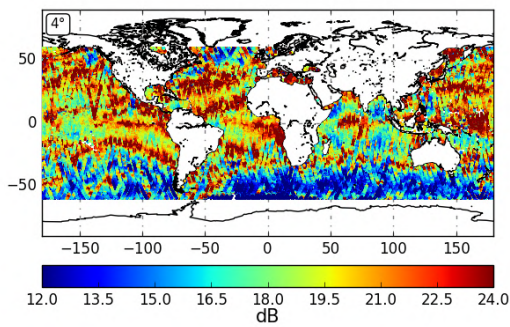
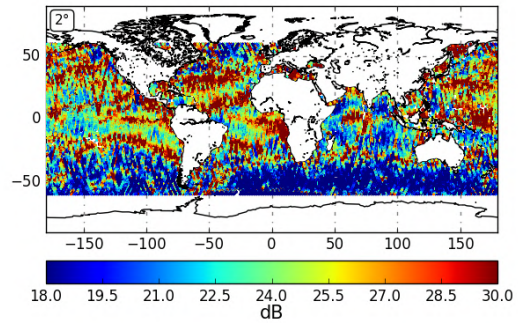


Figure 6-10 : Distribution of  $\sigma_0$  values for incidence values around  $0^\circ$  (a),  $2^\circ$  (b),  $4^\circ$  (c),  $6^\circ$  (d),  $8^\circ$  (e) and  $10^\circ$  (f) at  $(\pm 0.5^\circ)$  as a function of wind speed (taken from the ECMWF model).

Map of Mean Sigma0 10% middle range



Map of Standard Deviation  $\sigma_0$  10% middle range

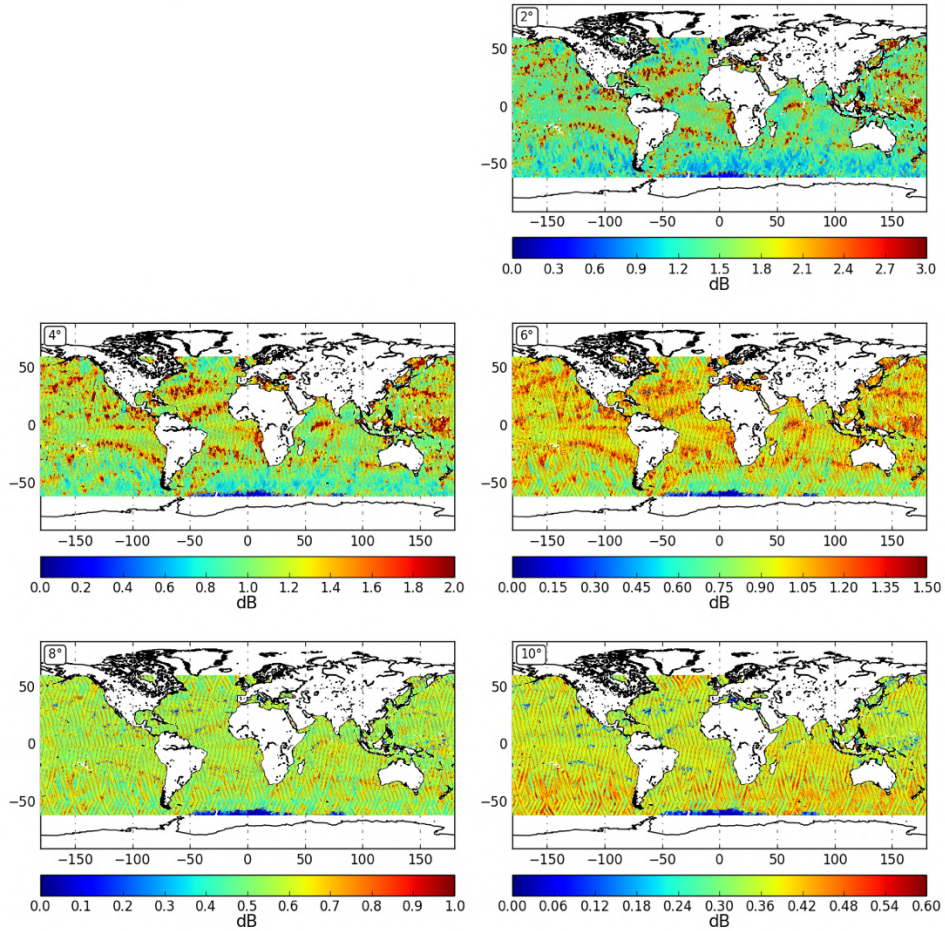


Figure 6-11: Maps of mean  $\sigma_0$  and its standard deviation for each beam center (2 to 10° beams) from LIA products of CFOSAT orbital cycle #4. Data plotted over the ocean for  $abs(latitude) < 50^\circ$  and distance to the coast  $> 100$  km.

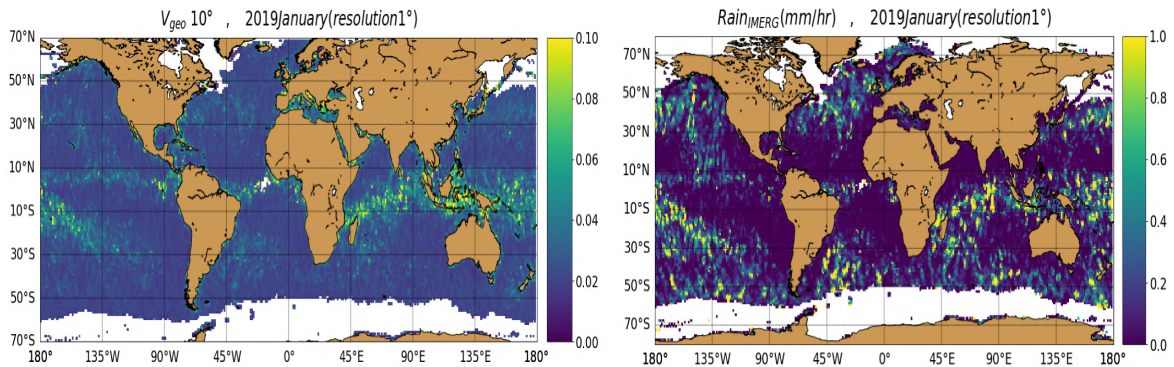


Figure 6-12 :Left: Indicator on  $\sigma_0$  variance (for beam 10°) compared to a rain map from IMERG (right).

## 6.4 FORESEEN ANALYSES AND EVOLUTIONS

### 6.4.1 PLANNED PROCESSING EVOLUTIONS

As explained in section 6.3, further investigations are needed to improve the antenna gain correction of the  $\sigma_0$  profiles. Thus, an update of the antenna gain correction will be done as soon as more data are available to estimate it from ocean scenes. Starting with CWWIC production version 4.3.2, the correction relies on combined 2D antenna pattern measurements (performed before the launch in an anechoic chamber, every 45° in azimuth for each beam) and RF simulations, and interpolated for all azimuth directions. In future versions, it is likely that we will use an empirical antenna gain pattern, integrated over all antenna azimuth angles. It will be estimated by averaging over a sufficiently long time period, echo measurements before instrumental correction is applied. Thus, this will be done when enough data will be available to estimate such an empirical correction.

### 6.4.2 FORESEEN ANALYSES

Concerning the mispointing estimation, which affects the estimation of  $\sigma_0$  through the antenna gain correction, we will continue to use the method implemented in the L1A processor and monitor its evolution with time.

We will also continue the analysis of  $\sigma_0$  values and their dependence with incidence, azimuth, surface parameters (wind, waves, sea ice), presence of rain, in order to validate more precisely the data. In particular:

- Behavior of the  $\sigma_0$  profiles from the 2° beam needs to be investigated in more details.
- More precise evaluation of possible inter-beam biases will be carried out
- Comparisons will be carried out on  $\sigma_0$  estimated from the retracking algorithm and from the Level1a  $\sigma_0$  estimates.
- Preliminary analysis on the  $\sigma_0$  angular dependence with respect to the wind direction indicates that it should be possible to estimate the wind direction at a scale of about 140 km to 200 km (two rotations of the antenna). This possibility will be investigated in more details before proposing to add this parameter (wind direction) in the Level 2 product.
- Comparisons with independent data sets (like GPM) will be enriched to estimate possible bias
- Analysis of  $\sigma_0$  on sea ice, and continental surfaces must be carried out in details. Statistical properties of  $\sigma_0$  in sea ice regions should help to define a flag on the presence of sea ice using SWIM data
- Impact of rain on  $\sigma_0$  (mean values, standard deviations) will be investigated in more details for all SWIM beams. Preliminary analyses indicate that the standard deviation of  $\sigma_0$  with respect to its detrended value at a scale of more than 500m is a good indicator of the presence of rain. A comparison with the rain flag provided by the nadir data should be carried out.

## **7 - L1B PRODUCTS (L1B CWWIC AND IWWOC ANALYSIS)**

### **7.1 VARIABLES ANALYZED**

The L1B products provided by the CWWIC mission center includes horizontal fluctuations of  $\sigma^0$  within each footprint and their spectra calculated for the 6, 8, 10° SWIM beam after subtracting the mean dependence with incidence angle to the  $\sigma^0$  values (detrrending operation). These products also include « modulation spectra » which are fluctuation spectra corrected from the speckle noise spectrum and from the impulse response function (in the spectral domain). Expert products (not distributed to users) are generated to record different possibilities of speckle correction although only one of them is implemented in the operational processing chain (see the PUG). One of the goals of the CAL/VAL is to examine the different options for speckle correction and to propose the optimal one. During this first step of the CAL/VAL, we analyzed for the 6, 8, 10° SWIM beams fluctuations of  $\sigma_0$ , their density spectra, estimate of speckle spectra, and modulation spectra.

Concerning the IWWOC processing chain, although there is no L1B distributed product, we have also analyzed the  $\sigma_0$  fluctuation spectra as intermediate products. In addition, although it was not initially planned, IWWOC analyzed fluctuation spectra from the 2 and 4° incidence beams of SWIM (see below), in addition to the 6°, 8°, and 10° beams.

At this level the main differences between CWWIC and IWWOC processing is that in CWWIC processing, the fluctuations analysis is performed at the scale of each complete footprints (~20 km footprints) whereas for IWWOC this analysis is done on overlaying sub-footprints (following the Welsh method) and eventually combining these different spectral estimates afterwards (depending on quality controls). At this stage, IWWOC processing does not include speckle nor impulse response function corrections. It is worth noting that IWWOC center decided recently to extend the analysis to the 2 and 4° SWIM beams.

In both cases ahead of the spectral analysis, some indicators are built to check the consistency of the scenes before applying a spectral analysis. During the CAL/VAL phases diagnostics are done on these indicators but they are not used no reject data sets ahead of the spectral analysis. For CWWIC, this includes in particular Indicators on the mean trend of  $\sigma_0$  (slope and curvature) compared to the GPM empirical model, and calculation of mean, variance, skewness and kurtosis of the modulations at the scale of the footprint. Discussion on mean trend of  $\sigma_0$  is not reported here because it was already mentioned in section 6.

### **7.2 VALIDATION METHOD AND DATA SET USED FOR ANALYSIS**

At this level, consistency of the results has been analyzed by looking either at case studies, or at statistics on large data sets, and by comparing to spectral parameters – mainly direction and wavelength- of wave model outputs (WW3 for IWWOC, MF\_WAM for CWWIC products).

### **7.3 MAIN RESULTS**

Directional analysis of the  $\sigma_0$  fluctuations within each footprint (each cycle) and their spectra have been analyzed in several cases and as averaged values over a 43-day period. Based on the results of this analysis, an error in the onboard real time processing of SWIM signals was evidenced and corrected on April the 25<sup>th</sup> leading to the current performances.

One main shortcoming in L1b products still remains, related to a simplification of the speckle noise model presently considered. In particular, close to the along-track direction, the speckle noise increases quite significantly. In section 7.3.1, we characterize this effect. In section we show that in spite of this effect, the correlation between fluctuation spectra and wave spectra is good, and increases for the outer beams (8 and 10°).

It affects the modulation spectra (supposed to be corrected from speckle noise). This is explained in 7.3.1. Section 7.3.2 describes the current  $\sigma^0$  fluctuations spectra performances. Other comments on  $\sigma^0$  fluctuations and speckle noise are given in 7.3.3 and 7.3.4, respectively.

### 7.3.1 ALONG-TRACK PERTURBATION DUE TO SPECKLE NOISE

As illustrated in Fig. [7-1](#), the mean variances of the  $\sigma^0$  fluctuations exhibit an important and systematic peak aligned with the along-track direction. In the Fourier domain (spectrum of fluctuations), this translates to an increase in energy close to the along-track direction as illustrated for a case study in Fig. [7-2](#) and for an average over a large number of spectra in Fig 7.3. This effect is attributed to an increase of speckle noise in the directions where the Doppler bandwidth becomes relatively small (due to the geometry of observations) which causes the number of independent samples to decrease drastically. This effect was anticipated before the satellite launch but its exact magnitude could not be simulated precisely as it depends not only on the Doppler bandwidth but also on the sea state itself.

Our analysis show (Figure 7-4) that the angular sector with respect to the satellite track affected by this loss of independent samples is about  $-15^\circ$  to  $+10^\circ$  for the ascending tracks and  $-10^\circ$  to  $+15^\circ$  for the descending ones (the asymmetry is explained by the Earth rotation effect). There is also a small change with latitude. These results are in qualitative agreement with a simple analytical model of Doppler bandwidth which takes into account the satellite speed, the look geometry and the Earth rotation (which adds some decorrelation to the radar echoes with a decreasing effect with latitude).

In the CWWIC Level1b processing, a subtraction of the density spectrum of speckle is implemented (see the PUG), but up to now this correction is taken as independent of the azimuth look angle. The present results indicate the necessity to introduce an angular dependency of the speckle noise correction. Work is under progress to establish from the data themselves an empirical model to correct for this perturbing effect.

Meanwhile, the Level2 products (spectra of fluctuation converted in wave spectra and resampled in wavenumber and azimuth) will be provided by masking the sectors affected by this noise, in order to avoid an incorrect detection of the dominant waves (see below).

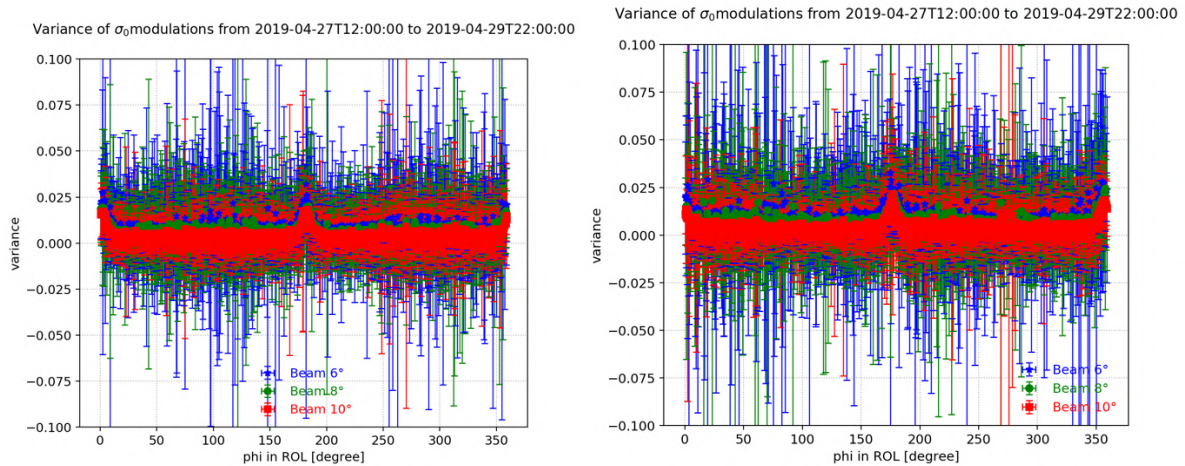


Figure 7-1: Mean Variance of the  $\sigma_0$  fluctuations calculated over each footprint and plotted as a function of the look direction with respect to the satellite track, for descending tracks (left) and ascending tracks (right). This plot was obtained by accumulating data over descending tracks for 1,5 days of observations.

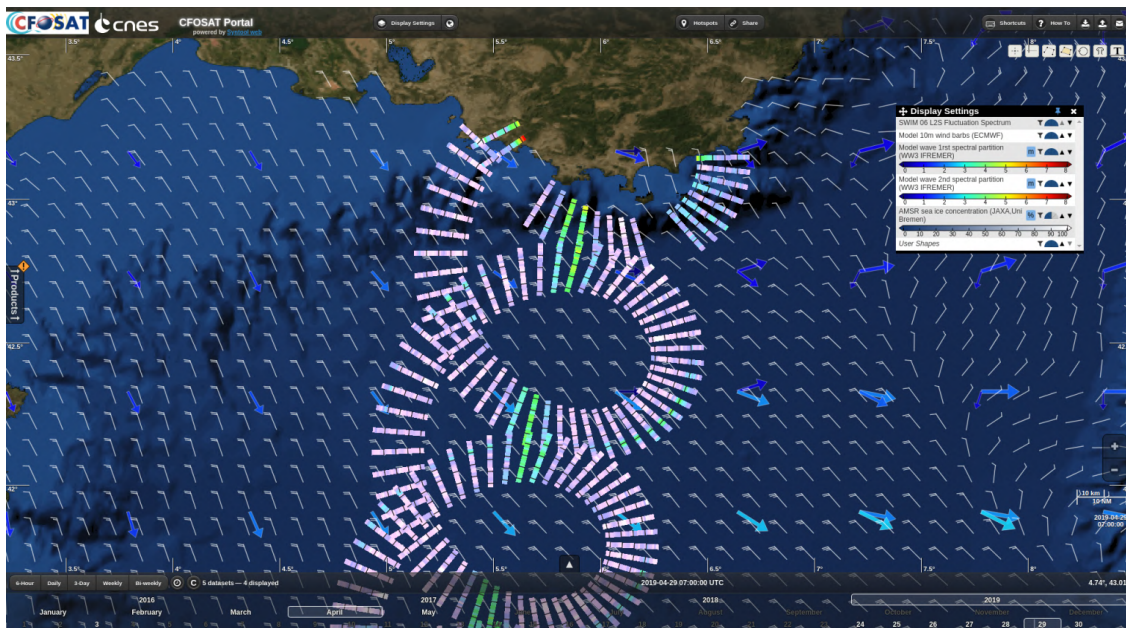


Figure 7-2: An example of fluctuation spectra plotted in the radial geometry of the SWIM scans for the  $8^\circ$  incidence beam. The small colored segments around the cycloid give in each observed direction, the fluctuation spectra as a function of the wave number (wave numbers increasing from the center of the cycloids). The background arrows indicate the wave parameters from the WW3 model for the first spectral partition (direction, wavelength indicated by the vector, significant wave height given by the color code). On this example waves propagating from northwest are well identified in the SWIM fluctuation spectra (with a  $180^\circ$  ambiguity). In addition, the along-track perturbation appears clearly. This case is taken from observations on the April 29<sup>th</sup> 2019 in the Gulf of Lion (North Mediterranean Sea)

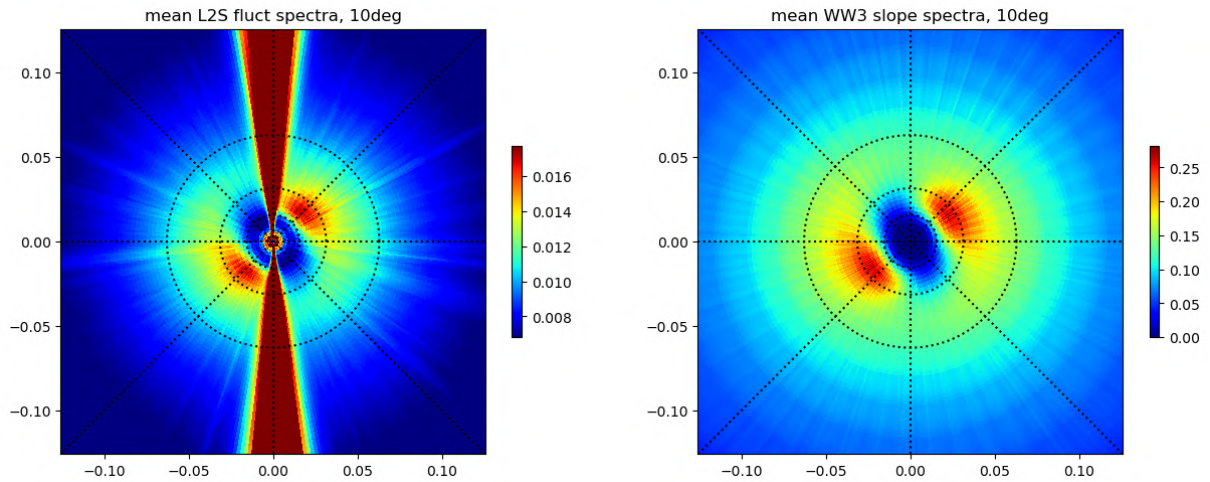


Figure 7-3 : Mean fluctuation spectra for a period of 6 days after April 25<sup>th</sup> (left) compared to the mean wave slope spectrum obtained from collocated points of WW3 outputs (right).

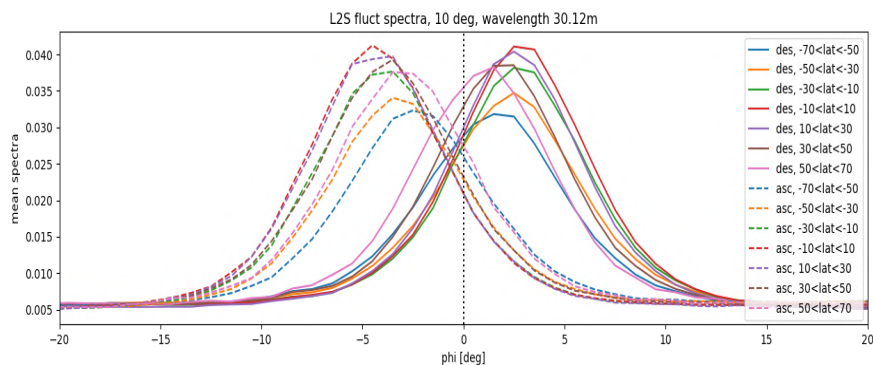


Figure 7-4 : Mean fluctuation spectra around the satellite track direction ( $\pm 20^\circ$  around the satellite track in abscissa) for a wavenumber of  $2\pi/30$  (rad/m). Ascending (resp. descending) tracks are shown in dashed (resp. solid) lines. The different colors are for different latitudes.

This analysis shows that a new model of speckle noise correction must be considered. This is not yet the case in the products up to version 4.3.2 (see below). Work is under progress to estimate an empirical model of spectral density of speckle as a function of wavenumber, azimuth direction and latitude. A tricky part will nevertheless remain: the increase of the standard deviation of the speckle. The mean value can be corrected by an adequate model but the increase on the noise of this statistical variable is more difficult to filter out. The present lack of an appropriate speckle model correction led us to temporarily provide L2 products with a mask applied in the sector perturbed by the along-track speckle noise maximum (see section 8 below).

### 7.3.2 FLUCTUATION SPECTRA COMPARED TO WAVE SPECTRA

In spite of the speckle noise perturbation in the along-track direction, it is still possible to analyze the agreement between SWIM fluctuation spectra and a reference (given here by the WW3 model). Figure 7.5 and 7.6 show such a comparison for mean spectra averaged over 6 days of data. Figure 7.5 shows that the mean fluctuation spectra for beams 6, 8, and 10 ° are in qualitative good agreement with the mean WW3 spectra (except in the along-track direction due to the speckle perturbing effects mentioned above): the energy distribution in the SWIM fluctuation spectra is consistent with that of the WW3 mean

spectra. More quantitatively, Figure 7.6 shows polar plots of the mean coefficient correlation between SWIM fluctuation spectra and WW3 spectra. For beams  $6^\circ$ ,  $8^\circ$ , and  $10^\circ$ , the correlation coefficient is larger than 0.5 for all wavelengths larger than about 60 m and in all directions (except the sector along-track affected by the increase of speckle noise).

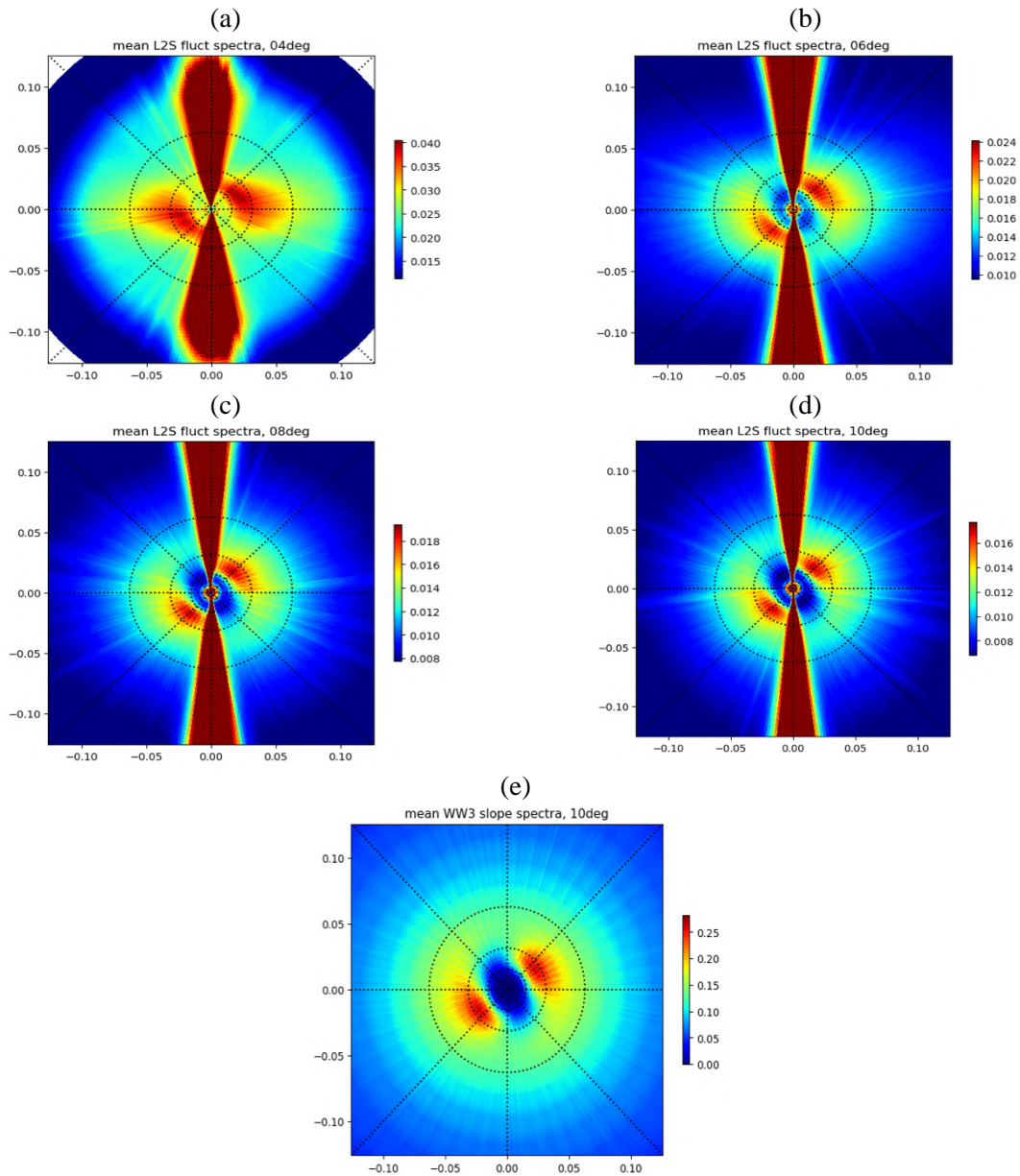


Figure 7-5 : Mean directional spectra (polar plots) of  $\sigma_0$  fluctuations for SWIM incidence beams  $4^\circ$  (a),  $6^\circ$  (b),  $8^\circ$  (c), and  $10^\circ$  (d). The mean was calculated over 6-day data set (2019/04/25  $\rightarrow$  2019/04/30). The horizontal and vertical axis are  $k_x$  and  $k_y$  wavenumbers (cpm) with  $k_y$  aligned along the satellite track direction. (e) mean wave slope spectrum from WW3 for collocated points during the same period of time

Compared to the SAR case, this cutoff wavelength is much less dependent of the direction of waves with respect to the geometry of observations with respect to wave directions, although we still lack of detection in the along-track sector. However, with an appropriate speckle correction (see section 7.3.4 below), it is not impossible that we will retrieve at least part of wave signal in this sector. As expected, for beams 2° and 4°, the correlation with WW3 is degraded compared to the other SWIM beams (6°, 8°, 10°). This is explained by the following reasons: no migration compensation is applied in the on-board processing and the range resolution is less than for the other beams (see Table 2). Indeed, these SWIM beams were not originally designed to retrieve wave information (but mainly to provide mean radar cross-sections). Furthermore, at these near-nadir incidences, the relation between signal modulation spectra and wave slope spectra may become non-linear due to range bunching effects on the signal. Nevertheless, Fig. 7.6 indicates that data from these 2° and 4° SWIM beams contain information on waves although more filtered than for the 6°, 8°, and 10° SWIM beams (correlation coefficient > 0.5 for wavelength > ~250 m and wave directions from about 40° to 140° or -140° to -40° from the along-track direction).

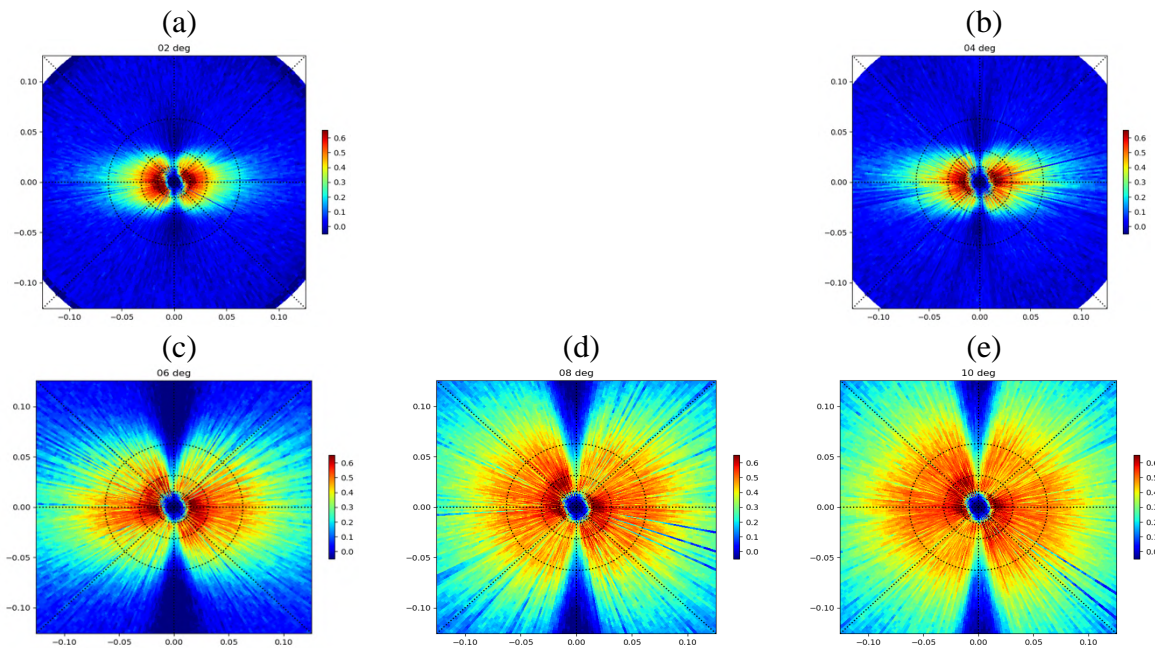


Figure 7-6 : Polar plots of the correlation coefficient between SWIM fluctuation spectra and WW3 collocated wave slope spectra for the data set from April 25<sup>th</sup> to April 30<sup>th</sup> 2019. Horizontal and vertical axes refer to the wave number of the waves in two orthogonal directions, with the vertical axis aligned with the satellite along-track direction. (a) and (b): for SWIM beams 2° and 4°, respectively. (c) to (e): for SWIM beams 6°, 8°, 10° (from left to right)

### 7.3.3 FLUCTUATION STATISTICS

The statistical parameters of  $\sigma^0$  fluctuations have been analyzed, not only in terms of variance but also in terms of skewness and kurtosis (Figure 7-7 below). The results indicate that in the sea-ice region the statistics of variance, skewness and kurtosis are significantly different from free-ice regions. A more detailed analysis is needed but if confirmed, it could help to identify ocean ice (instead of using ancillary data as done up to now and in addition to the mean level of  $\sigma_0$ ). Such statistical parameters may also help to identify non-standard ocean scenes like those affected by rain, bloom, etc. This will be

investigated in the future and flags indicating non-standard oceanic values of these parameters will be refined.

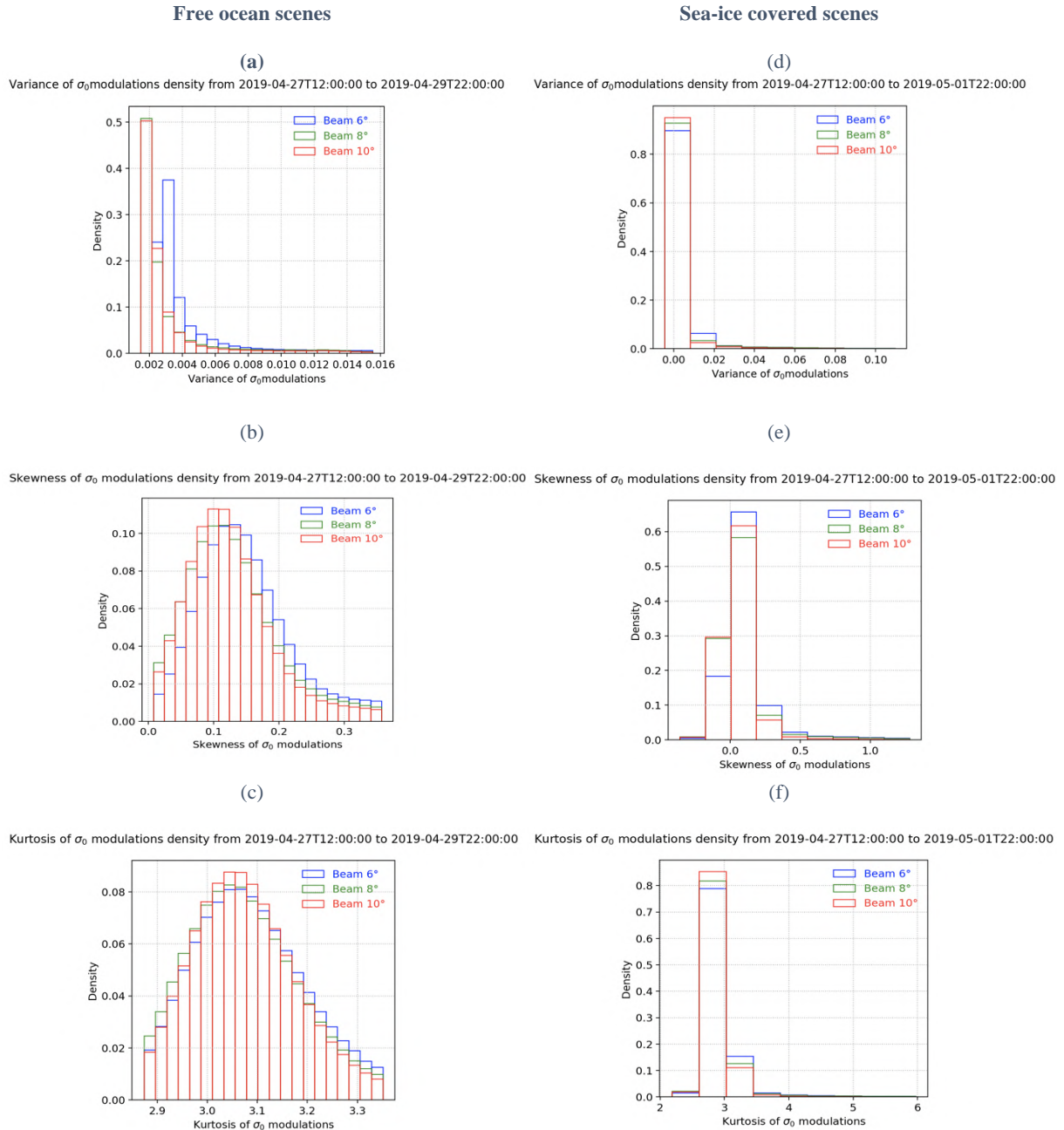


Figure 7-7 : Histograms of variance (a, d), skewness (b,e) and kurtosis (c,f) of the  $\sigma_0$  fluctuations estimated for each footprint for a period of 2.5 days (27-29 April 2019). a, b, c: ocean scenes. d, e, f: sea-ice covered regions. The selection of “free ocean scenes” or “sea-covered scenes” has been carried out by using the ECMWF sea-ice coverage parameter collocated with the SWIM data.

Figure 7.8 shows the mean behavior of variance and skewness of the signal fluctuations with significant wave height (given by the ECMWF model). The sensitivity of variance with significant wave height is visible in Figure 7.8 left. Note that the mean and standard deviation of the variance have been calculated

here by accumulating all azimuths sectors, except the along-track sector of  $\pm 15^\circ$ . So, the sensitivity to significant wave height is smaller than if only wave direction would have been taken into account. Note also that in the mean, the variance of  $\sigma_0$  fluctuations decreases when going from the SWIM beams  $6^\circ$  to  $8^\circ$  and  $10^\circ$ . This is expected and explained by the different number of samples averaged during the on-board processing (156, 186, 204 for 6, 8, and  $10^\circ$  beams respectively) which impacts the speckle noise energy density.

Interestingly, in the same conditions, the skewness of the signal fluctuations shows a clear trend with significant wave height. This parameter is not yet used to estimate wave height but this result could indicate that it would be interesting to consider it. In opposite the kurtosis of the  $\sigma_0$  fluctuations do not exhibit any trend wind significant wave height, except a decreasing trend for  $H_s < 1\text{m}$  (not shown).

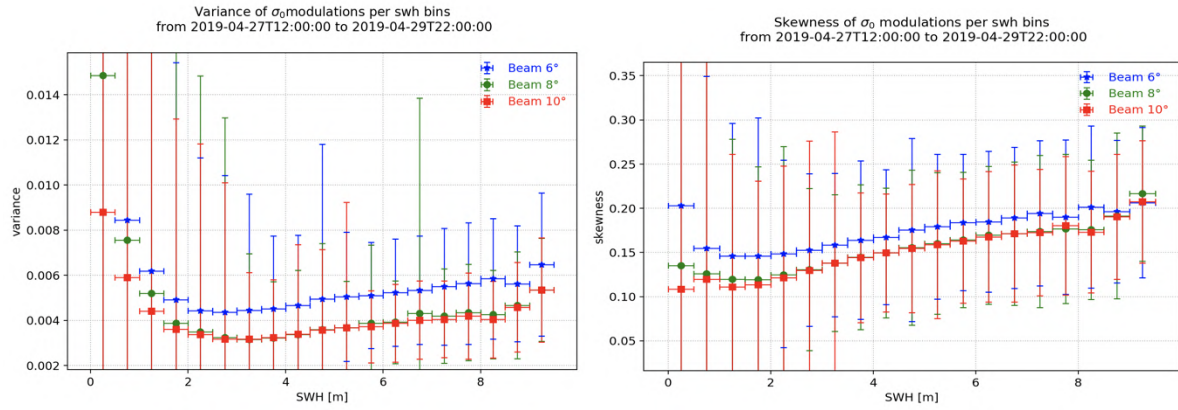


Figure 7-8 : Mean variance (left) and skewness (right) of the signal fluctuations within each footprint as a function of significant wave height (given by the ECMWF model here). Data are averaged over 1,5 days for the  $10^\circ$  beam SWIM observations. The along-track sector affected by the large speckle noise has been excluded in the statistics calculation ( $\pm 15^\circ$ )

### 7.3.4 FIRST ANALYSIS OF THE SPECKLE DENSITY SPECTRUM

As explained in the [2], several options are implemented in the CWWIC processing chain to correct the fluctuation spectra from speckle background effect. One of the CAL/VAL goals is to define the optimal correction. During the first half of the CAL-VAL, this task could not be fully accomplished because of the perturbations mentioned at the beginning of section 7. The first results are however summarized below. As a reminder, the current method (implemented in the current processing chain) to correct fluctuations spectra from speckle noise in the CWWIC processing chain is an analytical model, triangle shaped, given by the following equation:

$$P_{sp}(k) = \frac{1}{N} \frac{\delta r}{2\pi} \frac{1}{\sin \theta} \text{tri} \left( \frac{k}{2\pi} \frac{\delta r}{\sin \theta} \right) \quad (1)$$

where  $\delta r$  is the radar radial resolution (estimated from the Impulse response function),  $\theta$  is the incidence angle,  $N$  is the number of independent samples integrated onboard. Eq. (1) is different from that mentioned in [2] as it considers the Fourier Transform of the real shape of the impulse response function which follows a cardinal sinusoidal shape rather than a Gaussian shape as assumed in the [2].

In the current processing, the number of independent samples  $N_{ind}$  is assumed to be the number of real-time integrated echoes (Table 5), and does not vary with azimuth angles. However, it is clear that it is

not an appropriate assumption, as shown by Figure 7-5. Indeed, the number of independent echoes coincides with the number of integrated echoes only if the Doppler bandwidth is much larger than the PRF [R13]. For side-looking conditions with SWIM, this is indeed the case, but this assumption breaks down for looking angles close to the along-track direction. A detailed analysis of this behavior has been undertaken to characterize precisely the angular sector where this assumption breaks down (due to Earth rotation impact it varies with orientation of the satellite track- ascending or descending- and with the latitude) and to derive a model of speckle noise in this sector from the observation themselves. In order to improve the speckle noise correction, the energy density of the background noise has been estimated separately in the along-track sector perturbed by the lack of Doppler bandwidth and outside thus sector. This is detailed in the next two sections.

### 7.3.4.1 BACKGROUND NOISE OUTSIDE THE ALONG\_TRACK SECTOR

Figure 7-9 shows an empirical estimate of the background noise spectrum outside this perturbed sector; it was obtained by averaging fluctuation spectra selected in azimuth directions where the fluctuation variance is minimum over a 180° sector; these directions are supposed to coincide with directions where the contribution from long waves is minimum. Figure 7-9 shows that the spectrum shape is close to a triangle function for wave numbers larger than about 0.05 rad/m. By applying a fit on this mean spectrum we could estimate the parameters  $\delta r$  and  $N_{ind}$  of Eq.(1). The result of the fit indicates that the slope of the triangle function is larger than initially assumed in Eq. (1), meaning that the effective resolution is coarser than assumed in the theoretical expression: 1.8 m, 2.1 m and 1.6 m respectively for the 6°, 8° and 10° beams compared to the 0.47 m theoretical resolution (see Table 5). This is probably because in the theoretical expression, we omitted for simplicity the impact of the convolution between the impulse response function and the result of the on-board averaging operation (signal averaged and sampled over 2 range bins for beam 6°, and over 3 range bins for beams 8 and 10°). The fit also indicates that the amplitude of the spectrum at the origin is different from that given by Eq (1) leading to values of  $N_{ind}$  (170, 255, 253 for respectively beams at 6, 8 and 10°) that are different from the number of averaged echoes in the signal (see Table 2). Note that until now these estimations have been performed on averaged fluctuation spectra whereas variations may occur depending on the situation. Therefore, this background speckle model needs still to be evaluated in more details. In particular, the impact of surface parameters (wind, waves) need to be estimated.

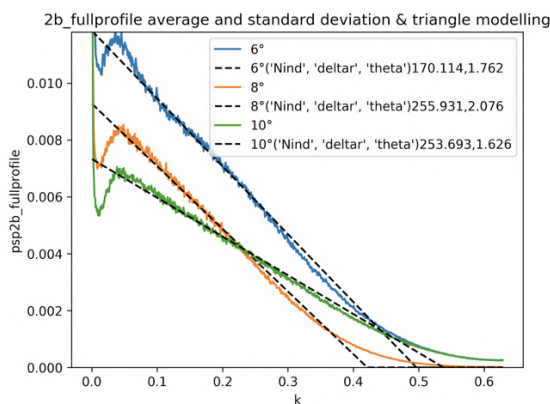


Figure 7-9 : Mean density spectra of  $\sigma_0$  fluctuations as a function of wave number  $k$  (rad/m) averaged over data samples taken in the direction of minimum of  $\sigma_0$  variances for beams 6° (blue), 8° (orange) and 10° (green) and for observations acquired on April 26<sup>th</sup> 2019, between 00h et 12h. The triangle model adjusted on the data (for  $0.05 < k < 0.4$  rad/m) is indicated as dashed lines.

SWIM beam	6°	8°	10°
$N_{ind}$ -estimated	170	255	253
$N_{ind}$ -current value	156	186	204
$\delta r$ - estimated (m)	1.76	2.07	1.62
$\delta r$ - current value (m)	0.47	0.47	0.47
$L_{dis}$	2	3	3

Table 5:  $N_{ind}$  and  $\delta r$  parameters as estimated from the speckle analysis and as currently used in the CWWIC products. The number of range gates used in the on-board integration process is also indicated ( $L_{dis}$ )

### 7.3.4.2 NOISE CHARACTERIZATION WITHIN THE ALONG-TRACK SECTOR

In and close to the along-track directions, the fluctuation spectra are different. This is illustrated in Fig. 7.11 (a-c) . The general trends are similar for the three SWIM beams (6°, 8°, and 10°). It indicates that the density spectrum varies rapidly with azimuth in the first 15 to 20° around the satellite track, both in shape and level.

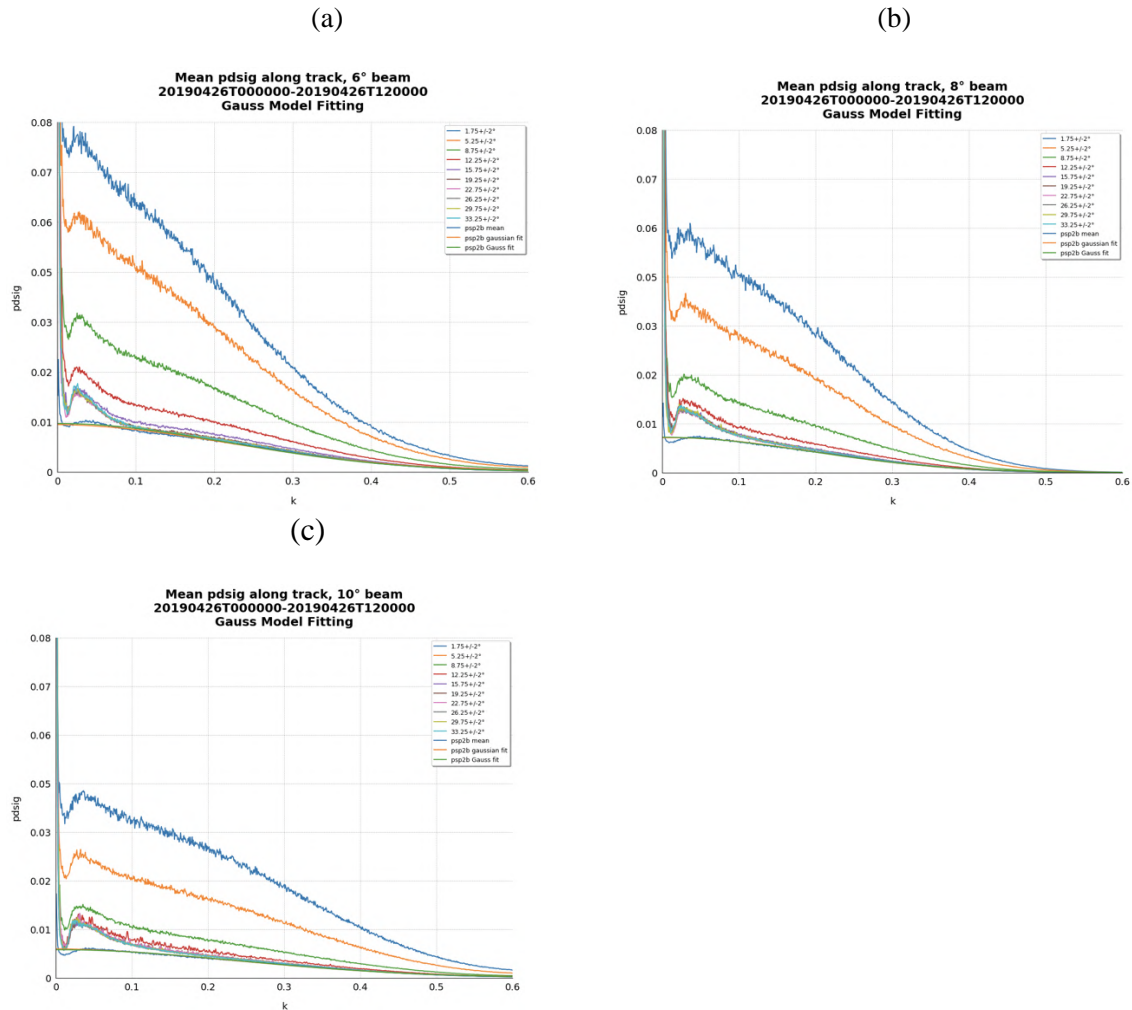


Figure 7-10 : Mean fluctuation spectra averaged by azimuthal sector with respect to the local orbital frame (w.r.t. the along-track direction) and averaged fluctuation spectra in the direction of minimum of variance over sectors of 180° (noted psp2b\_mean in the figure). The time period considered in the average quantities is 12 hours starting on 26 April 2019 00 UTC. (a,b,c): for SWIM beams at 6°, 8°, and 10°

Close to the along-track sector (up to about  $\pm 15^\circ$  from the along track direction), where the Doppler bandwidth is reduced and the energy density spectrum is dominated by speckle noise, fluctuation spectra have a non-linear shape and the energy decreases very significantly from the along-track direction to azimuth angles around  $15^\circ$  with respect to the along-track direction. Very close to the along-track direction its energy at low wave number is up to 7 times higher than in the direction of minimum of variance (curve labeled psp2b\_mean). At more than  $15$  to  $20^\circ$ , the spectral shape remains stable and the wave signal is clearly identified for wavenumbers less than  $0.1 \text{ rad m}^{-1}$ . Moreover, beyond  $k \sim 0.15 \text{ rad m}^{-1}$  (wavelength of about  $42\text{m}$ ) fluctuation spectra is similar to psp2b mean.

These results indicate that a speckle correction dependent on the azimuth angle is necessary in the sector close to the along-track direction and that this correction must converge to the background noise estimated far from this sector (see beginning of this section). Note also that the perturbing effect in the along-track sector is the highest for beam  $6^\circ$  with an amplification factor by a factor of 2 approximatively from beam  $10^\circ$  to bema  $6^\circ$ .

### 7.3.4.3 BUILDING A NEW MODEL OF SPECKLE CORRECTION FOR ALL AZIMUTHS

To build a model applicable for all azimuths, we are currently testing various empirical models which combines a part depending on azimuth in the along-track sector, and a part constant outside this sector. We use the mean fluctuation spectra similar as shown in Figure 7-10 and remove the mean wave contribution in the fluctuation spectrum. A preliminary version of such a model is shown in Figure 7-11.

The impact on the retrieved wave spectrum is illustrated in Figure 7-12 which displays for two examples, a comparison of wave spectra obtained by using i) the processing currently implemented in the operational chain and ii) an alternative correction for speckle density spectrum based on the empirical analytical model presented just above. Although the noise correction is not perfect, the empirical speckle model correction reduces drastically the impact of the along-track background noise and the partitioning is not anymore affected by it (see below). For the case with the presence of waves along-track, this new speckle correction allows to retrieve the waves in the along-track sector.

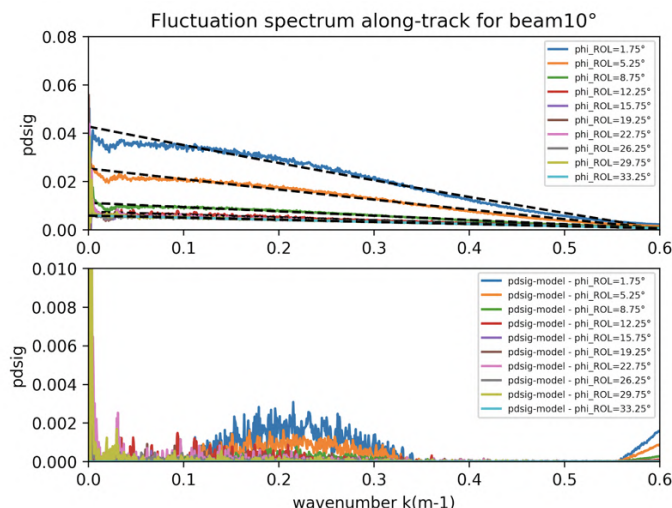


*Figure 7-11 : Top: Analytical model for speckle noise correction in the case of the  $10^\circ$  beam of SWIM (black dashed lines). The model combines a triangle function adjusted on fluctuation spectra in the direction of minimum of variance, and a polynomial function of order 2 in the sector close to the along-track direction. The fluctuation spectra have been corrected from the wave contribution. The different colors refer to different azimuth angles. Bottom: difference between fluctuation spectra and the fitted model.*

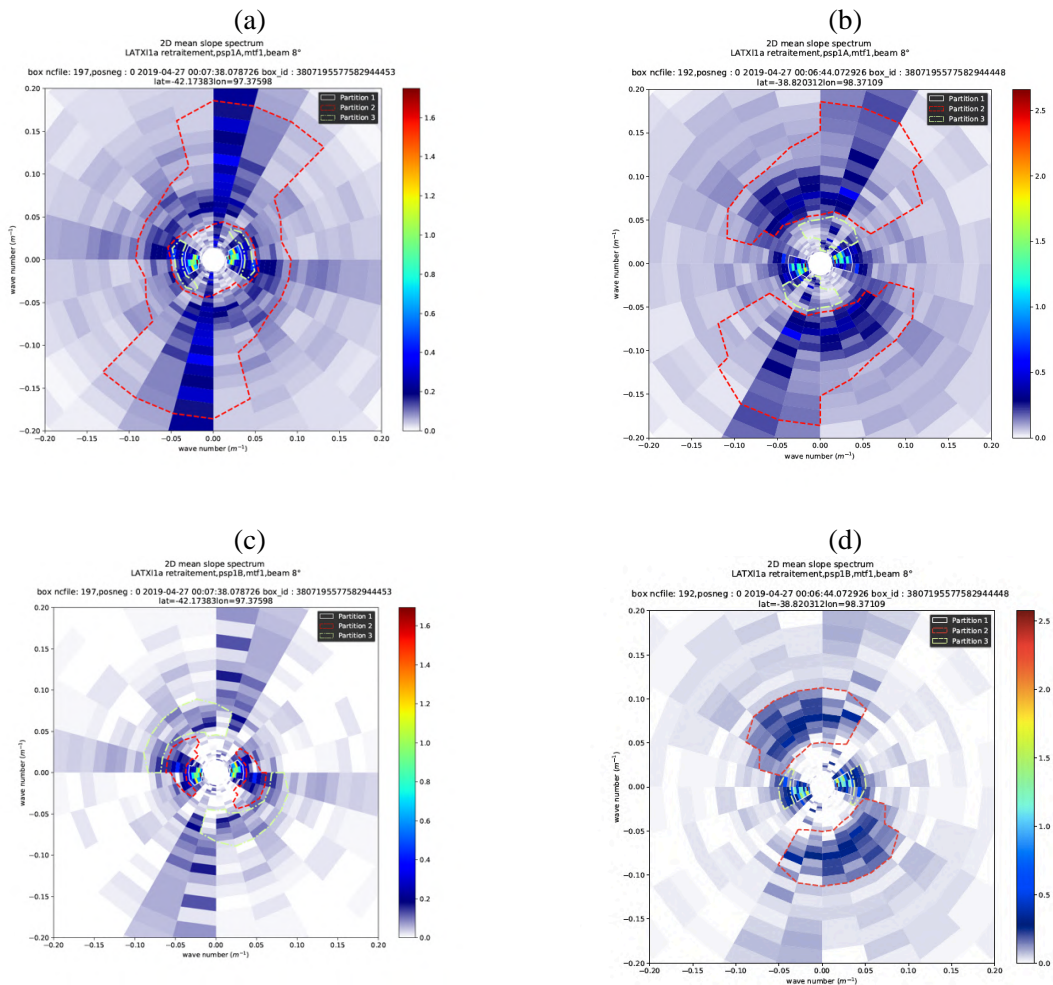


Figure 7-12 : Comparison of wave spectra obtained by applying the speckle correction from: (a) and (c) the analytical correction as currently implemented in the CWICC processing chain; (b) and (d) an empirical model which varies with azimuth to account for along-track perturbations and takes into account a modified background spectrum noise. Here the horizontal and vertical axes refer to the wave number of the waves in the Est-West and North-South directions, respectively. The white, red and yellow contours indicate the partitions found in each case.

## 7.4 FORESEEN ANALYSES AND EVOLUTIONS

### 7.4.1 PLANNED PROCESSING EVOLUTIONS

The main evolution in the future will concern the speckle correction model. Presently, there is no correction for speckle in the IWWOC product whereas in the CWWIC products, the speckle correction is the one defined before launch which does not vary with azimuth (with a large underestimation in the along-track direction  $\pm 15^\circ$ ) and for which the background noise outside the along-track direction seems to be underestimated. Starting with the processor version 4.3.0, there is a possibility to correct for speckle with an empirical model varying with azimuth and latitude, but this option is not activated yet, because we are still working on the coefficients of this empirical model to analyze also the dependence on sea-state; further evolutions may take into account a speckle model which also depends on sea state variables.

#### 7.4.2 FORESEEN ANALYSES

In the next months, an important effort will be put on the speckle estimation in order to propose the best method of estimation and correction. It will take into account the variation of speckle properties with direction with respect to the along-track satellite. This will allow to avoid or reduce the perturbing effects evidenced in all wave spectra as mentioned in sections 7 and 8 (along-track  $\pm 15^\circ$  perturbation) and to reduce the background noise for all directions. Validation of the proposed empirical model will also be performed by using other possible empirical estimates of speckle noise using either the cross-spectral method (see the PUG) and/or the speckle mode of acquisition.

Statistical parameters of the  $\sigma^0$  fluctuations need to be analyzed in more details to propose flags which could mark non-standard ocean scenes (sea-ice, rain, etc).

Finally, more analysis will be done to extend the IWWOC products to wave spectra estimated from the 2 and 4° beams. Although this was not initially specified, the first results show that indeed the  $\sigma^0$  fluctuations at these incidences are well detected and can be related to the presence of waves. The transfer function which relates the fluctuation spectra to wave spectra needs however to be better qualified (the limit of a linear transfer function with respect to wave slope spectra is probably reached at these incidences, see section 8.3).

## **8 - L2 PRODUCTS (L2 CWWIC)**

### **8.1 VARIABLES ANALYZED**

For the CWWIC products, we recall that the main transformations between Level1B and Level 2 are the following:

- the radial modulation spectra (i.e. radial spectra of  $\sigma^0$  fluctuations corrected from the speckle noise) are resampled in wave number (65 wave numbers) and azimuth (12 bins of  $15^\circ$  over  $180^\circ$ ),
- the radial modulation spectra are transformed into wave slope spectra by applying a « Modulation Transfer Function » (MTF). In the CWWIC processing chain, this MTF is supposed to be independent of the wave number of the waves (linear model) and up to four possibilities to estimate the MTF are implemented in the processing chain (See the PUG for more details). Until now, only the MTF1 was tested. MTF1 uses an estimate of the mean falloff of  $\sigma^0$  with incidence angle, in each azimuth direction.
- the different directions of the wave spectra are then combined to build the polar directional wave spectra at the scale of “wave box” of about 70km x 90 km (in the nominal mode of SWIM acquisition).
- a partition scheme is applied to detect up to 3 partitions
- wave spectral parameters (significant wave height, peak direction and peak wavelength are calculated on the full polar spectrum and on up to 3 partitions.

For the IWWOC products, the processing does not include yet the transformations to pass from fluctuation spectra to wave slope or wave height spectra. Work is going on to do so, and will basically include the same first two steps as described just above. A preliminary study of the MTF is presented in section 8.4.

### **8.2 VALIDATION METHOD AND DATA SET USED FOR ANALYSIS**

Because of the problem initially encountered in the fluctuation spectra (see section 7), and also because of uncertainties remaining in the  $\sigma^0$  profiles with incidence (see section 6), the validation at this stage remains preliminary.

Results from data sets acquired since April 25<sup>th</sup> 2019 are presented in section 8.3. The analysis was performed on products generated by a prototype of the 4.3.1 processing chain where the L2 wave spectra are masked in the along-track direction before applying partitioning and before calculating main parameters (wave height direction, wavelength,...). This allows to avoid inconsistent detection of partitions and estimation of parameters while the speckle correction is not yet optimal. This is illustrated in Fig 8.1 below.

The products analyzed in section 8.3 were obtained using the MTF1 version of the Modulation Transfer Function (MTF) which uses the measured mean trend of  $\sigma^0$  with incidence (between 0 and  $10^\circ$ ).

In a first stage of the analysis the wave parameters of the partitions were taken from the products and associated for comparisons with partitions of MFWAM model as provided by the MFWAM partitioning scheme. The results are presented in sections 8.2 and 8.2.2 below.

In a second stage of the analysis (done very recently), we also re-partitioned the MFWAM spectra and applied the partitioning masks of MFWAM to the SWIM spectra (section 8.2.3). At this stage of the validation, we are more confident in this latter analysis because it separates analysis of error due wave parameter estimations to errors due to partitioning. However, in this report we keep the results obtained from the analysis of the SWIM partitions contained in the product because they show that improvement needs also to be done on partitioning. Considerations on partitioning are discussed in section 0 .

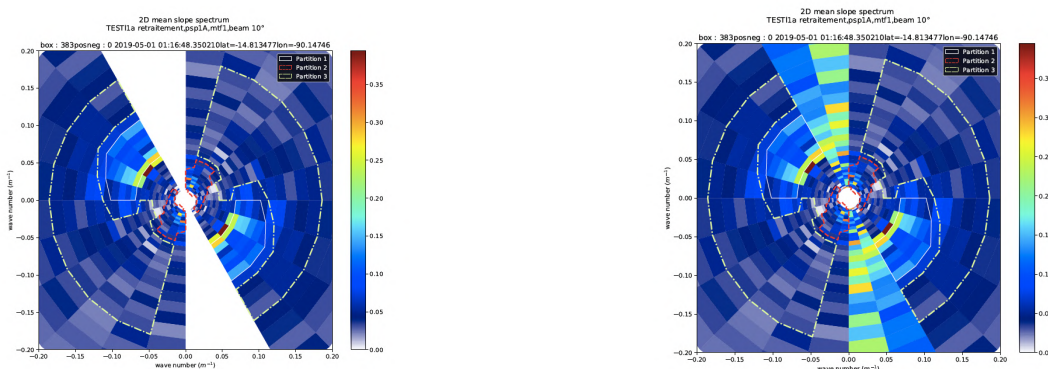


Figure 8-1 : 2D Wave spectrum from the CWWIC product. Left with the mask applied, right without the mask. The partitions (contours in solid white, red lines, and dashed yellow line) are estimated on the masked spectra to avoid a detection of partition in the along-track perturbed sector.

## 8.1 COMPARISONS OF THE DIRECTIONAL SPECTRA FROM DIFFRENT BEAMS AND WITH MFWAM SPECTRA

Wave spectra contain a large quantity of information (energy, wavelength, direction) so that it is not easy to conclude on their intrinsic quality. In order to synthetize the information, we proposed to analyze correlation indexes and quadratic differences between pairs of spectra (between SWIM spectral beams and between each spectral beam and the MFWAM spectra- masked as the SWIM spectra). The correlation index is expressed as proposed in [R13]. Figure 8-2 illustrates the maps of correlation index for a 13-day period (26 April-9 may) for (a) difference between spectra from beams 6 and beam 10°; (b) difference between spectra from beam 10° and MFWAM spectra.

For the comparison between SWIM beams, the largest correlation indexes for all pairs are observed in the highest sea states as shown by comparing Fig 8-2 to right-hand map of Fig.8-6 which gives the  $H_s$  map for the same period. In opposite, the smallest values of correlation and highest values of quadratic difference are observed either in the low sea state regions ( $H_s < 1m$ ) or regions impacted by signal inhomogeneity (with probable occurrence of rain in particular- see Figure 5-14 in section 5.3. Overall, a correlation index better than 0.5 is observed for 75% of the pairs 8°-10° (best combination for 6°-8° with 84% of correlation index larger than 0.5). The histograms of the correlation indexes and of the quadratic differences (Figure 8-2 c and d) have a tail in their distribution, which should enable us in the future to define threshold values of these quantities to better flag or reject data of lesser quality. Same results were obtained for other pairs of spectra (6°-8° and 8°-10°).

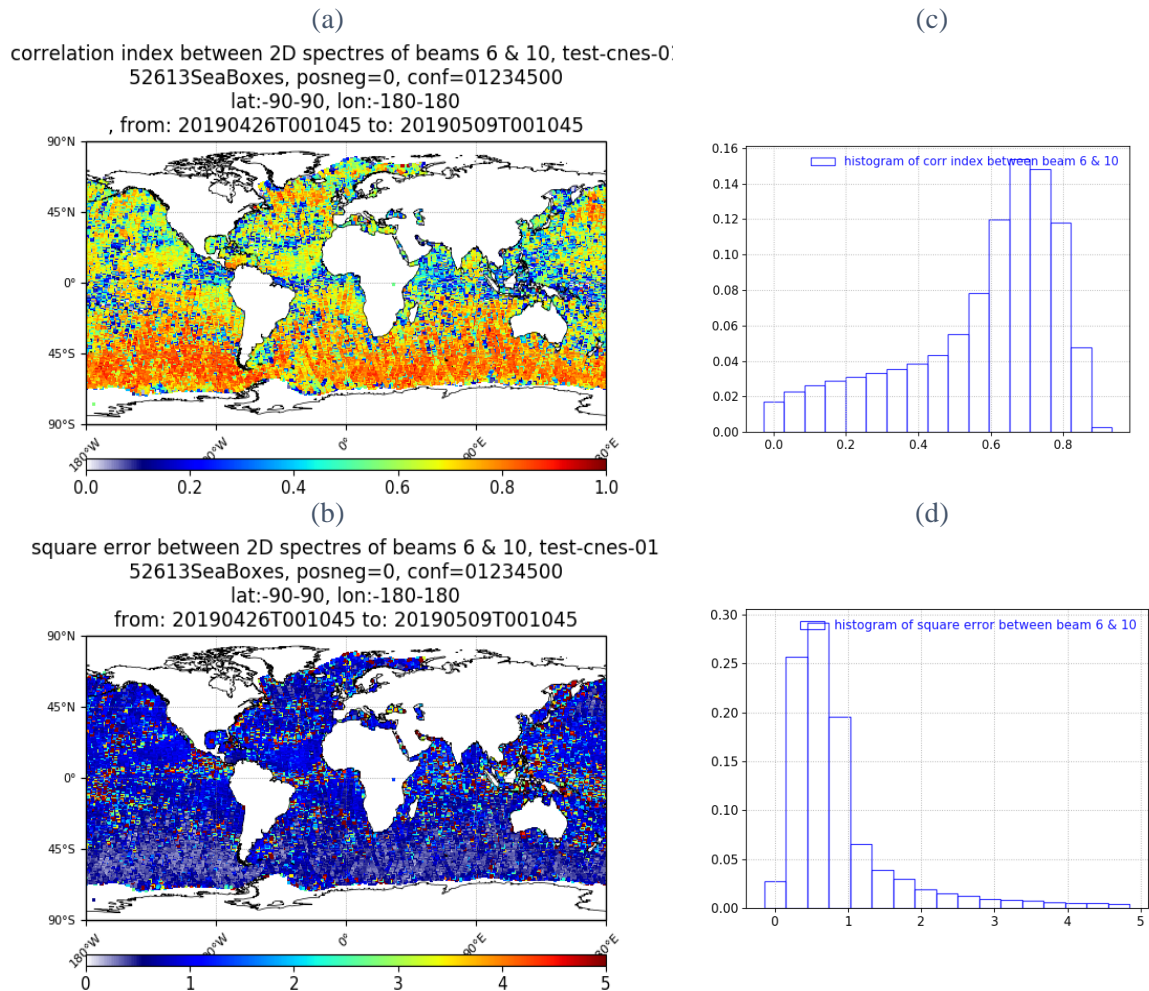


Figure 8-2: Map correlation index (a) and quadratic difference (b) between pairs of spectra from SWIM beam 10° and SWIM beam 6° (c) and (d) : corresponding distribution

Correlation indexes between spectra from SWIM-beam 10° and from MFWAM are presented in Fig. 8-3). It shows that i) the correlation index is less than between pairs of SWIM spectra (54 % have a correlation index larger than 0.5), ii) the correlation is also the best in high sea state conditions. At  $H_s$  less than 1m, the correlate index drops to about 0.2 and the quadratic error is maximum. The statistics of the correlation index and quadratic difference also indicate that spectra from the 10° incidence beam are in better agreement with MFWAM than those from spectral beams at 8° and 6° for which the correlation indexes are of 52% and 50%, respectively.

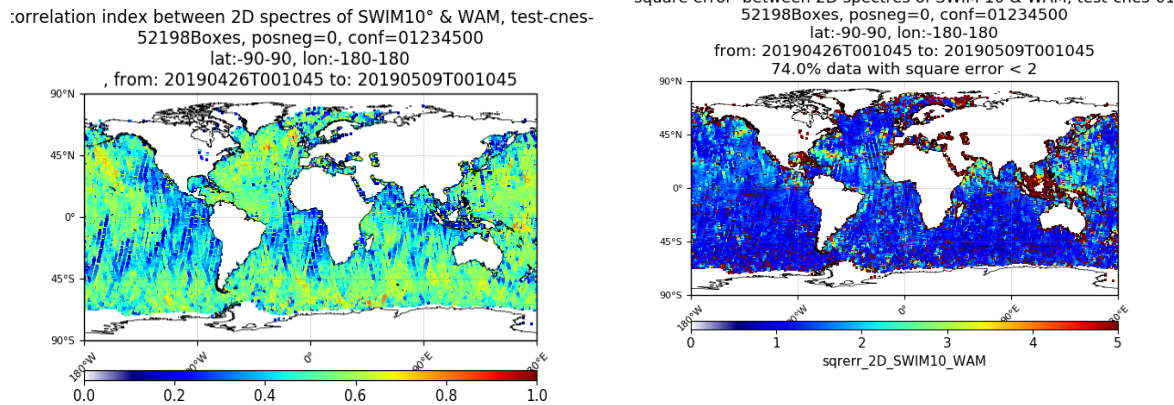


Figure 8-3: Map of correlation index (a) and quadratic difference (b) between pairs of spectra from SWIM beam 10° and MFWAM.

## 8.2 STATISTICS AND MAPS OF WAVE PARAMETERS

### 8.2.1 SIGNIFICANT WAVE HEIGHT OF THE WAVE SPECTRA

Continuing with the analysis of the full spectra, figure 8-4 shows scatter plots (as 2D histograms) for the total significant wave height from SWIM for beam 6°, 8°, and 10° compared to MFWAM significant wave height. For all beams, it clearly shows that although the correlation is rather high (correlation coefficient larger than 0.96 and rmse less than 0.28 m), there is a significant positive bias on the significant wave height for all wave heights smaller than 4 to 5 m. At larger wave heights (> 5-6 m) the bias becomes negative. The departure from the 1:1 slope in the relation between  $H_s$  from SWIM and  $H_s$  from the reference is more pronounced for the beams 6 and 8 degrees than for the 10-degree beam.

In order to check the impact of the SWIM spectrum mask in this comparison, we also recalculated the MFWAM significant wave height from the MFWAM spectra but by applying the same mask as done on the SWIM data. The results (Figure 8-5 for beam 10°) indicate that in this case the negative biases at large  $H_s$  are slightly reduces but those at  $H_s < 4$  m are only marginally reduced. This means that the main part of the positive bias evidenced at  $H_s < 4$  m cannot be attributed to the energy lacking in the along-track direction masked in the SWIM spectra.

Figure 8-6 shows the comparison between SWIM and MFWAM as geographic maps and for the 10° beam only. The conclusion are qualitatively similar with an overestimation of  $H_s$  in all regions where  $H_s$  is below 4 m approximatively.

In summary this analysis on total  $H_s$  leads to conclude that when calculated over the whole SWIM spectrum without partitions,  $H_s$  values are significantly overestimated at  $H_s$  smaller than about 4 to 5 m compared to model data. The same conclusion was obtained by comparing to ECMWF  $H_s$  or nadir  $H_s$  (not shown). A small underestimate is also observed at large  $H_s$  (above 6-7m), but it still needs to be quantified by using a larger set of data.

At this stage of the analysis, we think that the main cause of the overestimation at small to moderate  $H_s$ , is due to the remaining background noise in the wave spectra as illustrated in Figure 8-1. This is consistent with the conclusion on speckle estimation (see section 7.3.4), which shows an underestimate of speckle noise density spectrum, not only in the sector close to the along track direction but in also in

other directions. This underestimation of speckle means that the fluctuation spectra are not enough corrected from speckle noise energy density, and this impact increases when energy of the wave spectra decreases. This effect may also combine with an underestimate of MTF (see section 8.2.3 and 8.4).

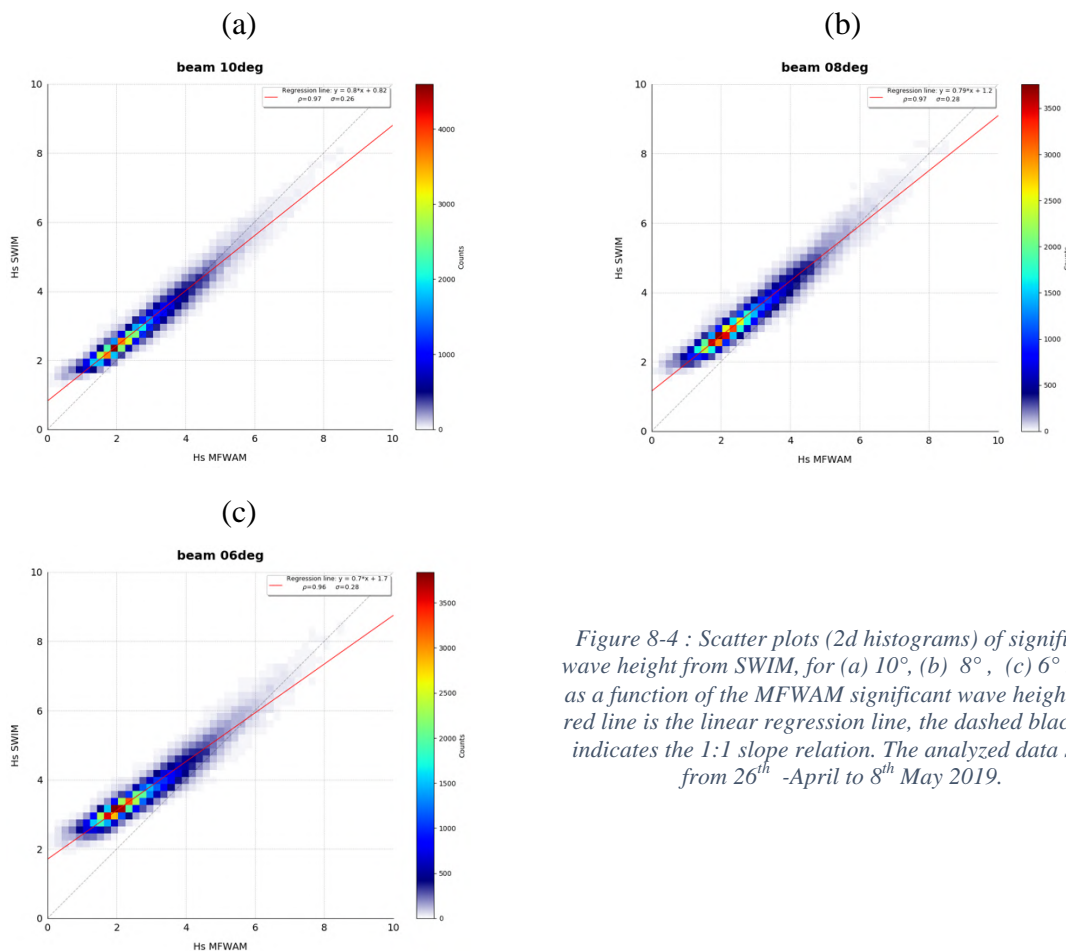


Figure 8-4 : Scatter plots (2d histograms) of significant wave height from SWIM, for (a) 10°, (b) 8°, (c) 6° beam, as a function of the MFWAM significant wave height. The red line is the linear regression line, the dashed black line indicates the 1:1 slope relation. The analyzed data set is from 26<sup>th</sup> -April to 8<sup>th</sup> May 2019.

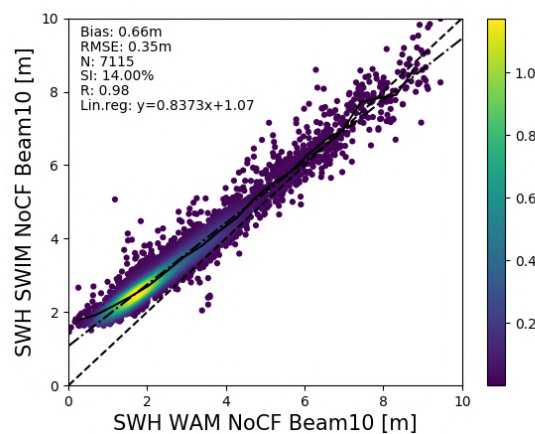


Figure 8-5 : Total significant wave height of SWIM (beam 10°) with respect to HS from MWAM spectra estimated by removing on both types of spectra the azimuth sector affected by the increased level of noise in the SWIM data.

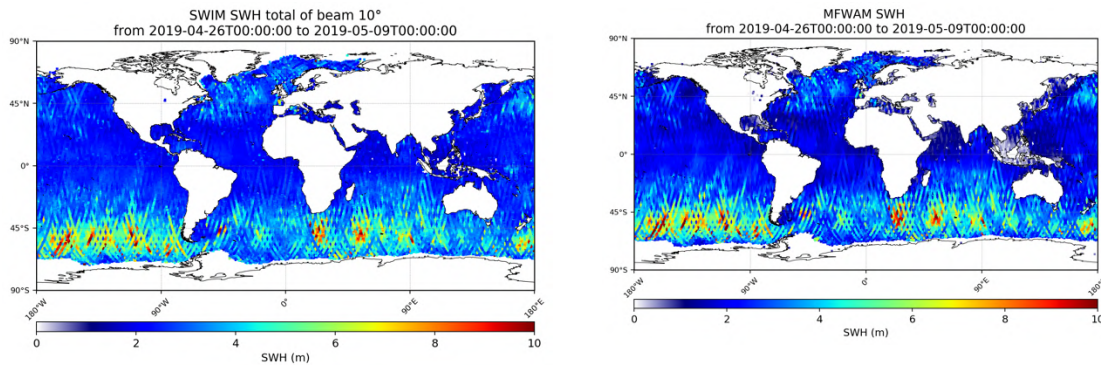


Figure 8-6 : Maps of SWIM (left) et MFWAM (right) total significant wave height for a period of about 13 days starting on April 26th 2019 02 :00. SWIM data are from the 10° beam in the left plot.

## 8.2.2 WAVE PARAMETERS FROM THE SWIM PRODUCTS PARTITIONS

In this section and the following one, we concentrate on the wave parameters estimated from partitions. Working with partitions is a way to better concentrate on the parameters of dominant wave systems and so, minimizing the contribution of the background noise (which is not properly corrected at this stage).

In this section, wave partitions are taken from the SWIM products and compared to wave parameters provided by the MFWAM model internal partitioning algorithm (first swell partition as found by the Meteo-France partitioning algorithm). Results obtained from the beam at 6° and 8° incidences are not presented here but give very similar conclusions.

Comparisons show that the significant wave height of the first partition is in overall good agreement, in particular for high sea-states ( $H_s \geq 3$  or 4 m) –see Figure 8-7 (a-d). At smaller wave heights, SWIM tends again to overestimate  $H_s$  compared to model values. Dominant direction (Figure 8-7 b-e) and wavelength (Figure 8-7 c-f) of the first partition are also generally in agreement except in some regions of the globe. Part of the disagreement evidenced in these regions is due to the mask applied on SWIM data (but not on MFWAM) so that for waves propagating in the along-track direction, the first partition in SWIM data cannot be found in this direction. This is clearly the case in the Arabic sea East of Africa, and along the coast of California in America. Note also that at in this analysis the association between SWIM and MFWAM is simple (first partition of SWIM associated with first partition of MFWAM). So part of the disagreement may also come from this too simple cross-assignment. This will be confirmed by the next section.

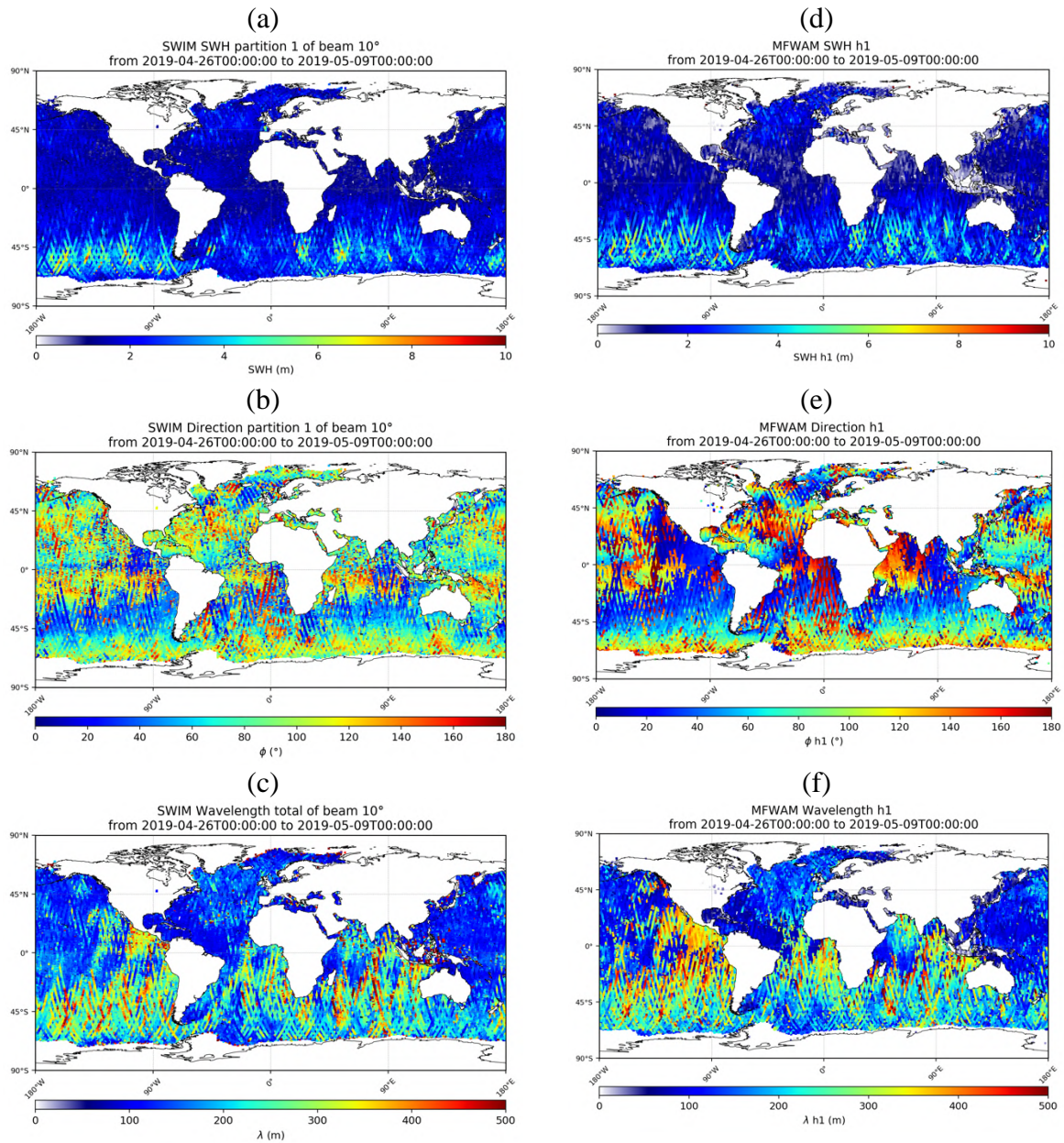
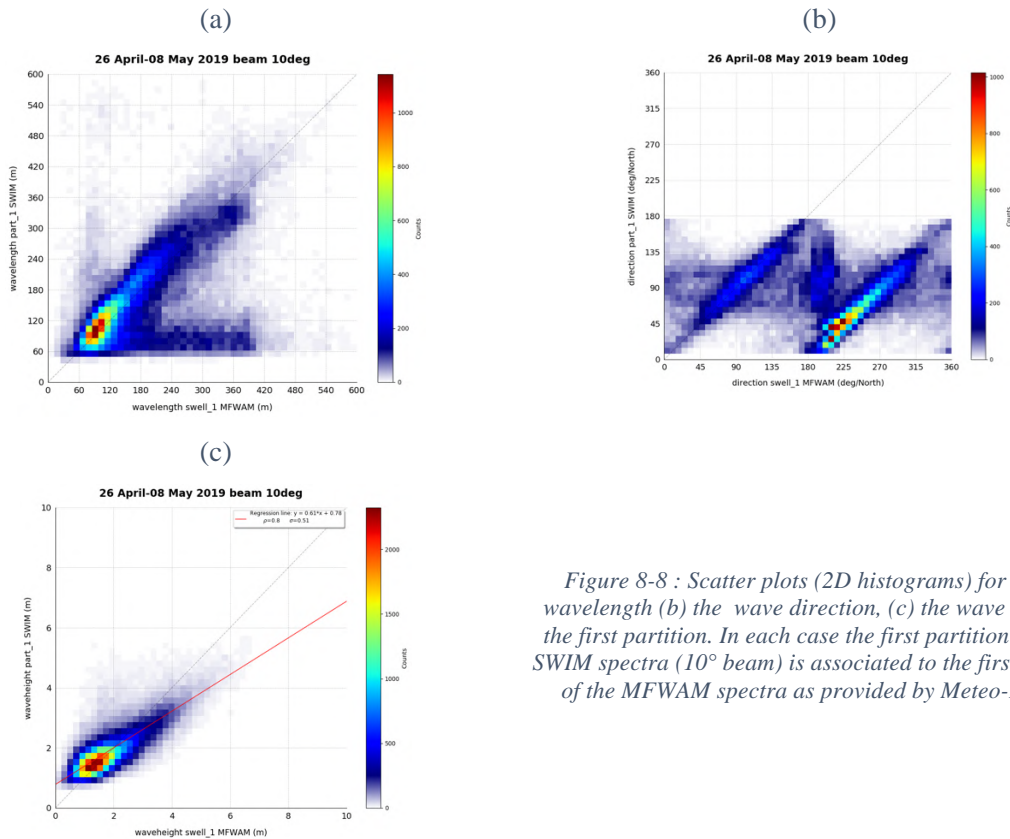


Figure 8-7 : Maps of SWIM (a-b-c) et MFWAM (d-e-f) parameters of first spectral partition for a period of about 13 days starting on April 26<sup>th</sup> 2019 02 :00. (a, d): Significant wave height of the first partition, (b, e): direction of the first partition, (c,f): wavelength of the first partition. For SWIM, the processing version is the prototype of version 4.3.0. The SWIM results are shown for the 10° incidence beam. For MFWAM, the parameters are taken from files provided by Meteo-France based on their own partitioning method.



*Figure 8-8 : Scatter plots (2D histograms) for (a) the wavelength (b) the wave direction, (c) the wave height of the first partition. In each case the first partition from the SWIM spectra (10° beam) is associated to the first partition of the MFWAM spectra as provided by Meteo-France*

Figure 8-8 shows the scatter plots of the SWIM first partitions parameters (beam 10°) as a function of wave parameters of the first swell partition of MFWAM (as found by the partitioning algorithm internal to MFWAM). The data set is similar to the one illustrated as geographic maps in Figure 8-7. For wavelength and direction, we see two populations of data with a very good agreement for the majority of the data set but also a disagreement, which we attribute due to the mask applied on SWIM data (but not on MFWAM) so that for waves propagating in the along-track direction, the first partition in SWIM data is associated to partition which cannot be in this direction.

As mentioned above, the association between SWIM and MFWAM parameters is very simple in these figures (first partition of SWIM associated to 1st swell of MFWAM). We show in the next session the same kind of comparisons but by imposing the same partitions on both MFWAM and SWIM spectra. We checked that this is the case in the Arabic sea East of Africa, and along the coast of California in America. In addition, the association between SWIM and MFWAM is simple here (first partition of SWIM associated with first partition of MFWAM provided as output of the operational model), so that part of the disagreement may also come from the lack of cross-assignment. Figure 8-9 illustrates this problem with two wave spectra from SWIM in almost the same conditions compared to the MFWAM spectrum. The detection of the first and second partitions are inverted from one SWIM case to the other, although the MFWAM spectra are very similar. This clearly shows that the partitioning algorithm for SWIM needs to be tuned in order to be less sensitive to background noise. This will be done once the background noise is better evaluated and subtracted.

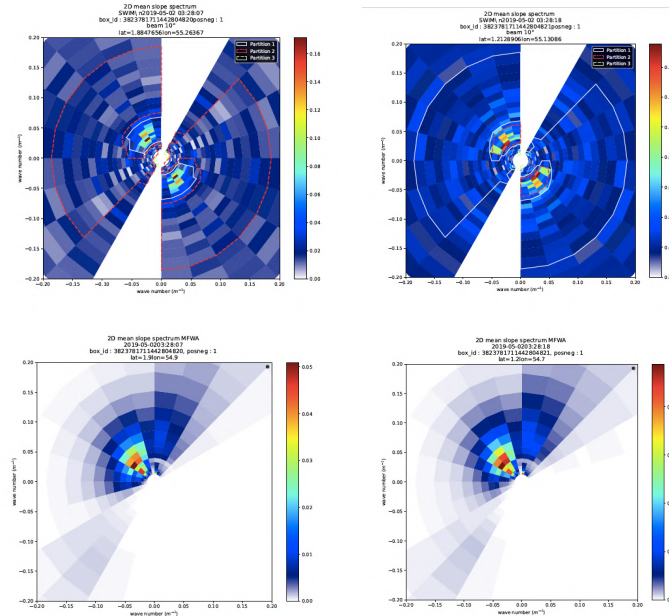


Figure 8-9: Top: wave spectra from SWIM (beam10°) and their associated partitions (in white, dashed red the first and second partitions, respectively). Bottom: associated wave spectra from MFWAM

### 8.2.3 ANALYSIS USING PARTITIONS ESTIMATED A POSTERIORI FROM THE MFWAM MODEL

In this section the comparison between SWIM and MFWAM on wave parameters is carried out by taking MFWAM partitions as the reference and considering the same domain of partitions for SWIM. For this purpose, first, MFWAM directional spectra have been symmetrized to provide the same type of observations as SWIM (with 180° ambiguities in direction). Then, MFWAM spectra have been partitioned on the symmetrized spectra using the watershed algorithm as in the L2 products, including cutoff imposed at low wave number ( $k < 0.0102$  rad/m). The azimuth masks have then been applied to remove the energy similarly to SWIM masked spectra, and the integral parameters have been estimated ( $H_s$ , peak wavelength and peak direction) for each partition following the methodology indicated in the SWIM Product User Guide.

The advantage of this approach is that it enables us to separate the effect of possible errors due to the inversion algorithm from those due to the partitioning results. By analyzing the parameters calculated on the same partitions, the objective is i) to analyze potential differences with respect to the reference (MFWAM model partitions) due to inversion algorithm, ii) to compare the results between the different beams of SWIM in identical spectral domains, iii) to compare the results for different orders of partitions. It must be noted, that will also be necessary in the future to evaluate the partitioning methods based on the SWIM data only.

Table 6 provides the results for each SWIM beam configuration, for the different partitions (up to 3) and for the case where all the partitions are considered together.

	Beam 6°	Beam 8°	Beam 10°
<b>Hs</b>			
Nb of points	- all : 31913 - part 1 : 13895 - part 2 : 10996 - part 3 : 7022	- all : 31785 - part 1 : 13842 - part 2 : 10950 - part 3 : 6993	- all : 31582 - part 1 : 13755 - part 2 : 10880 - part 3 : 6946
Mean bias	- All : 0.86 - part 1 : 0.97 - part 2 : 0.98 - part 3 : 0.69	- all : 0.65 - part 1 : 0.73 - part 2 : 0.62 - part 3 : 0.53	- All : 0.45 - part 1 : 0.47 - part 2 : 0.44 - part 3 : 0.40
Rmse	- all : 0.39 - part 1 : 0.42 - part 2 : 0.35 - part 3 : 0.30	- all : 0.33 - part 1 : 0.37 - part 2 : 0.30 - part 3 : 0.27	- all : 0.27 - part 1 : 0.32 - part 2 : 0.23 - part 3 : 0.19
Scatter index	- all : 29.2% - part 1 : 19.5% - part 2 : 40.4% - part 3 : 72.3%	- all : 25.0% - part 1 : 17.0% - part 2 : 34.4% - part 3 : 64.1 %	- all : 19.9% - part 1 : 14.6% - part 2 : 26.3% - part 3 : 46.5%
<b>Direction</b>			
Mean bias	-all : -1.0° - part 1 : -0.7° - part 2 : -1.8° - part 3 : -0.5 °	-all : -0.5° - part 1 : -0.4° - part 2 : -0.8° - part 3 : 0.0°	-all : -0.4° - part 1 : -0.5° - part 2 : -0.4° - part 3 : 0.0°
rmse	- all : 21.8° - part 1 : 20.1° - part 2 : 23.2° - part 3 : 22.8°	- all : 20.8° - part 1 : 18.5° - part 2 : 22.2° - part 3 : 22.8°	- for all : 18.5° - part 1 : 16.1° - part 2 : 19.3° - part 3 : 22.8°
<b>Wavelength</b>			
Mean bias (m)	- all : 20 - part 1 : 13 - part 2 : 24 - part 3 : 30	- all : 13 - part 1 : 4 - part 2 : 15 - part 3 : 26	- all : 7 - part 1 : -1 - part 2 : 7 - part 3 : 23
Rmse (m)	- all : 82 - part 1 : 79 - part 2 : 87 - part 3 : 80	- all : 76 - part 1 : 69 - part 2 : 82 - part 3 : 78	- all : 70 - part 1 : 62 - part 2 : 76 - part 3 : 75
Scatter Index	- all : 36.9 % - part 1 : 42.7% - part 2 : 38.0 % - part 3 : 27.7%	- all : 34.2% - part 1 : 37.3% - part 2 : 35.8 % - part 3 : 27.0%	- all : 31.7% - part 1 : 22.3% - part 2 : 22.4% - part 3 : 26.1%

Table 6: Statistical scores for the comparison between the wave parameters (significant wave height Hs, dominant direction, dominant wavelength) of the MF-WAM wave spectra partitions and of the SWIM spectra partitions. The data set covers from April 25<sup>th</sup> to June 10<sup>th</sup> 2019 processed with version 4.3.0

The first comment from this analysis is that parameters from beam 10° give the best agreement to the reference compared to results from the other SWIM beams. This is true for all parameters and all statistical indicators (mean bias, rms difference, scatter index). The reason is probably twofold: beam 10° is the less sensitive to possible wind fluctuations within the footprint, and it is associated with the smallest speckle noise perturbation.

The second comment is that for all conditions (all beams and all partitions), we find here gain, as in the analysis on the total spectrum and with crude partition associations, a positive bias of SWIM Hs with respect to MFWAM Hs. This bias ranges from 0.47 m (beam 10°, partitions #1) to 0.98 m (beam 6° partitions #2). Because this bias is observed for all beams and is the largest for beams 6° and 8°, we think that this is due to insufficient speckle noise correction with a largest underestimation of speckle for beam 6° and 8° as compared to 10° as found with our empirical estimate of speckle (see section VII).

Another reason could be an error in the MTF estimation but this latter is the same for all beams, as it is estimated on the mean profile of  $s_0$  from 0 to  $10^\circ$ .

The third comment is that the scatter index for  $H_s$  increases with the order of the partitions (sorted by decreasing energy). For beam  $10^\circ$  for example, the scatter index on  $H_s$  is less than 15% for partition 1 but increases to 26% and 46% for partitions 2 and 3, respectively, although the rms error remains between 20 and 30 cm (this can be explained by the definition of the scatter index which uses the  $H_s$  value for the normalization). Correlatively the rms error on direction slightly increases with the partition order ( $16^\circ$  to  $23^\circ$  for beam  $10^\circ$ ). As for the wavelength of partitions, the scatter index is of the same order of magnitude for partitions 1 and 2 and decreases for partition 3. This seems to indicate that even if the accuracy decreases with the order of partition for  $H_s$ , the information on the wavelength of the partitions remains reliable for the lowest energetic partitions. One of the reasons could be that the first partitions, which are generally swell dominated, are more perturbed in the SWIM spectra by artefacts due to non-homogeneous scenes induced for example by rain, currents, islands, etc (these cases are not yet flagged nor rejected in the data).

### 8.3 ADDITIONAL CONSIDERATIONS ON THE WAVE SPECTRUM PARTITIONING

The current partitioning scheme used in CWWIC products relies on a watershed algorithm in order to delineate wave systems in the directional wave spectra. With several examples illustrated below, we show how the spectra are sometimes under- or over-partitioned which biases the energy of the partitions and leads to miss some wave systems.

In Figure 8-12 below, two collocated spectra from SWIM (combined slope spectrum) and Sentinel-1 (Wave Mode) are shown. The associated roughness images from Sentinel-1 (S1) is also shown. A clear crossed-sea can be seen on both the roughness image and S1 spectrum, with measured  $H_s$  larger than 2m for the two wave systems. Although the two peaks can be clearly seen on SWIM combined spectrum, the partitioning algorithm fails in separating the two.

This may be due a lack of constrains in the initialization of the watershed algorithms which looks for relative maxima.

Another example is given in Figure 8-13, which shows collocated SWIM and MFWAM spectra and their partitions using for both a watershed algorithm (calculated off-line for MFWAM). This example illustrates the need to adjust the pre or post-processing the SWIM partitioning in order to avoid over partitioned results.

Other examples of over-partitioning often encountered are probably due to the noise present in the SWIM spectra (see Figure 8-9 above). If not well accounted for, this noise can lead to artificially splitting a single wave system. An alternative is to use a post-processing algorithm merging neighboring partitions with small contrast. Such methodologies will be tested in the future.

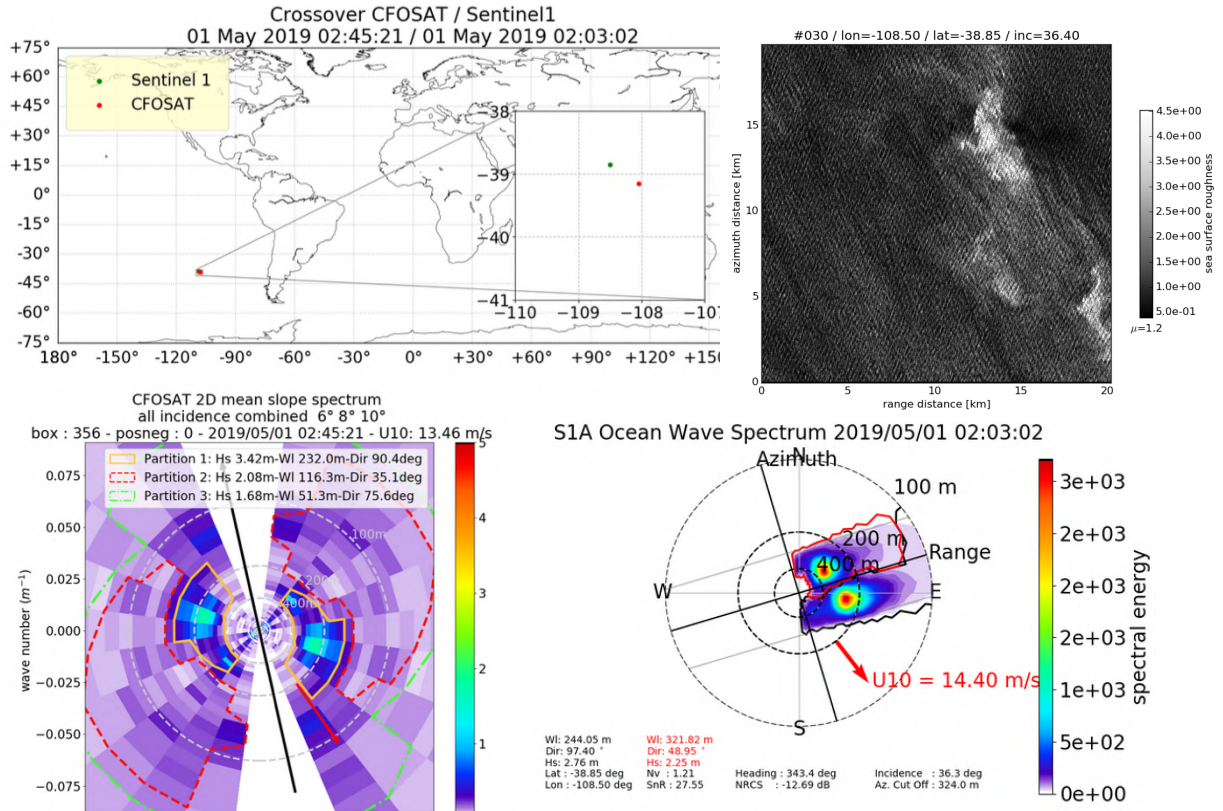


Figure 8-10 : Illustration of collocated wave spectra imaged by SWIM and Sentinel-1

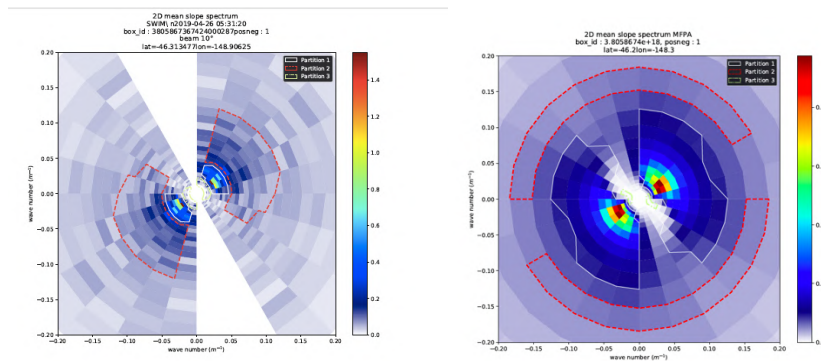


Figure 8-11: Collocated SWIM and MFWAM spectra with their associated partitions (solid white contour for the first partition, dashed red contour for the second one)

## 8.4 SOME COMPARISONS WITH BUOY DATA

First comparisons of 2D and omni-directional spectra with buoy data have been performed. Here we illustrate three cases.

- case 1 of August 19th 2019, 18:00 UTC at the Brittany buoy location (47°33'0" N 8°28'12"). This case corresponds to a young swell from NW generated in the Atlantic open ocean. Figure 8-12 compares the 1D and 2D spectra from the Brittany buoy, the SWIM data, and the MFWAM model. The peak and shape of the 1D spectrum from SWIM are in good agreement with the buoy and the model. However, SWIM data shows two issues: the energy is underestimated in the swell energy part, and there is a parasitic peak at low frequency. The underestimation of energy or wave height observed in this case is probably due to the mask on the SWIM spectra as shown in the comparison of the 2D spectra. We expect that this problem will be reduced when we will be able to better correct for speckle noise and subsequently suppress this mask. The parasitic peak (corresponding to wavelengths of about 600m) is probably due to the presence of inhomogeneities in the SWIM footprint which induce energy at low wave number or frequency. It shows that a better filtering of these effects in the SWIM data is necessary. The good consistency in the shape of the spectra with frequency is an indirect indication that the MTF is appropriate (at least the fact that it is constant with wavenumber).

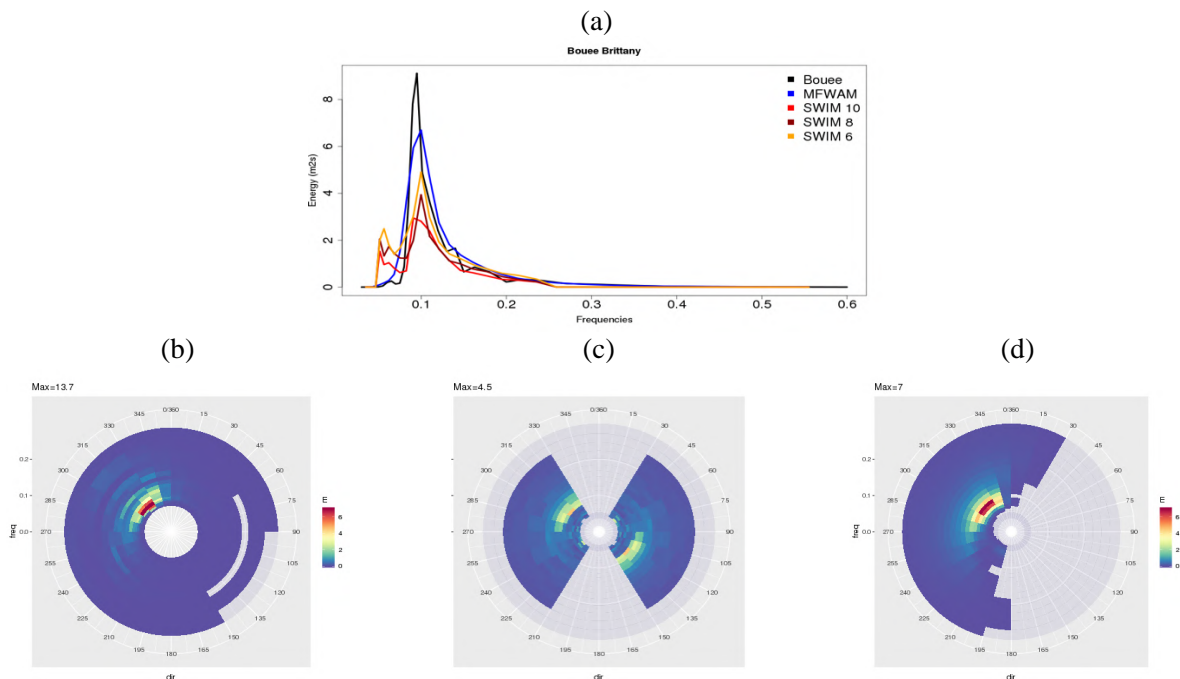


Figure 8-12: (a) Omni-direction spectra ( $m^2s$ ) from the Brittany buoy(47°33'0" N 8°28'12"), MFWAM and SWIM (3 beams the red, brown and yellow curve as indicated in the insert) on 19 August 2019 18:00 UTC. (b, c,d) directional spectrum from (b) the buoy, (c) SWIM beam 10°, (d) MFWAM

- case 2 of August 14th 2019 18:00UTC at 6 miles from the “Yeu” Island near the French coasts ( $46^{\circ}49,993'N$ ,  $02^{\circ}17,700'W$ ) . This case corresponds to total significant wave height of 2m dominated by a swell propagation from the west. A less energetic wind sea is also present (about 1m significant wave height) from South. Figure 8-13 shows that the swell component is very well captured by SWIM and not by MFWAM in this case. The shape of the SWIM spectra is in very good agreement with that from the buoy, except again at very low frequencies, where we observe a parasite peak of high energy which may be due to inadequate rejection of non-homogeneities in the SWIM footprint. This peak is even higher than the one associated to the swell, which means that in the future, these parasitic peaks must be better filtered out from the SWIM data.

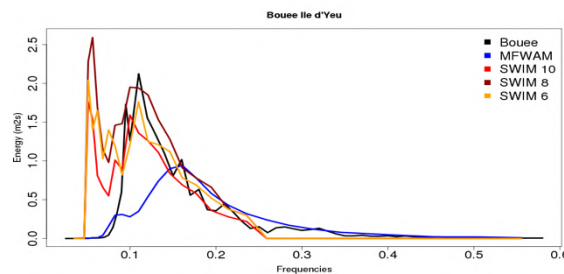


Figure 8-13: Omni-direction spectra ( $m^2s$ ) from the Yeu Island buoy( $46^{\circ}49,993'N$ ,  $02^{\circ}17,700'W$ ), MFWAM and SWIM (3 beams with the red, brown and yellow curves as indicated in the insert) on 19 August 2019 18:00 UTC

- case 3 of July 24th 2019, 18 00 UTC at the Brittany buoy location ( $47^{\circ}33'0'' N$   $8^{\circ}28'12'' W$ ). This case corresponds to a mixed sea condition generated by a mid-latitude storm in the Atlantic waters: according to the buoy observations, there is first a wind sea from South with a 0.2Hz peak frequency; this component cannot be captured by SWIM because its direction is within the masked sector and the wavelength is under the detection limit of SWIM. There are also two swell systems, one around 0.16 Hz and one around 0.09 Hz. Both swell systems are well identified by SWIM which better captures the second swell from West than the model (see the directional plots.) As observed for the other cases, there is an important parasitic peak at low frequency, which is not observed by the buoy.

These comparisons, although performed on a limited number of cases, already show that SWIM provides details on the wave spectra which are sometimes not captured by models. They contain useful information to correct or constrain models, for example through assimilation procedures (see section 8-6). The 3 examples also illustrate the need for a better filtering of the energy at the lowest wavenumbers (frequencies) in the SWIM data. Presently the maximum wavelength considered in the NRT products is around  $2\pi/600m$ , whereas the current L2 product keeps information for wavelengths larger than that; this probably should be modified in the future. An improvement could also be to apply FFT analysis on signal modulation periodograms of smaller in size than those presently used (the whole footprint is currently considered in the CWWIC products) and reject spectra which are not close enough to the mean. This is the option proposed for the IWWOC products (tests in progress). Finally, this study also validates in an indirect way the assumption of the MTF (constant with wavenumber) as the shape of the SWIM 1D wave spectra is very similar to that of the buoy data; this is also discussed in section 8.5.2, by using

model data.

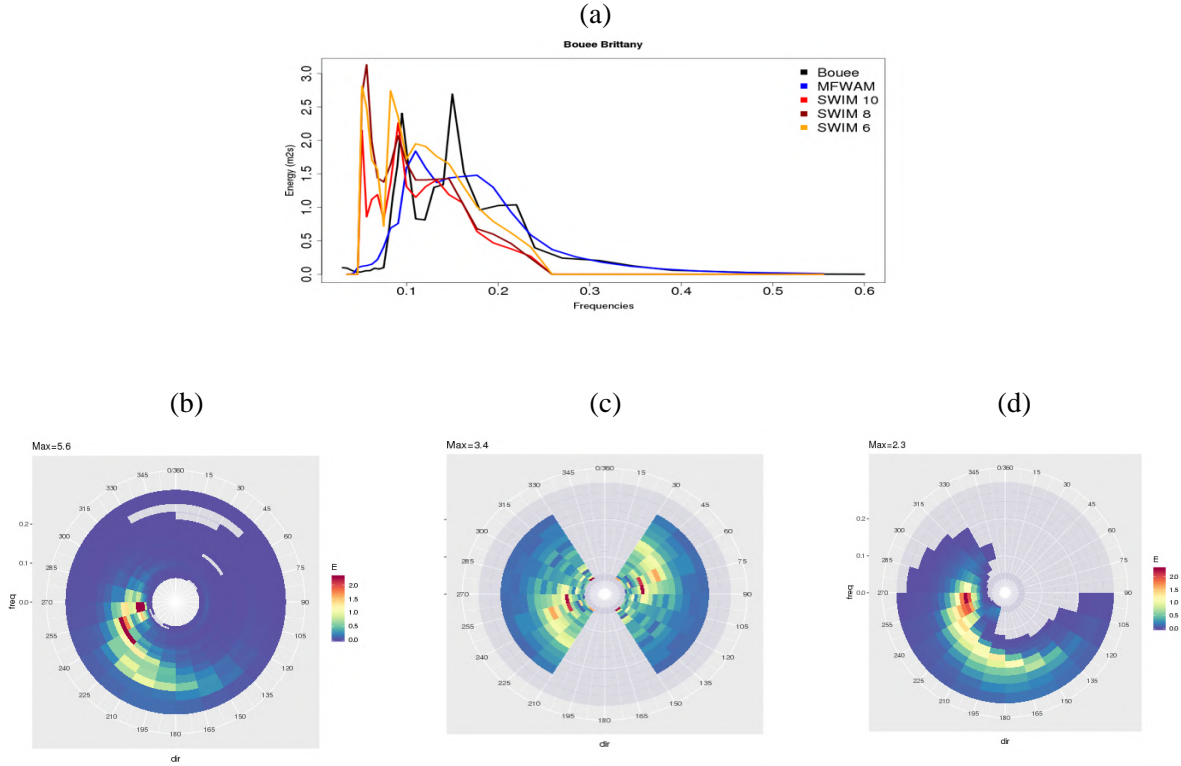


Figure 8-14: Same as Figure 8-12 but for a location close to the Brittany buoy (47°33'0" N 8°28'12" W) on July24th 2019, 18:00UTC

## 8.5 STUDIES ON THE MODULATION TRANSFER FUNCTION

### 8.5.1 MTF FROM THE CWWIC PRODUCTS

The modulation spectrum  $P_m(k)$  from SWIM measurements is related to the slope spectrum  $k^2F(k)$  through the modulation transfer function (MTF).

$$P_m(k) = MTF k^2F(k) \quad (2)$$

where  $F(k)$  is the wave height spectrum.

The scattering theory and solution for near-nadir viewing radar measuring reflectivity modulation spectrum was developed by Jackson et al in [R14, R15, R16]. Based on various approximations, it was shown that the MTF can be written as

$$MTF(\theta, \varphi) = \frac{\sqrt{2\pi}}{L_y} \alpha^2(\theta, \varphi) \quad (3)$$

$$\text{with } \alpha(\theta, \varphi) = \cot(\theta) - \frac{1}{\sigma_0} \frac{\partial \sigma_0}{\partial \theta} \quad (4)$$

where  $L_y$  the footprint dimension in the azimuth direction,  $\sigma_0$  is the normalized radar cross-section,  $\theta$  the incidence angle and  $\varphi$  the azimuth look direction.

Eq. (2-4) are valid only under the following assumptions: (i) the dimension of the footprint is very large with respect to the wave dimensions (true for SWIM), ii) the local slopes of the waves remains small iii) hydrodynamic modulations can be neglected.

The current L2 products (configuration MTF1) are provided using these expressions, where the mean trend of  $\sigma_0$  with incidence is estimated from the SWIM observations using the profiles of  $\sigma_0$  for each azimuth, between 2 and 11° of incidences.

CWWIC also provides products for experts which include alternative MTF with respect to the one used in version 4.3.0 (see [2]). In particular option 3 (for MTF3) is not based on the assumptions here above but it is calculated so that the significant estimated from  $F(k)$  is equal to  $H_s$  from nadir.

Here we compare the dependence of MTF1 and MTF3, with respect to wind speed and wave height to examine whether the MTF1 behavior is consistent or not.

Figure 8-15 (upper left) shows the behavior of MTF1 with wind speed (here ECMWF winds). The mean trend is a decrease of MTF1 with wind speed, which is consistent with what is expected from the behavior of the  $\alpha$  coefficient (using for example the quasi-specular backscattering model for  $\sigma_0$ ). However, this trend is found here rather weak except at winds smaller than about 3 m/s. The same kind of behavior is found when analyzing the trend of MTF1 with significant wave height (Figure 8-15 bottom left).

The right-hand side of Figure 8-15 shows the behavior of MTF3 which is estimated so that the significant wave height of each SWIM spectrum coincides with the significant wave height measured from the nadir beam. In the present version, MTF3 is estimated by normalizing the energy of the SWIM directional spectrum (corrected from speckle noise) without mask with respect to the energy corresponding to the nadir significant wave height. Because of the remaining perturbations due to speckle noise in the along-track direction (see section 7), this may slightly bias the results. Therefore, this analysis will be redone after an improved speckle correction can be applied.

However, we can already mention that the trend of MTF3 with wind speed or wave height (Figure 8-11 right) is quite different from that of MTF1 (Figure 8-15 left). A decrease with wind speed is also found but it is much more pronounced. Furthermore, the values of MTF3 for a given wind speed are much more spread than in the case of MTF1, and particularly at winds smaller than 15 m/s. This large scatter is probably mainly due to the presence of noise still remaining in the SWIM modulation spectra (with a too small subtraction of speckle noise spectrum). It is possible that the largest dependence with wind speed or wave height compared to MTF1 indicates that the theoretical model of MTF1 should be revisited.

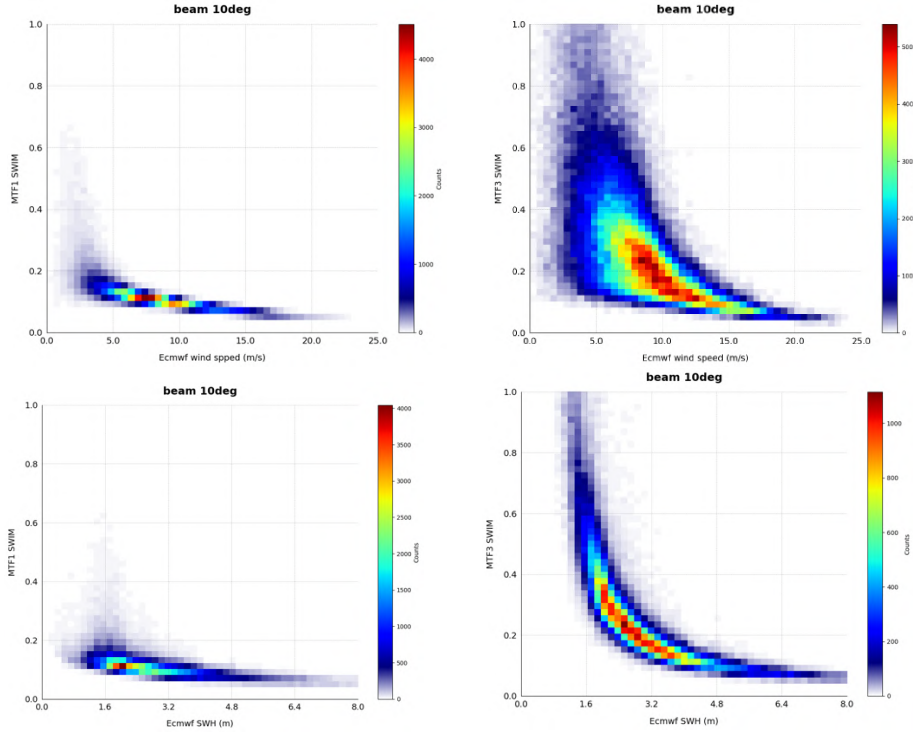


Figure 8-15 : Modulation Transfer function versus collocated significant wave height (from ECMWF here), for MTF1 (left) and MTF3 (right).

### 8.5.1 INDIRECT ANALYSIS OF THE MTF THROUGH COMPARISONS OF SLOPE SPECTRA BETWEEN SWIM AND WW3

Another form of the approximation proposed by {R15, R16} is based on Eq (2-3) , and (5) below:

$$\alpha(\theta, \varphi) = \left( \cot \theta - \frac{\partial \ln p(s)}{\partial s} \right) \quad (5)$$

$p(s)$  is the probability density function of the slopes at the surface,

Expressions (2-3-5) have been used in an analysis which used the fluctuations spectra to check in what conditions, the linear relation between the slope spectra and the modulation spectra remains valid. For this purpose, we have compared omni-directional slope spectra  $k^2 F(k)$  inversed from Eq.2-3-5 to collocated Wave Watch III wave slope spectra. The omni-directional spectra exclude the observations in the along-track directions to avoid the problem of large speckle perturbation. In addition the omni-directional fluctuation spectra have been corrected for speckle by fitting a triangle function on each considered fluctuation spectra (similarly to what is done in the CWWIC processing chain but applied here on omni-directional spectra).

For this study, the term  $\frac{\partial \ln p(s)}{\partial s}$  in (5) has been estimated by assuming that the slope pdf follows a Gaussian shape with variance mss (mean square slope) , which leads:

$$\frac{\partial \ln p(s)}{\partial s} = - \frac{2 \tan \theta}{\langle mss \rangle} \quad (6)$$

Furthermore, mss was parameterized as a function of wind speed  $U_{10}$  and wind direction with respect to the antenna azimuth:

$mss = f(U_{10}, (\varphi - \varphi_0))$  where  $f$  is a function provided using an empirically-derived GPM mission look-up table and  $U_{10}$  was taken from the ECWF winds.

Figure 8-16 shows the comparison of the mean inversed slope spectra corresponding to the  $10^\circ$  SWIM beam measurements against the collocated Wave Watch III model output for selected categories of wind speeds. Twelve days of observations have been considered in this analysis. It shows that in average, inversed slope spectra generally follow the WW3 spectra, especially for winds  $U_{10} > 9$  m/s . This means that the linear relation is globally valid. However, small nonlinear effects are also apparent. Our results also indicate that these effects are larger at  $8$  and  $6^\circ$  (not shown). This is explained by the fact the assumptions ii) and iii) mentioned in the previous section are less and less valid when the incidence angle goes close to nadir. Work is under progress to analyze in more details the conditions which creates this non-linearity and propose a way to correct for this effect.

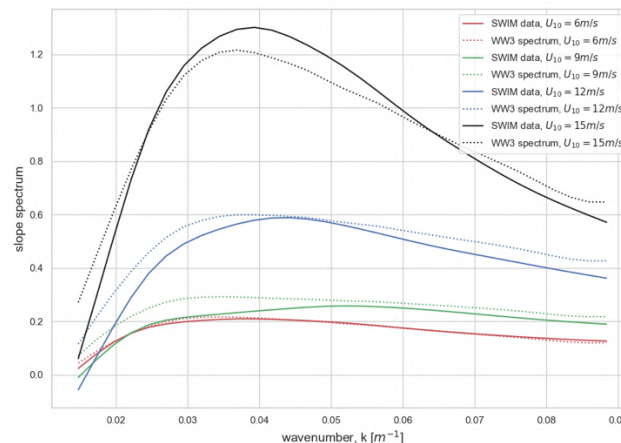


Figure 8-16: Mean slope spectra inversed from SWIM  $10^\circ$  radar beam observations as explained in section 8.5.1, in comparison with time-spatial collocated Wave Watch III model for four different wind speeds.

## 8.6 VALIDATION BY USING ASSIMILATION PROCESSES IN WAVE FORECAST MODEL

### 8.6.1 METHODOLOGY

During the calibration/validation phase of CFOSAT mission the assimilation of SWIM level 2 wave products is used to evaluate the quality of the data and the performance of the assimilation in both analysis and forecast periods. A quality control procedure for SWIM Level 2 wave data has been implemented in order to remove data which are inconsistent with respect to the first-guess of the model. Also the along-track mask is used for the wave spectra before the assimilation in the wave model. The wave model MFWAM is set globally for a grid size of  $0.5^\circ$  and is driven by the wind and ice fraction forcing from IFS-ECMWF atmospheric system. The methodology for the assimilation during the Cal-Val phase consists in implementing assimilation runs with SWIM L2 wave products and then perform the validation of the results with independent wave data such as altimeters and buoys. Several assimilation runs including significant wave heights from nadir look and wave spectra from different

beams have been performed to analyze the improvement on the wave forecast. The validation of the assimilation results is mainly performed with altimeters wave heights.

### 8.6.2 RESULTS

Figure 8-16 and Figure 8-17 show the global bias map of significant wave height with and without assimilation SWIM L2 wave data, respectively. It is clear to see the significant reduction of the bias high and intermediate latitudes. The assimilation of nadir SWH and wave spectra from beam 6° improves globally the normalized scatter index of SWH by roughly 16 %. the improvement is enhanced in high and intermediate latitudes to more than 20 %.

The benefit of using directional properties from SWIM wave spectra is well observed on the impact of difference between runs with and without assimilation. This impact of the assimilation on the mean wave period is significant and reaches more than 2 seconds mostly on the ocean swells tracks in the Pacific, Indian and Atlantic oceans, as illustrated in Figure 8-15. Further, one can see easily the good correction induced by the assimilation for the underestimation of mean wave period (red color patches) after the passage of CFOSAT.

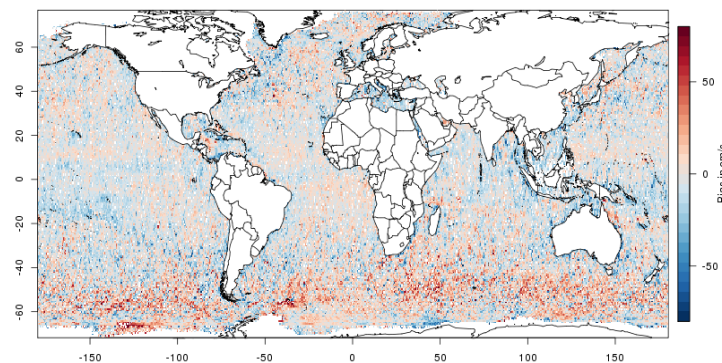


Figure 8-17 : Significant wave height bias map for the run of the model MFWAM with the assimilation of nadir SWH and wave spectra from beam 6° for the period starting from 26 April until 20 May 2019. The validation is performed with altimeters Jason-3, Saral and Sentinel-3A and 3B. The maximum range of bias is roughly 60 cm.

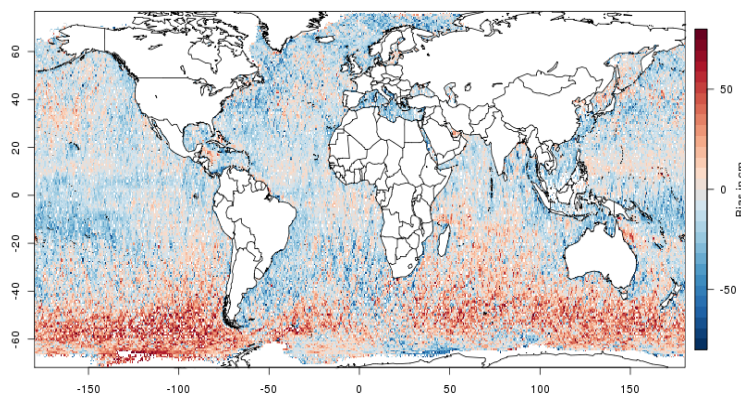


Figure 8-18 : Significant wave height bias map for the control run of the model MFWAM without assimilation for the period starting from 26 April until 20 May 2019. The validation is performed with altimeters Jason-3, Saral and Sentinel-3A and 3B. The maximum range of bias is roughly 60 cm.

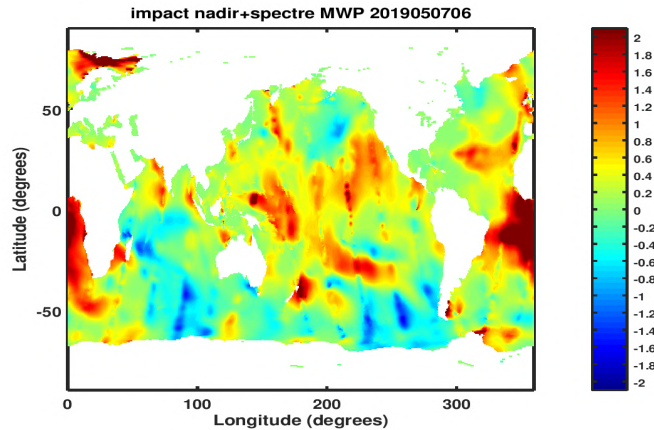


Figure 8-19 : Difference of mean wave periods from runs of the model MFWAM with and without assimilation of SWIM nadir SWH and wave spectra from beam 6° on 7 May 2019 at 06:00 UTC. Red and blue colors stand for overestimation and underestimation of the model MFWAM.

## 8.7 FORESEEN ANALYSES AND EVOLUTIONS

### 8.7.1 PLANNED PROCESSING EVOLUTIONS

As soon as the best option for speckle and MTF corrections are identified, the processing will be done with these optimal options. We hope that the speckle correction will make it possible to suppress the mask presently applied on the data.

Other possible evolutions are already envisaged but not yet fully decided

- change of the azimuth sampling of the 2D wave spectra: 7.5° instead of presently 15°
- improvements in the partitioning algorithm

### 8.7.2 FORESEEN ANALYSES

Work is still need to:

- assess and improve the speckle correction
- evaluate and improve the MTF corrections
- tests to improve the partitioning algorithm
- evaluate the tradeoff between a higher azimuthal sampling and a decrease in the number of independent samples used to estimate the wave spectra
- evaluate the relative performances of the 6, 8, 10° in terms of wave parameters and adjust the proposed combined product;
- consider a possible extension of wave parameters inversion from the 2 and 4° incidence beam data

Note that a change in speckle correction and masking option may affect both the energy of the wave spectra and their partitions but also the partitioning itself. MTF will mainly affect the normalization of the wave spectra. It will not change fundamentally the results of the spectrum partition nor the evaluation of dominant wavelength and direction.

## 9 - SYNTHESIS AND CONCLUSION

These first months of validation have been very fruitful.

The main conclusions are the following:

- The SWIM instrument exhibits a perfect behavior until now
  - Very stable consumption
  - Stable thermal behavior
  - Measured pointing accuracy  $< 0.1^\circ$
  - Antenna rotation speed: 5.6 rpm
  - Impulse response within the requirements and very stable
  - High availability of tracking mode
  
- Nadir parameters (significant wave height,  $\sigma^0$ ) produced by the CWWIC mission center are of excellent quality.
  
- The  $\sigma_0$  products from the different SWIM beams (from  $0$  to  $10^\circ$ ) show very consistent behavior (dependence with incidence and wind speed) and their absolute values are consistent within about  $\sim 1$ - $2$  dB with independent measurements (GPM, altimeter missions). Starting with version 4.3.1 of the CWWIC L1a processing, a new look up table (LUT) is used as input for the azimuthally- integrated antenna gain correction. This makes the  $\sigma_0$  profiles with incidence not anymore dependent of the side of azimuth look with respect to the satellite track and also in better agreement with GPM profiles (less convexity). However, the choice made to build this new LUT must still be validated.
  
- Level 1b products ( $\sigma_0$  fluctuations and their spectra) show consistent results. The analysis has shown that speckle noise is about 5 to 6 times higher when the antenna looks along the satellite track direction. This is consistent with the reduction of Doppler bandwidth for the geometry and it indicates that the speckle correction cannot be considered as independent of azimuth direction as presently assumed in the CWWIC processing chain. The background noise parameterization outside the along-track sector needs also to be modified. Indeed, the present corrections seem to underestimate the speckle noise at small wavenumbers and overestimate it at large wavenumbers.
  
- Level 2 products: The first conclusion is that SWIM detects correctly the waves in the range [70m-500m]. However, with the present processing the 2D wave spectra exhibit an important background noise in all directions and an important increase of this noise in the along-track direction. This noise is attributed to speckle effects which are not yet considered yet with a sufficient accuracy. Work is under progress to better estimate and subtract from the 2D wave spectra this background noise. In spite of this shortcoming, the performances on significant wave height, wavelength and wave direction are very encouraging. When estimated on same partitions (with MFWAM model as reference), they are very consistent with collocated MFWAM parameters. Some biases (in particular for the significant wave height  $H_s$  when  $H_s$  is smaller than 4-5 m, must still be confirmed and analyzed. One recommendation at this stage is to be cautious in the use of the parameters of the spectral partitions as given in the products, because the partitioning algorithm is still not well tuned for our conditions (with large background noise). From the first comparisons with buoy data we find that a parasite peak at low wavenumbers should be better filtered out, and that the shape of the 1D wave height spectra is in good agreement with that of the buoys, which indicates that the assumption of linearity between fluctuation spectra and wave spectra is valid.

The intense CAL-VAL activity will continue in the next months, with the support of a larger group of experts. In particular, further work will focus on the following aspects:

- Nadir products:

- Calibration of coefficients for wind speed inversion consistently with the series of other altimeter from the  $\sigma_0$  values
- Validation of mean square slopes retrieved from the “adaptive” inversion method remains to be done
- analysis of the rain flag performance
- Validation of ICE1 and ICE2 inversion algorithms

- Precise  $\sigma_0$  calibration based on:

- analysis of data from transponders
- inter-comparison with respect to other data sets (altimeter missions, GPM,)
- analysis of possible relative biases between the different beams of SWIM

- Impact of atmospheric effects (rain, clouds) on  $\sigma_0$  and on wave products

- Level 1b products from CWWIC

- Further analysis is needed to qualify the different options of speckle noise corrections
- 3<sup>rd</sup> and 4<sup>th</sup> order statistical parameters (skewness, kurtosis) of the  $\sigma_0$  fluctuations could be analyzed more precisely to use them as flags on the surface scene
- Quality flags need to be adjusted and analyzed

- Level 2 products from CWWIC: these products could only be analyzed globally since April 25<sup>th</sup> 2019 because of the perturbation induced by the incorrect on-board processing before this date. Therefore, we still need

- a systematic validation of wave parameters compared to references (wave models, buoy, SAR data) from the full and partitioned spectra;
- analyses of the relative performances of the 6, 8, 10° in terms of wave parameters and adjustment and the proposed combined product;
- analysis of the results from the different MTF choices, recommendation on the optimal choice for wave inversion;
- analysis of a possible extension of wave parameters inversion from the 2 and 4° incidence beam data.

In spite of these necessary improvements, the conclusion is that the SWIM data are of good quality and that very shortly after the launch they can be used for scientific studies provided that the users take into account the limits mentioned here. Work is under progress to better correct the wave spectra from the speckle perturbation, to further evaluate the validity of the Modulation Transfer Function, and to improve the partitioning algorithm.

**Note:** datasets acquired before April 25<sup>th</sup> will not be disseminated. Provision of these data will be analyzed (product level, application, ...) upon request for specific studies.

**10 - ANNEX A - SWIM ACQUISITION MODES SINCE THE 25<sup>TH</sup> APRIL 2019**

Starting date and approximate time	End date and approximate time	Orbit cycle	Antenna mode : Nominal -N (ie rotating), or Fixed -F	Macrocycle mode (sequence of antenna beam illumination): either Nominal-N (0_2_4_6_8_10), or as indicated	Acquisition mode: Nominal-N or Speckle mode -S
25/04/2019 00:15	24/06/2019 18:20	14 to 19	N	N	N
24/06/2019 18:20	24/06/2019 18:40	19	N	0_0	N
24/06/2019 18:40	25/06/2019 23:59	19	N	N	N
26/06/2019 00:00	27/06/2019 23:59	19	N	N	S
28/06/2019 00:00	29/06/2019 23:59	19	N	0_2_8_8	S
30/06/2019 00:00	01/07/2019 23:59	19	N	0_2_10_10	S
02/07/2019 00:00	02/07/2019 23:59	19	N	0_2_8_8_8	N
03/07/2019 00:00	03/07/2019 23:59	19	N	0_2_10_10_10	N
04/07/2019 00:00	04/07/2019 03:05	19	F (0°)	N	N
04/07/2019 03:05	04/07/2019 21:05	19	F (0°)	0_2_8_10	N
04/07/2019 21:05	04/07/2019 23:59	19	F (0°)	N	N
05/07/2019 00:00	05/07/2019 02:55	19	N	N	N
05/07/2019 02:55	05/07/2019 06:01	19	F (90°)	N	N
05/07/2019 06:01	05/07/2019 23:59	19	F (90°)	0_2_4_6	N
06/07/2019 00:00	06/07/2019 03:06	19	F (90°)	N	N
06/07/2019		20 to 25	N	N	N

**Legend :**

For instrumental calibration needs
SWIM & SCAT in STAND-BY mode during 4h30 due to solar/moon eclipse conjunction
Nadir Sigma0 calibration using on-ground transponder
For scientific needs

**Reference :** CF-SYMI-NT-3572-CNES

**Issue :** 1.0

**Date :** 2019\_09\_11

## 11 - ANNEX B- CWWIC PROCESSING VERSIONS CORRESPONDING TO DATA RELEASE TO USERS

The processing chain at CWWIC is called AWWAIS. During this CAL/VAL, some data sets were produced with the prototype chain whereas the regular data production comes for the operational chain.

Data sets period and delivery	Data sets produced by	Processing version	Main changes with respect to the previous version	Comments
26 April to 11 June 2019  Data sets made available by CNES to CAL/VAL contributors	Prototype implemented at CNES	4.3.0	<p><b>L1a:</b></p> <ul style="list-style-type: none"> <li>- New variable called “reliable_swath_x” (x: beam number) indicating the efficient swath indices (within the 3dB antenna gain aperture)</li> <li>- Thermal noise estimated from the noise floor of the 2° beam echo instead of the nadir echo,</li> <li>- Output of linear values of <math>\sigma_0</math> instead of dB, no data filtering for negative value</li> </ul> <p><b>L1b:</b></p> <ul style="list-style-type: none"> <li>- additional flag to distinguish between slope and convexity behavior of the <math>\sigma_0</math> profiles (with respect to GPM LUT)</li> </ul> <p><b>L2-wave products:</b></p> <ul style="list-style-type: none"> <li>- directional wave spectra provided either as masked or non-masked variables (masked to mitigate the along-track noise issue)</li> <li>- wave parameters calculated on the masked spectra</li> <li>- Implementation of an new speckle calculation method (dependent on azimuth direction) as a new possible option. This option is available but not yet activated in products.</li> </ul> <p><b>L2-nadir:</b></p> <ul style="list-style-type: none"> <li>- Correction of the mispointing angle used as retracking algorithm’s input</li> <li>- Correction of the nadir-estimated rain flag</li> </ul>	<p>Still some bugs identified:</p> <p>L2:</p> <ul style="list-style-type: none"> <li>- phi_orbit_box is incorrect</li> <li>- nadir_swh_box and nadir_sogma0_box are incorrect</li> <li>- implementation on the speckle correction has no impact on the products, as the option is not activated yet</li> </ul>

**Reference :** CF-SYMI-NT-3572-CNES

**Issue :** 1.0

**Date :** 2019\_09\_11

16 July 2019 05:33 to 29 July 10:00  Data sets made available by CNES to French CAL/VAL groups	Operational CWWIC chain	4.3.1	Same as 4.3.0 but for the operational chain	
From 29 July 2019, 10:14 UTC Beginning of data release to all science team members	Operational CWWIC chain	4.3.2	<p><b>L1a:</b></p> <ul style="list-style-type: none"> <li>- New LUT used to prescribe the pre-calculated antenna gain pattern integrated over the azimuth direction</li> <li>- Correction of anomaly on the flag on mispointing ( flag_dep)</li> </ul> <p><b>L2 :</b> bugs corrected on phi_orbit_box, nadir_swh_box and nadir_sigma0_box</p>	